Physical Controls on Cirrus Cloud Inhomogeneity

Jennifer E. Kay

A dissertation submitted in partial fulfillment of the requirements for the degree of

Doctor of Philosophy

University of Washington

2006

Program Authorized to Offer Degree:

Earth and Space Sciences

University of Washington
Graduate School

This is to certify that I have examined this copy of a doctoral dissertation by

Jennifer E. Kay

and have found that it is complete and satisfactory in all respects, and that any and all revisions required by the final examining committee have been made.

Co-Chairs of the Supervisory Committee:

_____
Marcia B. Baker

_____
Dean A. Hegg

Reading Committee:

_____
Marcia B. Baker

_____
Dean A. Hegg

_____
Qiang Fu

Date:_____

In presenting this dissertation in partial fulfillment of the requirements for the doctoral degree at the University of Washington, I agree that the Library shall make its copies freely available for inspection. I further agree that extensive copying of the dissertation is allowable only for scholarly purposes, consistent with "fair use" as prescribed in the U.W. Copyright Law. Requests for copying or reproduction of this dissertation may be referred to ProQuest Information and Learning, 300 North Zeeb Road, Ann Arbor, MI 48106-1346, 1-800-521-0600, or to the author.

Signature_____

Date_____

University of Washington

Abstract

Physical Controls on Cirrus Cloud Inhomogeneity

Jennifer E. Kay

Co-Chairs of the Supervisory Committee:
Professor Marcia B. Baker
Department of Earth and Space Sciences
Professor Dean A. Hegg
Department of Atmospheric Sciences

Cirrus cloud inhomogeneity can generate large biases in radiative transfer and climate model calculations. Understanding cirrus inhomogeneity will improve physically based model parameterizations. In this study, we use a parcel model with binned ice microphysics and observational analyses to assess physical controls on cirrus inhomogeneity, herein measured using an optical depth distribution ($P(\sigma)$). In Chapter 2, we calculate microphysical and dynamical timescales and $P(\sigma)$ along simple trajectories using atmospherically relevant ranges of aerosols, ice nuclei (IN), temperatures (T), vertical velocities (w), and deposition coefficients. $P(\sigma)$ shape depended on the ratio R: fallout timescale (τ_{fall}) over growth timescale (τ_{growth}). With $R > 1$, $P(\sigma)$ had a peak at large σ ($\sigma > 1$) while with $R < 1$, $P(\sigma)$ had a monotonically decreasing shape. Of the atmospheric input variables, w had the largest influence on R and $P(\sigma)$ shape. In Chapter 3, we analyze a cirrus climatology from Lamont, OK to identify typical $P(\sigma)$ shapes and to evaluate which parameters could explain the observed $P(\sigma)$. Most cirrus had monotonically decreasing $P(\sigma)$ shapes ($R < 1$), $\sigma < 0.5$, and $T < -40$ ºC. Observed cirrus $P(\sigma)$ were attributed to homogeneous nucleation alone, mesoscale (100-1000s m) variability in w, thin saturated layers, and short ice crystal residence times below cloud. In Chapter 4, we use the parcel model and trajectories derived from a mesoscale weather model (MM5) to evaluate $P(\sigma)$ during an orographic cirrus event. Along MM5 trajectories, parcel model cirrus cloud fraction, cloud lifetimes, and $P(\sigma)$ were largely controlled by synoptic scale lifting and the presence of mesoscale gravity waves ($w > 1$

m/sec). Large and variable N_{ice} associated with variable w resulted in broad $P(\sigma)$. Background IN increased cloud cover, but did not prevent homogeneous nucleation. The spatial resolution of the MM5 domain and the IN specification affected $P(\sigma)$. Taken together, our modeling and observational analyses suggest that cirrus $P(\sigma)$ are more sensitive to plausible variations in dynamic forcing than to plausible variations in aerosol forcing.

TABLE OF CONTENTS

LIST OF FIGURES

LIST OF TABLES

ACKNOWLEDGEMENTS

Many people have made the research presented in this dissertation possible. Marcia Baker and Dean Hegg have been patient, honest, attentive, and thoughtful Ph.D. advisors for the last four years. Their expertise and hard questions improved the quality of the science presented in this dissertation. They have also been inspiring role models and kind mentors. I have greatly appreciated their willingness to let me be independent and to pursue opportunities beyond the scope of my dissertation research.

Alan Gillespie, Tom Ackerman, and Qiang Fu have contributed to my development as a scientist by encouraging me to pursue new research and by always providing thoughtful feedback.

I am grateful to Robert Elleman, Rob Wood, Mark Stoelinga, Dale Durran, Steve Warren, Steve Burges, John Locatelli, Brian Swanson, at the University of Washington, Dave Turner at University of Wisconsin, and Jennifer Comstock at PNNL for fruitful scientific discussions, inspiration, and technical help.

Katie (Crahan) Kaku, Matt Garvert, and Robert Hahn have been patient and supportive officemates. Stephanie Kampf and Amy Gaffney have been supportive friends and are inspirational women scientists in my generation. I thank my friends, collaborators, and mentors in Earth and Space Sciences, Atmospheric Sciences, the Program on Climate Change, and at the Climate Impacts Group. They have made graduate school interesting, challenging, rewarding, and fun.

Finally, my parents Suzanne and Robert Kay, my brother Alex Kay, my grandmother Norine Mahlburg, and Robert Elleman have been supportive and wonderful throughout the entire graduate school process.

Chapter 1:
INTRODUCTION

1.1. Research goal and chapter organization

In this dissertation, we use modeling and observations to assess the influence of physical processes on cirrus optical depths and radiative impacts. Throughout our work, we approximate the visible optical depth (σ) of a cirrus cloud as:

$$\sigma = 2\pi {R_{eff}}^2 N_{ice} \Delta z \tag{1.1}$$

where N_{ice} is the number concentration of ice crystals (# cm^{-3}), R_{eff} is the effective radius (m), and Δz is the cloud thickness (m).

We define R_{eff} as:

$${R_{eff}}^2 = \frac{\int {R_{ice}}^2 N_{ice} dR_{ice}}{N_{ice}} \tag{1.2}$$

where R_{ice} is the ice crystal radius.

The primary goal of our research is to understand the physical controls on cirrus inhomogeneity, i.e., radiatively important σ variability.

In this introductory chapter, we describe the influence of clouds on radiative fluxes, with a particular emphasis on cirrus and the importance of cirrus inhomogeneity (Section 1.2). Then, we review the current understanding of ice formation in the atmosphere (Section 1.3). Next, we describe the way climate models represent cirrus processes and inhomogeneity (Section 1.4). Finally, we summarize this introductory chapter and describe the goals and scope of the research presented in the remaining chapters of this dissertation.

1.2. The influence of clouds on radiative fluxes and climate

Clouds regulate the Earth's climate by modifying radiative fluxes. Clouds reflect solar radiation, which cools the underlying surface and atmosphere, and reduce the infrared emission to space, which warms the underlying surface and atmosphere. In this section, we define and present an algebraic expression for the cloud radiative impact (CRI – Wm^{-2}), we discuss the contribution of clouds to the current climate and to uncertainty in projections of future climate, and finally, we discuss the effect of cirrus and cirrus inhomogeneity on radiative fluxes.

At any height in the atmosphere, the net influence of the cooling cloud albedo effect and the warming cloud greenhouse effect can be expressed as:

$$CRI = F_{cloud} - F_{clear} \quad (1.3)$$

where F_{cloud} is the net downward radiative flux in an area with 100% cloud cover (Wm^{-2}), F_{cloud} is the net downward radiative flux in an area with no clouds (Wm^{-2}).

By neglecting the influence of multiple scattering, atmospheric gases, and aerosols on radiative fluxes, the CRI at the top of the atmosphere (TOA) can be approximated as:

$$CRI = -\left(\frac{S}{4}\right)\left(a_c + (1-a_c)^2 a_s - a_s\right) + \sigma_{sb}\left(T_s^{\,4} - T_c^{\,4} - (T_s^{\,4} - T_c^{\,4})e^{-\sigma D/c}\right) \quad (1.4)$$

where S=1367 is the Solar constant (Wm^{-2}), a_s is the surface albedo, a_c is the cloud albedo, $\sigma_{sb}=5.67*10^{-8}$ is the Stefan Boltzmann constant, T_s is the surface temperature, T_c is cloud temperature, D is the diffusivity factor, and c is a factor to relate σ to the infrared optical depth.

Throughout this chapter, we use Eq. 1.4 to quantify the effect of clouds on radiative fluxes. The first and second term on the RHS of Eq. 1.4 represent the cloud albedo effect and the cloud greenhouse effect respectively. Because clouds both cool and warm the climate, the magnitude and the sign of the CRI depends on surface properties such as a_s and T_s and cloud properties such as T_c, a_c, and σ. If the σ is specified, the CRI can be calculated by relating a_c to σ, and by relating σ to the infrared optical depth. For example, for cirrus we relate cirrus a_c to σ using Eq. 1 from

Garrett et al. (2003) with an asymmetry parameter g=0.8, and we relate the visible to the infrared optical depth using c=2 (Fu et al., 2000).

The CRI is related to another metric that is frequently used to calculate the impact of clouds on radiation, the cloud radiative forcing (CRF - Wm^{-2}):

$$CRF = F_{allsky} - F_{clear} = cf * CRI \quad (1.5)$$

where F_{allsky} is the net downward radiative flux in a partially cloudy area (Wm^{-2}), F_{clear} is the net downward radiative flux in the clear air portions of a partially cloudy area (Wm^{-2}) and cf is the cloud fraction.

We chose to use CRI (Eq. 1.4) because CRF (Eq.1.5) requires a measure of the cf.

Estimates of the global TOA CRF based on observations range from -21 to -24 Wm^{-2}, but there are regional differences in effect of clouds on climate ((Hartman et al., 1992), (Sungsu Park, personal communication)). The observed negative global TOA CRF results from low clouds that cover large areas and have a stronger albedo effect than greenhouse effect. However, clouds can warm the climate in locations with low incoming solar radiation, high a_s (e.g., snow-covered areas, deserts), or when clouds are optically thin and have low emission temperatures.

Quantifying the radiative impact of clouds has received extra scientific attention since the discovery of anthropogenic climate change. For a doubling of CO_2, uncertainties in the CRF response reported in the 2001 Intergovernmental Panel on Climate Change (IPCC) assessment report (Houghton et al., 2001) are larger than the CO_2 radiative forcing (~3.7 Wm^{-2}). Given these findings, the 2001 IPCC report stated: “Probably the greatest uncertainty in future projections of climate arises from clouds and their interactions with radiation”. A recent review by Soden et al. (2006) found that climate model cloud feedbacks enhance global warming due to increasing greenhouse gases, but that cloud feedbacks remain as the largest source of uncertainty in current climate sensitivity predictions.

Cirrus affect the Earth's climate through their direct effect on radiative fluxes and their indirect effect on upper tropospheric moisture budgets. Cirrus have a stronger greenhouse effect than low clouds because of their low emission temperatures (T_c < -30 °C). As a result, both the magnitude and the sign of cirrus CRF depends on the cloud optical properties and T_c ((Chen et al., 2000), (Hartmann et al.,1992); (Fu et al., 2002)). Optically thin cirrus have a positive CRI and warm the Earth's climate because they have a weak albedo effect (Figure 1.1, Figure 1.2). On the other hand, optically thick cirrus have a strong albedo effect, and cool the climate despite their low emission temperatures. Most cirrus are optically thin ($\sigma < 5$), and warm the climate.

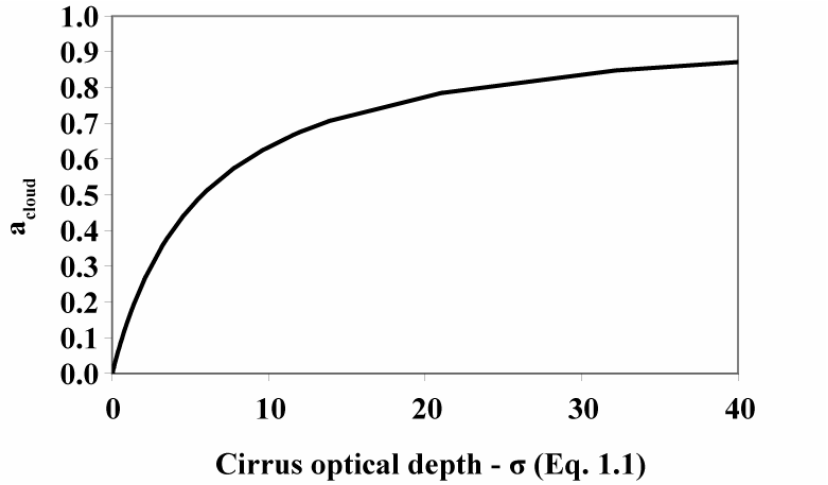

Figure 1.1: Relationship between cirrus albedo and σ. In our simple radiative transfer calculations, a_c and σ were related using Eq. 1 from Garrett et al. (2003) with an asymmetry factor g=0.8.

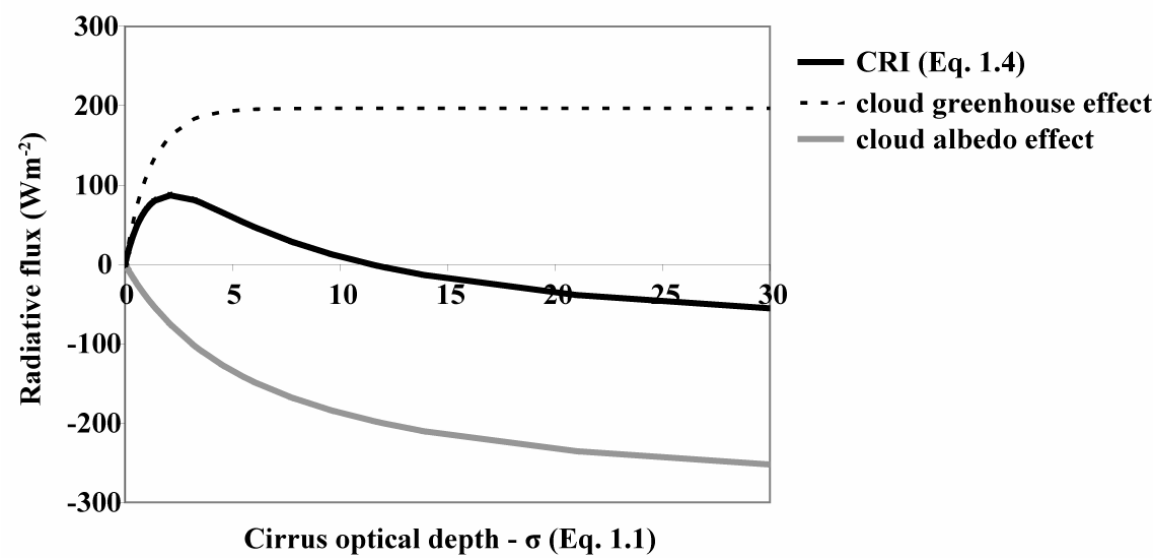

Figure 1.2: Effect of cirrus on top-of-atmosphere radiative fluxes. Optically thin cirrus warm the climate (CRI > 0), while optically thick cirrus cool the climate (CRI < 0). Our CRI calculations neglect the atmosphere (Eq. 1.4) and assume T_c=- 40 °C, Δz= 1000 m, T_s=10 °C, a_s=0.1, c=2 (Fu et al., 2000). We relate a_c to σ using Eq. 1 from Garrett et al. (2003) and g=0.8 (see Figure 1.1).

In addition to their direct effects on radiative fluxes, cirrus also modify the vertical distribution of a potent greenhouse gas: upper tropospheric water vapor. Model projections for global warming due to increasing greenhouse gases double via an upper tropospheric water vapor feedback (Houghton et al., 2001). The strength of a water vapor feedback cannot be directly inferred from thermodynamic arguments because upper tropospheric humidities are often well below water saturation. Cirrus processes affect the vertical and lateral transport of upper tropospheric water vapor and therefore modify the strength of the water vapor climate feedback.

Cirrus inhomogeneity affects radiative fluxes at all scales greater than the radiative smoothing scale (Davis et al, 1997). Below the radiative smoothing scale, horizontal σ variability is smoothed out by multiple scattering and does not affect radiative fluxes. Smith and Delgenio (2001) estimated that the radiative smoothing scale for cirrus ranges from 50 to 150 m, with an average of ~100 m. Throughout this work, we consider cirrus inhomogeneity on scales from 100 m to 300 km, a typical global climate model (GCM) spatial resolution (Houghton et al., 2001).

Researchers have demonstrated that neglecting cirrus inhomogeneity leads to significant radiative transfer biases. Carlin et al. (2002) and Fu et al. (2000) estimated the radiative impact of cirrus inhomogeneity by comparing radiative transfer calculations that included inhomogeneity with calculations that assumed plane parallel homogeneous (PPH) cirrus. They found neglecting observed cirrus inhomogeneity over scales of typical climate model grid cells resulted in cirrus a_c and OLR biases of 11% and -14 W m^{-2} respectively. Therefore, neglecting cirrus inhomogeneity can lead to compensating effects because an overestimation of albedo effect results in a cool bias, and an underestimation of the cloud greenhouse effect results in a warm bias. For example, assuming a_c=0.15 and a_s=0.1 and using Eq. 1.4, the CRI bias resulting from a positive 11% a_{cirrus} bias and a negative 14 Wm^{-2} OLR bias would be – 9.0 Wm^{-2}. With 25% cloud cover, the CRF bias would be – 2.2 Wm^{-2} (Eq. 1.5).

Both surface properties and cirrus inhomogeneity influence the magnitude of radiative flux biases. For typical a_s (a_s <0.3), neglecting cirrus inhomogeneity results in a positive albedo bias because of the convex relationship between cirrus a_c and σ. However, the non-linear relationship between σ and cirrus a_c depends on a_s (Carlin et al., 2002). As a result of the concave relationship between σ and OLR, PPH calculations will always underestimate OLR when cirrus inhomogeneity is neglected (Fu et al., 2000). For a given cirrus inhomogeneity, OLR biases increase with the difference between T_s and T_c (Figure 1.3). Based on the findings of Fu et al. (2000) and Carlin et al. (2001), OLR biases dominate the total CRI bias that results from neglecting cirrus inhomogeneity. We focus on the calculation of OLR biases in this dissertation.

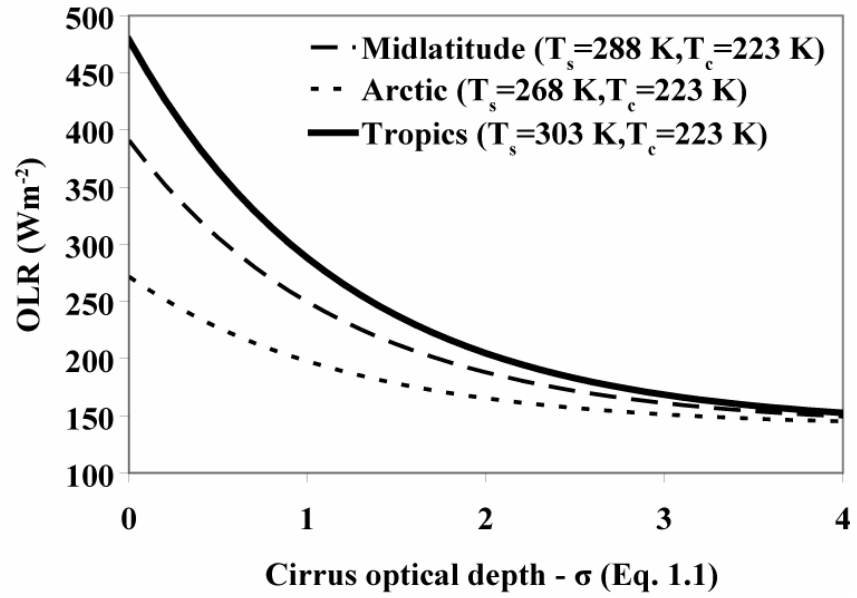

Figure 1.3: Concave relationship between OLR and σ. PPH OLR biases increase with the concavity of the relationship between OLR and cirrus σ. Therefore, the largest PPH OLR biases occur when there are large difference between T_s and T_c. We calculated OLR using Eq. 1 of Fu et al. (2000), which neglects the atmosphere.

1.3. Cirrus formation and N_{ice}

In the upper troposphere, ice crystals form by homogeneous freezing of liquid aerosols and by heterogeneous freezing processes involving both liquid and solid aerosol particles. The freezing threshold, i.e., the temperature and relative humidity where ice forms, and resulting N_{ice} depends on the freezing mechanism. For a fixed temperature or ice water content (IWC), N_{ice} determines R_{eff}. Given the importance of N_{ice} to σ (Eq. 1.1), we briefly review the current understanding of heterogeneous and homogeneous freezing.

At temperatures below 0 °C and humidities above ice saturation, the N_{ice} resulting from heterogeneous freezing depends on the number concentration of active ice nuclei (IN) (N_{IN} - # cm^{-3}). IN are insoluble aerosols that provide surfaces for heterogeneous nucleation. Observations show that background immersion IN concentrations are smaller (N_{IN} = 0.001-0.1 cm^{-3}, ((Rogers et al, 1998), (DeMott et al., 2003a))) than total aerosol concentrations (N_{aer} = 10-300 cm^{-3}, (Minikin et al. 2003)) but can approach typical N_{ice} (N_{ice}=0.001-10 cm^{-3}) (Lynch et al., 2002). Large N_{IN} (N_{IN}> 0.1 cm^{-3}) have been observed during dust storms (e.g., DeMott et al. (2003b)), but most existing observations suggest that large N_{IN} are not typical ((Rogers et al, 1998), (DeMott et al.,

2003a)). In addition to immersion heterogeneous nucleation, there are many heterogeneous nucleation pathways whose atmospheric relevance remains unknown. For example, laboratory studies have demonstrated that heterogeneous nucleation can result from solid inclusions of crystallized letovicite (Zuberi et al., 2001), contact nucleation (e.g., Durant and Shaw (2005)), and nucleation of secondary crystalline organics (e.g., Gavish et al. (1990), Seeley and Seidler (2001), Zobrist et al. (2006), Beaver et al. (2006)).

At temperatures below ~-40 °C and large ice saturations, liquid aerosols can freeze homogeneously. Parcel model studies demonstrate that the N_{ice} resulting from homogeneous freezing increases with vertical velocity and decreasing temperature (Lin et al., 2002). Unlike warm clouds (Twomey, 1974), parcel modeling also suggests N_{ice} is relatively insensitive to N_{aer} ((Jensen and Toon, 1994),(Lin et al. 2002)) and the details of the aerosol size distribution (Kärcher and Strom, 2003). Koop et al. (2000) used laboratory measurements to demonstrate that homogeneous nucleation rates (J_{hom} - m^{-3} sec^{-1}) depend only on aerosol water activity and temperature. When aerosols are in equilibrium with their environment and when the Kelvin (size) effect is negligible, the aerosol water activity is equivalent to the ambient relative humidity (RH - %). Koop et al. (2000)'s results have been used to simplify the treatment of homogeneous freezing (e.g., Kärcher and Lohmann (2002)).

1.4. Climate model representation of cirrus

Climate model grid cells (10^6 m) are much larger than the scales of radiatively important cirrus inhomogeneity (10^2 to 10^3 m). Difficulties in using the available model resolution to represent the observed cloud variability, and the lack of knowledge about cirrus processes, create significant uncertainty in modeled cirrus inhomogeneity and radiative impacts.

Most climate models predict cloud evolution using a prognostic bulk mixing ratio variable and a fixed partitioning of the ice and liquid phases (e.g., NCAR's CAM2 (Boville et al., 2001), NASA GISS's model (Delgenio,1996), UKMO's HADCM3 (Pope et al., 2000)). For the upcoming 2007 IPCC report, some modeling centers are predicting distinct cloud ice and cloud water variables as promoted by Fowler et al. (1996) and Lohmann and Roeckner (1996) (e.g., GFDL's CM2.0 (Delworth et al., 2006), NCAR's CAM3 (Boville et al., 2006), MPI's ECHAM5

(Roeckner et al., 2003)). However, other climate models are still using one prognostic cloud variable (e.g., NASA GISS's ModelE (Schmidt et al., 2006)) or diagnostic clouds (e.g., CCCma's CGCM3 (Knut von Salzen, personal communication)). In principle, prognostic cloud schemes are more physically realistic than diagnostic cloud schemes (Rasch and Kristjansson, 1998), and the use of distinct ice and water mixing ratios is more realistic than the use of a single mixing ratio with fixed temperature partitioning. In reality, all cloud schemes must represent complex microphysical processes with large-scale predicted variables such as temperature, vertical velocity, and relative humidity. Because many physical processes remain unresolved, climate models still diagnose many key cloud variables including cf, particle size, and particle number concentration.

Although many climate models predict cloud water, cirrus properties are largely prescribed. In most climate models, cirrus formation temperature, N_{ice} , R_{eff}, and cf are highly parameterized. For example, cirrus N_{ice} and R_{eff} are often diagnosed as a function of temperature or height (e.g., Bolville et al. (2006)), and cirrus cf is often diagnosed using large-scale relative humidity (e.g., Sundqvist et al. (1989) and Chabouureau and Bechtold (2002)). To compensate for biases that result from neglecting cloud inhomogeneity, climate modelers often scale cloud properties such as the σ (e.g., Schmidt et al. (2006)). The radiative impact of simplifying cirrus inhomogeneity is significant. For example, Gu and Liou (2006) found 7 Wm^{-2} TOA flux differences when they compared a climate model simulation that used an σ reduction factor of 0.7 with a climate model simulation that incorporated observed horizontal cirrus inhomogeneity from ISSCP data. Gu and Liou (2006)'s results demonstrate that the representation of cirrus inhomogeneity has significant impact on model radiative forcing and climate.

1.5. Summary and overview of completed research

In this introductory chapter, we used simple calculations and previously published research to establish that:

- The magnitude and the sign of cirrus CRF and CRI depend on cirrus inhomogeneity, T_c, and surface properties.
- Large and compensating cirrus a_c and OLR biases result from neglecting cirrus inhomogeneity.

- Although heterogeneous nucleation processes with unknown atmospheric relevance exist, N_{IN} measurements are available and Koop et al. (2000) is a well-established parameterization of homogeneous freezing.
- Improving representation of cirrus radiative impacts in physically-based climate models requires accurate parameterization of cirrus inhomogeneity, T_c, and surface properties.

In this dissertation, we assess which physical processes have the largest influence on cirrus inhomogeneity and radiative impacts. Throughout our work, we measure inhomogeneity with an σ distribution (P(σ)), i.e., the probability density function of cirrus σ. We found P(σ) to be a useful definition of cirrus inhomogeneity for two reasons. First, using P(σ) provided a simple framework for relating physical processes to cirrus inhomogeneity. Second, improved understanding of the controls on P(σ) can be incorporated into physically-based climate model radiative transfer calculations.

We estimate P(σ) over different spatial and temporal domains For example, we calculate P(σ) over the duration of Lagrangian parcel model experiments. We also use σ time series at a single location to measure P(σ). In contrast, P(σ) in climate models represent a large spatial domain at a single model time step. Clearly, direct comparison between these frameworks requires temporal stationarity and spatial uniformity assumptions that do not always apply. Nevertheless, our estimates of P(σ) should be useful for understanding the causes for P(σ) shape, regardless of the time spatial or temporal domain under consideration.

In Chapter 2, we describe microphysical and dynamical controls on cirrus P(σ) using algebra and numerical modeling experiments. Many of the results presented in Chapter 2 are based on a paper entitled "Microphysical and dynamical controls on cirrus optical depth distributions" Kay et al (in press) (hereafter K06, Appendix A). First, we approximate cirrus σ evolution with simplified algebraic equations. Then, we introduce our adiabatic parcel model with binned microphysics, a key tool for our research. Next, we use our parcel model to find the main controls on cirrus P(σ) shape along idealized trajectories. We compare the influence of homogeneous and heterogeneous nucleation on P(σ) shape using the observed N_{IN}, J_{hom} calculated using Koop et al. (2000), and a plausible range of vertical velocities and temperatures. Motivated

by recent laboratory measurements (Magee et al., 2006), we also present and discuss the effect of varying the deposition coefficient (α_{ice}) on cirrus properties and timescales. The α_{ice} sensitivity tests were not included in K06. The insights gained from Chapter 2 provide a useful framework for understanding the main physical controls on observed cirrus P(σ) shapes.

In Chapter 3, we analyze a rich cirrus climatology from Lamont, Oklahoma (OK), and assess the primary controls on cirrus inhomogeneity using insights from modeling and observational constraints. First, we present a summary of pre-existing cirrus observations and our new observations of upper tropospheric humidities, cirrus macrophysical properties, and cirrus P(σ). Then, using our cirrus P(σ) observations, we calculate the magnitude of typical PPH OLR biases and evaluate strategies for reducing PPH OLR biases. Finally, by combining a conceptual cirrus model with the observational constraints, we describe the main factors that control cirrus presence and inhomogeneity (i.e., P(σ)).

In Chapter 4, we evaluate the microphysical and dynamical controls on orographic cirrus P(σ) along realistic upper tropospheric trajectories. On April 19, 2001, GOES infrared imagery revealed cirrus formation in the lee of the Southern Rocky Mountains. The cirrus were advected by a broad 300-mb ridge and observed ~ 5-6 hours after formation at Lamont, OK. Using trajectories from a mesoscale weather model, the goal of Chapter 4 is to assess the effect of gravity waves and IN on cirrus cloud cover, $P(N_{ice})$, and P(σ).

In the last chapter of this dissertation, Chapter 5, we summarize the results from the three research chapters. We also suggest directions for future research based on the primary findings of our work.

Chapter 2:
CIRRUS P(σ) ALONG IDEALIZED TRAJECTORIES

2.1. Introduction and chapter organization

As described in Chapter 1, large OLR and albedo biases can result from neglecting cirrus inhomogeneity ((Fu et al., 2000), (Carlin et al., 2001)). We use P(σ), i.e., the probability density function of σ, to measure cirrus inhomogeneity. In climate and weather models, P(σ) over a large spatial domain at a single model time step can be approximated as a gamma distribution whose two fit parameters ($\overline{\sigma}$,ν) are determined by the mean σ ($\overline{\sigma}$) and the standard deviation in σ (std(σ)) (Fu et al., 2000):

$$P(\sigma) = \frac{1}{\Gamma(\nu)}\left(\frac{\nu}{\overline{\sigma}}\right)^{\nu} \sigma^{\nu-1} \exp^{-\frac{\nu\sigma}{\overline{\sigma}}} \tag{2.1}$$

where $\nu = \left(\frac{\overline{\sigma}}{std(\sigma)}\right)^2$ and Γ (ν) is the gamma function.

In this chapter, we use algebra and Lagrangian parcel model experiments to assess how microphysics and dynamics influence cirrus P(σ) and P(σ) gamma distribution fit parameters. Throughout this chapter, we refer to K06 (Appendix A), in which we summarized the main controls on cirrus P(σ) in parcel model experiments and compared observed P(σ) to modeled P(σ).

The chapter is structured as follows: First, we review K06's algebraic approximations of the main controls on cirrus σ evolution. Next, we introduce our adiabatic parcel model, the primary tool we used for assessing the influence of microphysics and dynamics on cirrus P(σ) along Lagrangian trajectories. We then summarize and discuss the main results of K06. In K06, we assumed that the deposition coefficient for ice (α_{ice}) was unity, but α_{ice} is an uncertain parameter (e.g., Magee et al. (2006), Haynes et al. (1992)). Therefore, we present and discuss the

effect of varying α_{ice} on cirrus cloud properties and microphysical timescales. Finally, we summarize our most important findings and discuss how they motivate the research presented in Chapters 3 and 4 of this dissertation.

2.2. Cirrus σ evolution

In K06, we approximated the Lagrangian σ evolution by taking time derivative of Eq. 1.1, and substituting the diffusional growth equation and the time derivative of N_{ice} due to freezing and fallout:

$$\frac{d\sigma}{dt} = 2\pi\Delta z R_{eff}{}^2 P_f\left(J, r_{aer}\right)N_{aer} + \frac{4\pi\Delta z}{\rho_{ice}}\alpha_{ice} D\rho_{sat}(T,P)S_i N_{ice} \ldots - \frac{\sigma V_{fall}(R_{eff})}{H} \tag{2.2}$$

where P_f is the probability of aerosol freezing (sec^{-1}), J is the freezing rate (m^{-3} sec^{-1}), r_{aer} is the aerosol radius (m), N_{aer} is the number concentration of aerosol (m^{-3}), α is the deposition coefficient (unit less), ρ_{ice}=density ice (kg m^{-3}), D is the vapor diffusivity ($m^2 sec^{-1}$), ρ_{sat} is the saturation vapor density (kg m^{-3}), T is the temperature (K), P is the pressure (Pa), S_i is supersaturation with respect to ice (%), V_{fall} is the ice crystal fall speed (m sec^{-1}), and H is the depth ice crystals must fall to be removed from the nucleating region of the cloud (m). Note: In section 2.3 and K06, we include a more thorough description of H.

From Eq. 2.2, we see that the main processes controlling the time evolution of σ are new freezing events, growth of existing ice crystals, and fallout of existing ice crystals. The σ evolution and P(σ) depend on the typical timescales for these microphysical processes. Therefore, Eq. 2.2 can be written in a schematic form with characteristic timescales:

$$\frac{d\sigma}{dt} \sim \frac{\sigma}{\tau_{freezing}} + \frac{\sigma}{\tau_{growth}} - \frac{\sigma}{\tau_{fallout}} \tag{2.3}$$

where $\tau_{freezing}$ is the freezing timescale (minutes), τ_{growth} is the growth timescale (minutes), and $\tau_{fallout}$ is the fallout timescale (minutes).

Dynamics influence cirrus $P(\sigma)$ by controlling the time evolution of S_i and T (see Eq. 2.2). Therefore, in K06 we compared typical microphysical timescales (Eq. 2.3) with typical timescales for both generation of ice supersaturation by lifting ($\tau_{lift\text{-}hom}$ – minutes, $\tau_{lift\text{-}het}$ – minutes) and temperature fluctuations (τ_{wave} – minutes).

2.3. Adiabatic parcel model with binned ice microphysics

In order to calculate the Lagrangian cirrus σ evolution (Eq. 2.2) and characteristic $\tau_{freezing}$, τ_{growth}, and $\tau_{fallout}$ (Eq. 2.3), we developed an adiabatic parcel model with binned ice microphysics. The model processes and validation are both described in K06. See K06 section 2.3.3 for a detailed description of timescale calculation methods and K06 Tables 2, 4, and 5 for typical timescale values. Here, we review two essential features of our model: 1) the relationship between zero-dimensional parcel model output and three-dimensional cirrus processes and 2) our treatment of freezing.

2.3.1. Relating parcel model cirrus to cirrus in the atmosphere

A conceptual model is needed to relate parcel model output to cirrus processes occurring in the atmosphere (Figure 2.1). As described by K06, the key simplification in our conceptual model is that nucleation does not occur throughout the vertical extent of cirrus clouds. Based on this simplification, a cirrus cloud of depth Δz can be separated into an ice formation region of depth H, and an ice fallout region of depth Δz -H. We use the parcel model to simulate nucleation, growth, and fallout in the ice formation region. By assuming that cirrus cloud character is primarily determined by ice formation region, we can then estimate the σ using Eq. 1.1 with a fixed Δz of 1000 m and N_{ice} and R_{eff} calculated from the parcel model runs with H = 100 m.

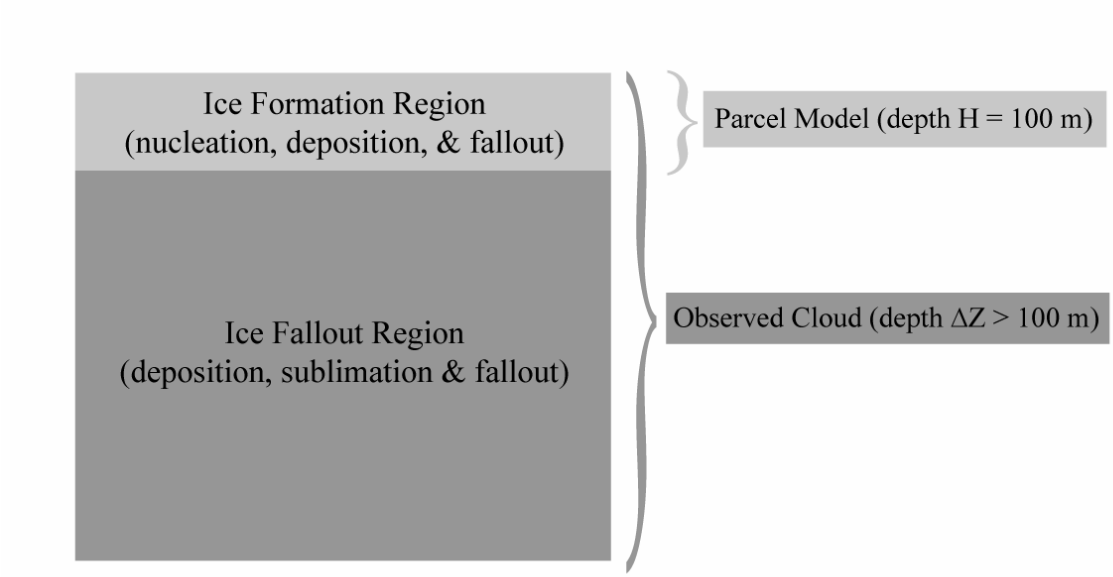

Figure 2.1: Cirrus conceptual model. We assume P(σ) shape is determined by processes occurring in an ice formation region of depth H near cloud top. We use our parcel model to represent nucleation, deposition and fallout occurring in the ice formation region. Then, we calculate cirrus optical depth (Eq. 1.1) by linearly scaling the ice formation region properties over the entire cloud depth ΔZ.

Limitations of this approach include the adiabatic assumption, the lack of radiative heating and cooling, and simplifications that are required to relate parcel model P(σ) to observed P(σ). In K06, we demonstrated that the adiabatic assumption and the lack of radiative heating and cooling are reasonable approximations because typical mixing timescales and radiative heating and cooling timescales are longer than typical microphysical and dynamical timescales in our parcel model. The most important limitations of our parcel model approach are related to the simplifications we use to relate parcel model output to observed cirrus. P(σ) is sensitive to the vertical interplay between the freezing, growth, and fallout processes. Although our selections for H and Δz are reasonable within the context of our cirrus conceptual model (Figure 2.1), both H=100 m and Δz =1000 m are ad hoc estimates. Variability in Δz or in the processes occurring below the formation layer would violate the method we use to estimate cirrus σ. P(σ) are sensitive to dispersion and shear in the atmosphere, which we neglect in our zero-dimensional calculations. Finally, P(σ) derived from idealized Lagrangian parcel model experiments cannot be directly compared to observed P(σ). P(σ) in the atmosphere result from both temporal and

spatial variability. Despite the described limitations, our approach allows direct attribution of $P(\sigma)$ shape to physical processes and the calculation of diagnostic timescales. Therefore, our research is a useful first step for assessing what controls $P(\sigma)$ in the atmosphere (see K06 and 1.5 for further discussion and justification).

2.3.2. Treatment of freezing in the K06 parcel model

Freezing determines N_{ice}. For a fixed IWC, N_{ice} determines R_{eff}. As a result, freezing controls two variables in Eq. 1.1, namely N_{ice} and R_{eff}. Given the importance of freezing to σ, we describe our parcel model's treatment of freezing.

The N_{ice} resulting from a homogeneous nucleation event (N_{ice}^{h} - # m^{-3}) in our parcel model is:

$$N_{ice}^{h} = \int_0^{\tau_{freezing}} J_{\hom}\left(RH(t),T(t)\right)\frac{4}{3}\pi r_{aer}(t)^3 N_{aer}(t)dt \qquad (2.4)$$

where J_{hom} is taken from Koop et al. (2000) (see K06 Eq. 2), and RH is the relative humidity (RH - %).

Freezing begins when RH exceeds $RH_{crit\text{-}hom}$, the critical RH required to start the stochastic homogeneous freezing of aerosols, i.e., the RH when $\frac{dN_{ice}}{dt} \sim 10^{-6}$ cm^{-3} sec^{-1}. Freezing continues until the growth of newly formed ice crystals reduces RH below $RH_{crit\text{-}hom}$, and stops the freezing i.e., when $\frac{dN_{ice}}{dt} < 10^{-6}$ cm^{-3} sec^{-1}. J_{hom} is a sharply increasing function of RH. As a result, N_{ice}^{h} is very sensitive to the maximum J_{hom} ($J_{hom\text{-}max}$).

Heterogeneous nucleation in the atmosphere may occur via many complex pathways (e.g., Zuberi et al. (2001), Gavish et al. (1990), Durant and Shaw (2005)) . As a result, a simple formulation for heterogeneous nucleation rates has not been developed. We investigate the influence of heterogeneous nucleation on σ evolution by including a specified N_{IN} that can act as

immersion ice nuclei. In K06, we assumed $0\ cm^{-3} < N_{IN} < 0.1\ cm^{-3}$, a range typical of background conditions in the Western USA ((DeMott et al., 2003a), (Rogers et al.,1998)). In all parcel model experiments, IN glaciate at RH_{ice} ~130% ((Kärcher and Lohmann, 2003); see K06 Eq. 3).

2.4. Summary of results from K06

In K06, we investigated the primary controls on P(σ) by comparing microphysical and dynamical timescales along idealized lifting and wave trajectories (see K06 Eq. 7, K06 Table 1). We found that P(σ) shape depends primarily on the ratio of $\tau_{fallout}$ to timescales of other microphysical and dynamical processes. Here, we review several key specific results from our paper.

In model runs where a parcel was lifted 1000 m at a constant vertical velocity ($\overline{w}$), cirrus P(σ) shape depended on R:

$$R \equiv \frac{\tau_{fallout}}{\tau_{growth}} \tag{2.5}$$

For homogeneous nucleation, R was primarily determined by $\overline{w}$. With large $\overline{w}$, R >1 whereas with small $\overline{w}$, R < 1. In these K06 model runs, $\overline{w}$ was vertical velocity during homogeneous nucleation (w^h). Therefore, as $\overline{w}$ increased, $J_{hom\text{-}max}$ increased, $N_{ice}{}^h$ increased, and R_{eff} decreased. Because Δz was fixed at 1000 m, $\overline{w}$ controlled σ (Eq. 1.1), τ_{growth} and $\tau_{fallout}$ (Eq. 2.2, Eq. 2.3), and cirrus P(σ) shape in the K06 experiments.

Using R, we identified two P(σ) regimes: limited fallout (R > 1) and fallout dominated (R < 1) (Table 2.1, K06 Figures 3, K06 Figure 8). With R > 1, cirrus P(σ) were peaked at large σ (σ > 1) because ice crystals stayed with the parcel. In this limited fallout regime (R > 1), $\tau_{lift\text{-}het}$ /τ_{growth} was large and glaciated IN could not prevent homogeneous freezing. However, as a result

of large $\tau_{fallout}/\tau_{lift\text{-}het}$, glaciated IN stayed with the parcel, reduced $J_{hom\text{-}max}$ and N_{ice}^{h} (Eq. 2.4), and modified P(σ) (Table 1.1). With R < 1, P(σ) monotonically decreased. In this fallout-dominated regime (R < 1), glaciated IN had little impact on P(σ) shape because they quickly fell out (small $\tau_{fallout}/\tau_{lift\text{-}het}$) and because N_{IN} were similar to N_{ice}^{h}.

Table 2.1: P(σ) shapes and gamma distribution fit parameters. In the idealized lifting experiments (K06), P(σ) shape and P(σ) gamma distribution fit parameters depend on R (Eq. 2.5).

Regime	**P(σ) description**	**P(σ) gamma fit parameters**
Limited fallout (R > 1)	P(σ) peaked at large optical depths (σ > 1)	large $\overline{\sigma}$ and ν > 1
Limited fallout (R > 1) with IN	P(σ) peaked at large σ and had a monotonically decreasing tail at low σ	This shape cannot be reproduced by a single gamma distribution
Fallout dominated (R < 1)	P(σ) monotonically decreasing and dominated by small σ	small $\overline{\sigma}$ and ν ≤ 1

Sinusoidal temperature fluctuations influenced P(σ) only when $\tau_{growth} < \tau_{wave} < \tau_{fallout}$, or τ_{wave} approached or exceeded $\tau_{freezing}$. We found that with R > 1, mesoscale fluctuations (τ_{wave} ~ 16 minutes) with a temperature amplitude ΔT=2 K broadened P(σ) (K06 Figure 9). Broadening P(σ) could be represented in a gamma distribution by decreasing ν. Temperature fluctuations resulted in new freezing events and affected P(σ) when RH exceeded RH_{crit} and τ_{wave} approached or exceeded $\tau_{freezing}$

2.5. The uncertain deposition coefficient (α_{ice})

The diffusional growth of ice crystals depends on α_{ice}, i.e., the fraction of impinging water vapor molecules that are incorporated into an ice crystal lattice (see Pruppacher and Klett (1997), Eq. 2.2). Unfortunately, α_{ice} is a highly uncertain parameter. Reviews of laboratory measurements suggest that α_{ice} could be as low as 0.001 and as high as 1 (Haynes et al., 1992), but recent laboratory measurements found α_{ice}=0.006 (Magee, 2006). Decreasing α_{ice} slows ice crystal growth (Eq.2.2) and the drawdown of S_i,. Indeed, low α_{ice} has been proposed as an explanation for atmospheric observations of large S_i (Peter et al., in prep). Throughout K06, we

assumed α_{ice} =1. For our P(σ) research, understanding how α_{ice} affects N_{ice}^{h} is crucial because N_{ice}^{h} affects cirrus microphysical timescales (Eq. 2.3) and R (Eq. 2.5). Here, we discuss the effect of varying α_{ice} on N_{ice}^{h} and the sensitivity of N_{ice}^{h} to N_{aer}. We then combine our modeling with observations (Kärcher and Strom, 2003) to constrain plausible α_{ice}.

Our parcel model sensitivity tests confirmed Gierens et al. (2003)'s results: N_{ice}^{h} is relatively insensitive to α_{ice} when $0.1 < \alpha_{ice} < 1$, but N_{ice}^{h} increases dramatically when $\alpha_{ice} < 0.1$ (Figure 2.2a, Table 2.2). In our parcel model, increasing N_{ice}^{h} at low α_{ice} resulted from an increase in $J_{hom\text{-}max}$ and $\tau_{freezing}$ (Figure 2.2b&c, Table 2.2).

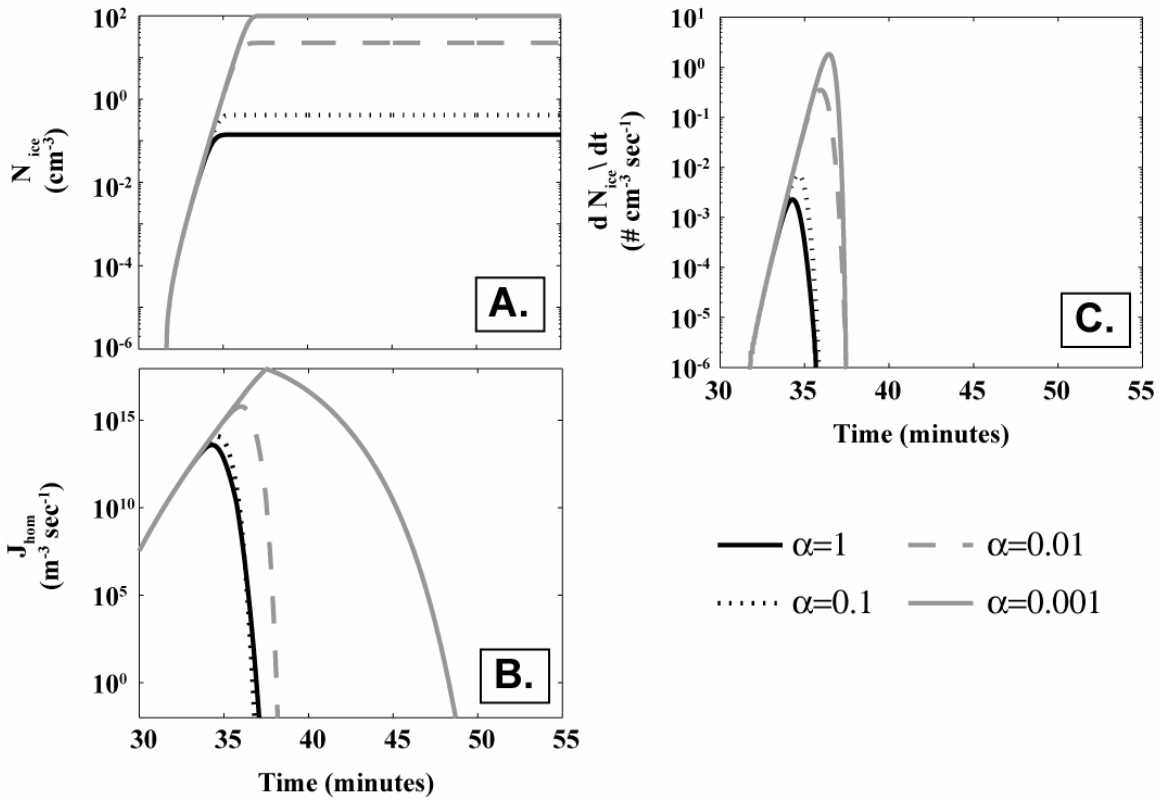

Figure 2.2: Influence of α_{ice} on homogeneous freezing. N_{ice}^{h} increased as α_{ice} decreased because $J_{hom\text{-}max}$ and $\tau_{freezing}$ increased (Table 2.2). Parcels started with N_{aer}=100 cm^{-3} at RH_{ice}=120% and T=-50 °C and were lifted at $\overline{w}$=10 cm sec^{-1}.

Table 2.2: Influence of α_{ice} on homogeneous freezing. See Figure 2.2 for description.

α_{ice}	N_{ice}^{h} (# cm^{-3})	$J_{hom\text{-}max}$ (m^{-3} sec^{-1})	$\tau_{freezing}$ (min)	τ_{growth} (min)
1	0.18	3.9 e+013	4.1	8.9
0.1	0.92	1.9 e+014	4.3	5.9
0.01	22.3	6.2 e+015	5.9	4.5
0.001	100.0	8.8 e+017	5.9	23.3

We also found that the sensitivity of N_{ice}^{h} to α_{ice} depended on w^h. For $0.001 < \alpha_{ice} \leq 1$, $J_{hom\text{-}max}$ and the fraction of N_{aer} that froze increased with w^h (Figure 2.3).

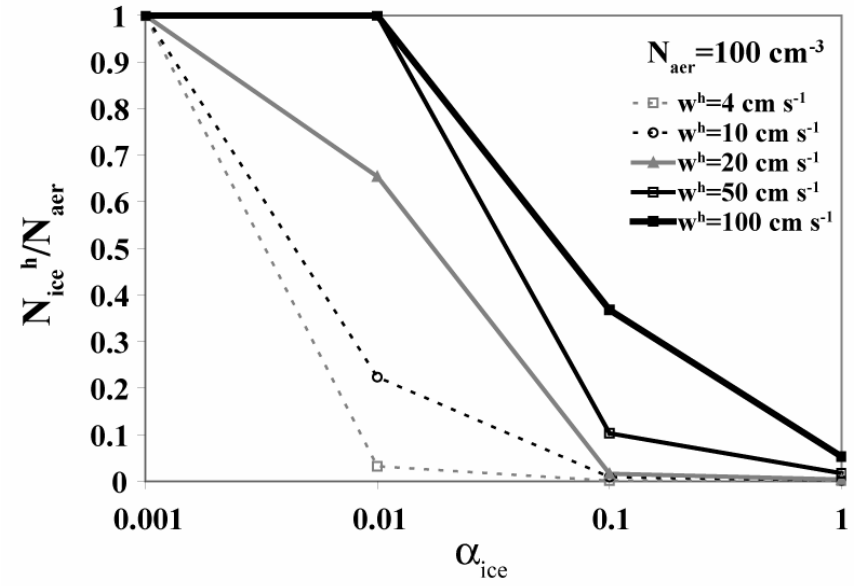

Figure 2.3: Influence of α_{ice} on homogeneous freezing as a function of vertical velocity. For $0.001 < \propto_{ice} \leq 1$, $J_{hom\text{-}max}$ and $\frac{N_{ice}^{h}}{N_{aer}}$ increased with w^h. Parcels started at RH_{ice}=120% and T= -50 °C.

Previous studies have demonstrated that the Twomey effect (Twomey, 1974), i.e., the sensitivity of N_{ice} to N_{aer}, is not an important effect for cirrus (e.g., DeMott et al. (1997), Jensen and Toon (1994)). In these models, $\alpha_{ice} > 0.1$ and N_{aer} did not affect N_{ice} because the efficient growth of a few ice crystals quickly reduced RH below RH_{crit} and stopped the freezing of

supercooled aerosols (Eq. 2.4). In agreement with previous research, N_{ice} was insensitive to N_{aer} with α_{ice}=1 (Figure 2.4).

With low α_{ice}, however, N_{ice} was very sensitive to N_{aer} (Figure 2.5). The sensitivity of N_{ice} to N_{aer} increased with $\alpha_{ice} < 0.1$ because newly formed ice crystals grew inefficiently and allowed larger $J_{hom\text{-}max}$, longer $\tau_{freezing}$, and a larger fraction of the available N_{aer} to freeze. With α_{ice}=0.001 and $w^h > 4$ cm sec^{-1}, N_{aer} equaled $N_{ice}{}^h$ (Figure 2.5). When N_{ice} was sensitive to N_{aer}, $\tau_{freezing}$ increased with N_{aer} (Table 2.3). Even though $\tau_{freezing}$ increased due to slow initial ice crystal growth, τ_{growth} as defined in K06 decreased because N_{ice} increased with N_{aer}.

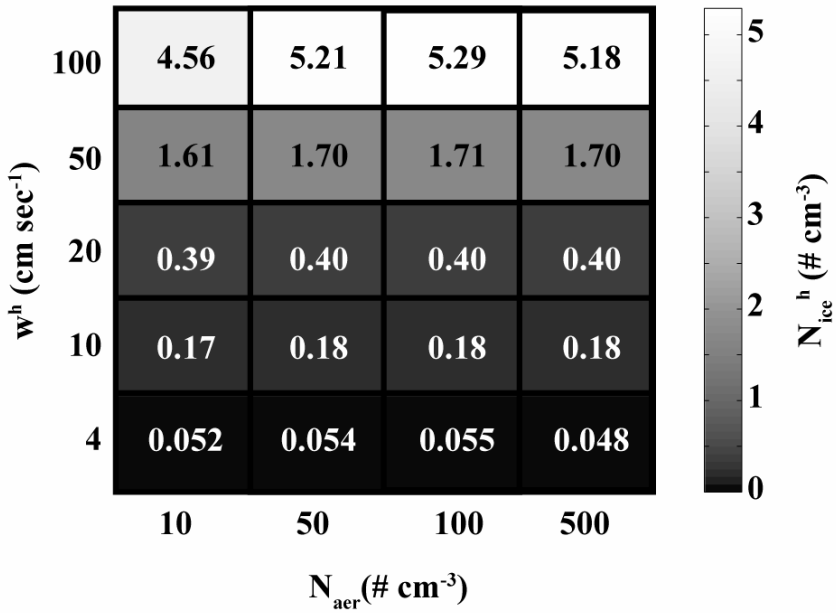

Figure 2.4: Vertical velocity controls ice number concentrations with α_{ice}=1. With α_{ice}=1, $N_{ice}{}^h$ depended primarily on w^h and was insensitive to N_{aer}. Parcels started RH_{ice}=120% and T= -50 °C.

Table 2.3: Aerosol number concentration controls ice number concentration with small α_{ice}. In idealized lifting experiments, N_{aer} determined N_{ice}^{h} when α_{ice}=0.001. Even though $\tau_{freezing}$ increased with N_{aer}, τ_{growth} as defined by K06 decreased because N_{ice}^{h} increased with N_{aer}. All parcel model runs started at RH_{ice}=120% and T=-50 °C and lifted at $\overline{w}$=10 cm sec^{-1}. For these experiments, $\overline{w}$=w^{h}.

N_{aer} (# cm^{-3})	N_{ice}^{h} (# cm^{-3})	$J_{hom\text{-}max}$ (m^{-3} sec^{-1})	$\tau_{freezing}$ (min)	τ_{growth} (min)
10	10.0	9.4 e+017	5.0	57.5
50	50.0	9.4 e+017	5.6	31.1
100	100.0	8.8 e+017	5.9	23.3
500	499.2	9.4 e+016	9.6	11.8

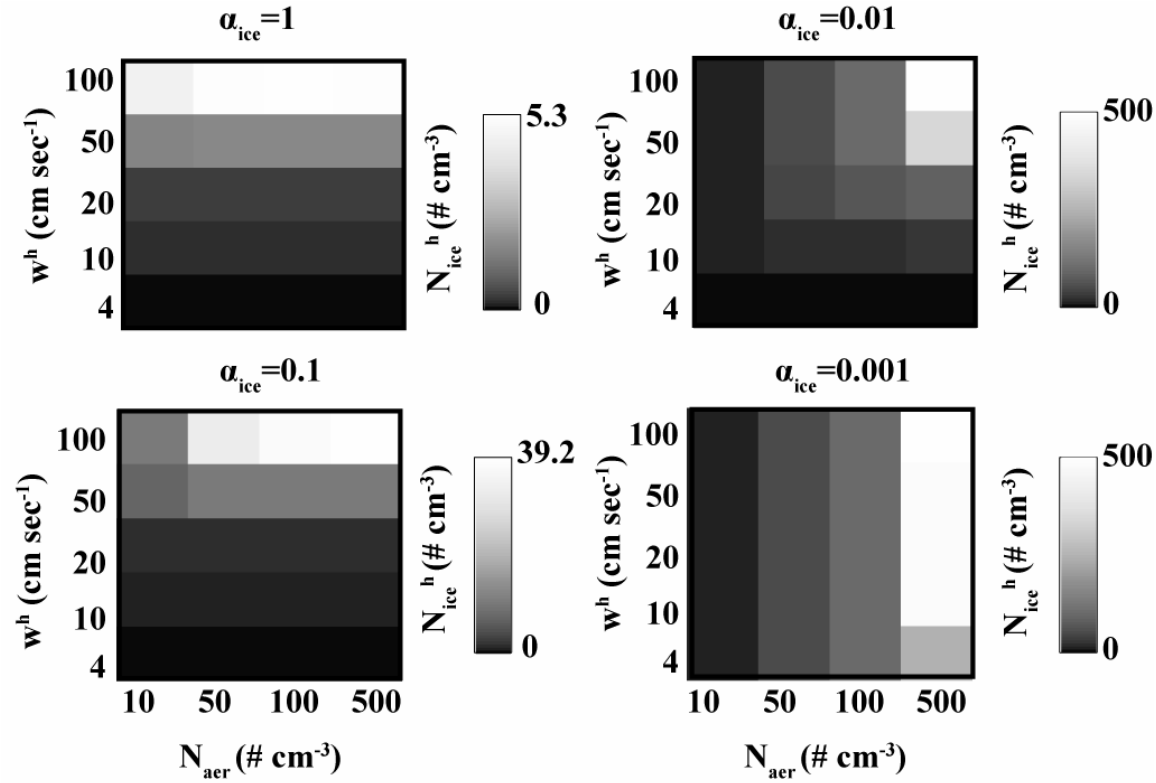

Figure 2.5: Controls on ice number concentrations with variable α_{ice}. As α_{ice} decreased, N_{ice}^{h} switched from depending primarily on w^{h} to depending primarily on N_{aer}. Parcels started at RH_{ice}=120% and T= -50 °C.

An obvious limitation of our estimated sensitivity of N_{ice} to N_{aer} with low α_{ice} is the simplistic treatment of aerosols in our parcel model. Although using monomodal sulfuric acid

aerosols can be justified when $\alpha_{ice} = 1$, the details of the aerosol size distribution and water uptake could influence the magnitude of the sensitivity N_{ice} to N_{aer} described in this work.

An extreme dependence of N_{ice} on N_{aer} is not consistent with atmospheric observations. In general, observed N_{ice} (0.001-10 cm^{-3}) are much lower than N_{aer} (10-300 cm^{-3}). During the INCA field campaign, N_{aer} in the polluted northern hemisphere above Prestwick, Scotland were 2-3 times greater than N_{aer} in the relatively pristine southern hemisphere above Punta Arenas, Chile (Minikin et al., 2003). Although N_{ice} were larger at Prestwick than at Punta Arenas, Kärcher and Strom (2003) concluded that the N_{ice} distributions for cirrus with similar vertical velocities were "strikingly similar" and that the "properties of the freezing aerosol particles do not strongly affect the number distribution of ice crystals in cirrus". Based on these cirrus observations, which show little dependence of N_{ice} on N_{aer}, and our parcel modeling, we suggest $\alpha_{ice} > 0.1$ in the atmosphere.

2.6. Summary

In summary, the main findings of this chapter and in K06 were:

- Microphysical and dynamical timescales control the evolution of cirrus σ (Eq. 2.2).
- Along idealized lifting trajectories, cirrus P(σ) shape depended on R (Eq. 2.5). With R > 1, cirrus had long lifetimes and P(σ) peaked at large values (σ > 1). With R < 1, cirrus had short lifetimes and P(σ) decreased monotonically.
- Along idealized lifting trajectories, w was the most important control on R and P(σ).
- With background IN concentrations ($N_{IN} < 0.1$ cm^{-3}) and scavenging, IN had little influence on cirrus σ along idealized lifting trajectories. IN never prevented homogeneous nucleation and IN influenced P(σ) shape only when R > 1.
- Temperature oscillations influenced P(σ) when $\tau_{growth} < \tau_{wave} < \tau_{fallout}$, or when τ_{wave} approached or exceeded $\tau_{reezing}$. When R > 1, mesoscale waves with appreciable ΔT (e.g., ΔT = 2 K in K06) broadened P(σ).

- With low α_{ice} measured in some laboratory experiments (Magee et al., 2006), N_{ice}^{h} and the sensitivity of N_{ice}^{h} to N_{aer} increased. The modeled sensitivity of $\frac{N_{ice}^{h}}{N_{aer}}$ to α_{ice} increased with w^{h}. However, atmospheric observations from the INCA field campaign revealed little dependence of N_{ice} on N_{aer} (Kärcher and Strom, 2003) and are therefore inconsistent with $\alpha_{ice} << 0.1$. Based on the INCA observations and our parcel modeling experiments, we suggest $\alpha_{ice} > 0.1$ in the atmosphere.

The findings of this chapter motivate a simple question: what model parameter space do cirrus $P(\sigma)$ in the atmosphere occupy? To address this question, atmospheric observations are required. In the next chapter (Chapter 3), we combine our understanding of what controls cirrus $P(\sigma)$ in idealized experiments with a cirrus climatology from Lamont, Oklahoma (OK). Using the observed cirrus cloud properties, including $P(\sigma)$, we assess what controls cirrus inhomogeneity in the atmosphere. The insights gained from this chapter provide a useful framework for understanding the microphysical and dynamical controls on mid-latitude cirrus $P(\sigma)$ observations.

Chapter 3:

CONSTRAINTS ON CIRRUS P(σ) CONTROLS FROM A MID-LATITUDE CLIMATOLOGY

3.1. Introduction

3.1.1. Motivation and research questions

In Chapter 2 and K06, we used a parcel model and idealized trajectories to calculate cirrus σ for an atmospherically relevant range of w, T, N_{IN}, N_{aer} and α_{ice}. We concluded that $\overline{\sigma}$ and the shape of cirrus P(σ) depend primarily on w. Given these and other modeling results described in Chapter 2 and K06, a clear question emerges: What range of model parameter space do cirrus in the atmosphere occupy? Addressing this question requires observations of cirrus environments and cirrus cloud properties.

In this chapter, we analyze climatological cirrus observations from the Atmospheric Radiation Measurement (ARM) Southern Great Plains (SGP) site in Lamont, OK (36.6 ° N, 97.5 ° W). We describe typical cirrus and their environment, quantify cirrus inhomogeneity and radiative impacts, and evaluate the processes controlling cirrus presence and inhomogeneity, i.e., P(σ). Our goal is to answer the following research questions:

- What are typical cirrus P(σ)?
- What is the effect of observed cirrus inhomogeneity on computed OLR?
- Do Lamont, OK cirrus observations provide obvious constraints on the physical processes controlling cirrus presence and P(σ)?

3.1.2. Chapter organization

In 3.2 and 3.3, we describe our analysis techniques and present our results. To address our research questions, we examine observations of:

1) T and relative humidity with respect to ice (RH_{ice}) in and around cirrus

2) cirrus macrophysical properties and their dependence on T, local static stability (Φ - K/km), and season.

3) cirrus σ and P(σ) shapes including the probability distribution of P(σ) gamma distribution fit parameters ($\overline{\sigma}$, ν in Eq. 2.1)

We also compare OLR estimated using the observed P(σ), the observed $\overline{\sigma}$, and gamma-distribution fits to the observed P(σ). Our observational analyses contribute to a rich existing cirrus climatology from Lamont, OK (Table 3.1). In 3.4, we combine observations and simple models to assess what variables control the observed cirrus P(σ). We conclude that mesoscale (spatial scale 100-1000s meters) variability in w^h and variability in the depth and T of elevated saturated layers can explain observed cirrus inhomogeneity. To justify this conclusion, we investigate what controls the three variables determine cirrus σ (Eq. 1.1): the N_{ice}, R_{eff}, and Δz. N_{ice} is particularly important because at a fixed IWC, N_{ice} primarily controls R_{eff}. Therefore, we first assess if observations can be used to constrain the relative role of homogeneous and heterogeneous nucleation. After finding that homogeneous nucleation alone can explain the Lamont, OK cirrus N_{ice} observations, we use our parcel model to calculate the w^h required to generate the observed N_{ice}. We find that mesoscale variability in w^h is required to explain the observed N_{ice} distribution. Next, we assess what could control observed Δz distributions. We describe why the depth and T of elevated saturated layers control Δz distributions, and why sublimation timescales below cirrus are uniformly short. In section 3.5, we summarize our findings and discuss lessons learned for incorporating cirrus inhomogeneity into model parameterizations.

Table 3.1: Previously published Lamont, OK cirrus observations

Study	Data used	Variables	Main findings
Mace et al. 2001 (MCA)	1 year of millimeter cloud radar (mmcr) data, Rapid Update Cycle (RUC) model	cirrus presence, synoptic vertical velocities (w_{syn}), ~135 hours of thin cirrus ($\sigma < \sim 2.4$) microphysical properties (Mace et al., 1998a)	♦ 22% presence, heights=8.5-10 km, temperatures (T) =-36 to -62 ºC, $\Delta z = 2.0 \pm 1.4$ km. ♦ Higher summer heights, but mean T and Δz did not change seasonally. ♦ Mean w_{syn} +0.2 cm sec^{-1}, but 1/3 $w_{syn} < -1.5$ cm^{-1}. ♦ R_{eff}=35 µm, N_{ice}= 0.10 cm^{-3}. ♦ $R_{eff} \downarrow$ with T. $N_{ice} \uparrow$with T. ♦ Monotonically decreasing P(N_{ice})
Mace et al. 2006 (MBV)	6 years of mmcr and NCEP-NCAR reanalysis data	cirrus presence, w_{syn}, synoptic weather patterns, thin cirrus ($\sigma < \sim 2.4$) microphysical properties (Mace et al., 1998a)	♦ Deepening of the troposphere explains seasonal cirrus height change ♦ Cold season (NDJFM) cirrus associated with weather disturbances, warm season (AMJJASO) cirrus likely formed by convective detrainment ♦ Cirrus present with ascending and descending w_{syn} ♦ Cirrus coincident with $0<w_{syn}$ had higher ice water contents (IWC) than cirrus coincident with $w_{syn}<0$. ♦ Monotonically decreasing P(IWC) and P(σ)
Wang and Sassen (2002) (WS)	mmcr and Raman lidar data	cirrus P(σ), cirrus microphysical properties	♦ IWC and $R_{eff} \uparrow$ with T: IWC=3.5 ± 5.0 mg m^{-3}, R_{eff}=34 ± 18 µm, at -60 °C, IWC=15.7 ± 22.7 mg m^{-3}, R_{eff}=67 ±41 µm at -30 °C. ♦ σ=0.58 ± 0.67 and IWP =12.2 ± 19 gm^{-2} ♦ Monotonically decreasing P(σ)
Comstock et al. (2004) (CAT)	Raman lidar data, RUC model	Cirrus RH	♦ 31% of in-cloud $RH_{ice} > 100\%$. ♦ Compositing of data by position within cloud revealed that at cloud top, more air was supersaturated (43% in-cloud $RH_{ice} > 100\%$).

3.2. Retrieval and analysis techniques

We used Raman lidar (Goldsmith et al., 1998) and radiosonde profiles collected between January 1998 and September 2001 to observe cirrus and their environment. Here, we explain and discuss our data analysis strategy. We created four distinct datasets: cirrus cloud masks, temperature profiles, upper tropospheric RH_{ice} and cirrus optical depths. In Table 3.2, we describe these datasets. In Table 3.3, we define and describe the cirrus properties we calculated from these datasets. In Appendix B, we provide a more detailed description of our data analysis techniques.

Raman lidar and radiosonde data have obvious strengths for cirrus retrievals including unambiguous phase discrimination (Sassen et al., 1991), high sensitivity to small ice crystals and small σ, and a large database of coincident temperature, pressure, and wind vertical profiles. Despite these important strengths, data availability, lidar resolution, and lidar attenuation limited the continuity and accuracy of our retrievals.

3.2.1. Description of retrieval techniques

As described in Tables 3.2, 3.3 and Appendix B, we estimated T_c, RH_{ice}, and Φ, and cirrus macrophysical properties using Raman lidar and radiosonde observations. To assess the influence of T on cirrus presence, we calculated at each T_j:

$$P(Ci)_{T_j} \equiv \frac{N_{Ci}(T_j - \Delta T < T_j < T_j + \Delta T)}{N_{Ci}} \tag{3.1a}$$

$$P(Ci,T)_{T_j} \equiv \frac{N_{Ci}(T_j - \Delta T < T_j < T_j + \Delta T)}{N_T(T_j - \Delta T < T_j < T_j + \Delta T)} \tag{3.1b}$$

$$P(T)_{T_j} \equiv \frac{N_T(T_j - \Delta T < T_j < T_j + \Delta T)}{N_T} \quad (3.1c)$$

where $\Delta T = 2.5$ ° C, T_j=-72.5:5:-2.5 °C is the discretization over the range of observed cirrus temperatures, N_{Ci} is the total number of cirrus observations (cirrus ≡ DR > 10%), and N_T is the number of T observations.

We estimated RH_{ice} with Raman lidar-derived water vapor mixing ratios and linearly interpolated radiosonde data (Tables 3.2 and 3.3). Like Comstock et al. (2004) (hereafter CAT, see Table 3.1), we eliminated noise generated by solar radiation by only analyzing night-time data (0-12 UTC). Although our cirrus RH_{ice} analysis relied on similar data, our calculations differed from CAT in three ways: 1) we used concurrent radiosonde data to estimate T and P, 2) we estimated es_{ice} using Murphy and Koop (2005), and 3) we used a 10% DR threshold to define cirrus. At typical T_c (-50 °C), we found that typical errors in T_c and water vapor mixing ratio (±1 °C, ±20%) led to large uncertainty in computed RH_{ice} (29% at ice saturation and 44% at water saturation). Given our error calculations and the lidar specifications, we interpreted our retrieved RH_{ice} values with caution.

We defined Φ as:

$$\Phi \equiv \Gamma_{ice} - \Gamma_{obs} \quad (3.2)$$

where Γ_{ice} is the pseudoadiabatic lapse rate for ice (K km^{-1}) and Γ_{obs} is the observed lapse rate (K km^{-1}).

We documented Φ in and above cirrus using the radiosonde profiles. We used linear regressions and t-tests with a 99% confidence limit to evaluate the dependence of cirrus macrophysical properties on T_c and Φ.

Table 3.2: Cirrus dataset specifications. See Table 3.3 for cirrus properties retrieved using these datasets.

Dataset	Description	Measurement resolution	Data quality criterion	Data amount
Cirrus cloud masks	ice ≡ depolarization ratio (DR) > 10%	10 minute, 200-300 m vertical	continuous and low random error (<20%) depolarization observations, two radiosondes within the 12-hour period.	328 12-hour periods (0-12 UTC or 12-24 UTC)
Temperature profiles	from radiosonde data	250 m vertical	radiosonde within 3 hours of cirrus.	277 profiles
Upper tropospheric RH_{ice}	calculated with Raman lidar vapor water mixing ratios, linearly interpolated radiosonde data, and Murphy and Koop (2005) es_{ice}	10 minute, 200-300 m vertical	low random error in water vapor mixing ratio (<20%), low random errors in DR (<20%), concurrent (±6 hours) radiosonde observations	145 12-hour periods (0-12 UTC only)
Cirrus optical depths (σ)	Beer's law and lidar backscatter used to estimate σ at 355 nm	1 minute	We required DR > 10%, σ error < 200%, and at least 70% data availability over the 3-hour period.	774 3-hour periods

Table 3.3. Definitions of estimated cirrus properties. See Table 3.2 for specifications of the cirrus datasets used to estimate cirrus properties.

Cirrus property	Definition	Cirrus datasets used
In-cloud temperature, T_c (°C)	T for depolarization ratio (DR) >10%, T_c derived from linearly interpolated radiosonde data.	Cirrus cloud masks, Temperature profiles
Duration, D (min)	Duration of continuous DR > 10% computed at each height.	Cirrus cloud masks
Effective lengthscale, L_{eff} (km)	D*horizontal wind speed linearly interpolated from radiosonde	Cirrus cloud masks
Layer thickness, Δz_{layer} (km)[1]	Thickness of continuous DR > 10% computed at each time.	Cirrus cloud masks
Total thickness , Δz_{total} (km)[1]	Thickness of all DR > 10% computed at each time.	Cirrus cloud masks
In-cloud Φ (K/km)	Φ (Eq 3.2) averaged from cloud bottom to cloud top	Cirrus cloud masks, Temperature profiles
Above-cloud Φ (K/km)	Φ (Eq 3.2) from cloud top to 500 m above cloud top	Cirrus cloud masks, Temperature profiles
In-cloud RH_{ice}	DR>10% (43,164 total observations)	Cirrus cloud masks, Upper tropospheric RH_{ice}
Near-cloud RH_{ice}	DR<10% and were within 30 minutes and 500 m of cirrus (77,552 total observations)	Cirrus cloud masks, Upper tropospheric RH_{ice}
Below-cloud RH_{ice}	DR<10% and were up to 1000 m below cirrus (44,627 total observations)	Cirrus cloud masks, Upper tropospheric RH_{ice}
Distant-from-cloud RH_{ice}	DR<10% and were far from cirrus (>6 hours) and had heights > 8.3 km. (105,172 total observations)	Cirrus cloud masks, Upper tropospheric RH_{ice}
Cirrus optical depth, (σ)	The e-folding reduction factor for solar radiation	Cirrus optical depths
Optical depth distribution, P(σ)	Probability density function of σ over a three-hour period	Cirrus optical depths
Mean σ, $\overline{\sigma}$	Mean σ over three-hour period	Cirrus optical depths
Standard deviation in σ, std(σ)	Standard deviation in σ over a three-hour period	Cirrus optical depths
$P(\sigma)_{\Gamma}$	Gamma distribution fit to observed P(σ) using observed $\overline{\sigma}$ and std(σ)	Cirrus optical depths
$P(\sigma)_{\Gamma pred}$	Gamma distribution fit to observed P(σ) using observed $\overline{\sigma}$ and Eq. 3.9a	Cirrus optical depths
Cloud fraction, cf	Fraction of 3-hour period with cirrus (DR>10%)	Cirrus cloud masks

3.2.2. Cirrus σ and OLR calculations

We estimated cirrus P(σ) and cloud fraction (cf) over three-hour periods using the Raman lidar-derived σ time series (Table 3.2, Table 3.3):

$$P(\sigma)_{\sigma_i} \equiv \frac{N_c(\sigma_i - \Delta\sigma < \sigma < \sigma_i + \Delta\sigma)}{N_c} \tag{3.3}$$

where N_c is the number of cirrus σ observations (cirrus ≡ σ > 0.01 and DR > 10%), Δσ=0.05, and σ_i=0.06:0.1:3.501 is the discretization over the observed range of σ.

$$cf \equiv \frac{N_c}{N_o} \tag{3.4}$$

where N_o=(1/minute)*3 hours=180 is the number of lidar σ observations in three hours.

P(σ) retrievals were calculated over 3-hours because in this time, the mean horizontal wind advects ~250 km of air, a typical GCM spatial resolution, over the lidar field of view. We calculated P(σ) with 1-minute temporal resolution data to capture σ variability important for radiative transfer calculations (Carlin et al., 2000). We used liberal data quality thresholds to obtain continuous σ time series. When lidar attenuation occurred, we set σ to the attenuation limit σ, or the largest σ the lidar can observe (nominally σ~3). Use of the attenuation limit σ may underestimate cirrus σ and generate artificial P(σ) shapes. However, we would rather include the minimum inferred σ than exclude large σ recorded by lidar attenuation..

We calculated OLR using Eq. 1 from Fu et al. (2000), which neglects atmospheric effects:

$$OLR = \sigma_{sb}\left(T_s^{\,4} - T_c^{\,4}\right)\exp^{-\frac{D\sigma}{c}} + \sigma_{sb}T_c^{\,4} \tag{3.5}$$

In all OLR calculations, we used the independent column approximation which neglects three-directional radiative transfer effects, and estimated T_s and T_c with linearly-interpolated radiosonde and surface observations.

We calculated the average OLR over three-hours using the observed σ variability (OLR_{var} Wm^{-2}):

$$OLR_{\text{var}} \equiv \frac{\sum_{t=0}^{t_{end}} OLR\left(\overline{T_s}, \overline{T_c}, \sigma(t)\right)}{N_o} \tag{3.6}$$

where t_{end}=3 hours, $\overline{T_s}$ is the mean T_s during the three-hour period and $\overline{T_c}$ is the mean T_c during the three-hour period.

To estimate biases generated by neglecting cirrus inhomogeneity, we compared OLR_{var} to OLR calculations that incorporated three different approximations of the observed cirrus σ variability: 1) OLR_{PPH} (Wm^{-2}) was calculated using:

$$OLR_{PPH} \equiv OLR\left(\overline{T_s}, \overline{T_c}, \overline{\sigma}\right) \tag{3.7}$$

where $\overline{\sigma}$ was calculated from the observed 3-hour σ time series.

2) OLR_{Γ} (Wm^{-2}) was calculated using:

$$OLR_{\Gamma} \equiv \sum_{\sigma=0}^{7} P_{\Gamma}(\sigma) OLR\left(\overline{T_s}, \overline{T_c}, \sigma\right) \tag{3.8}$$

where $P(\sigma)_{\Gamma}$ is Eq. 2.1 with $\overline{\sigma}$ and υ calculated from the observed 3-hour σ time series.

3) $OLR_{\Gamma pred}$ (Wm^{-2}) was calculated using:.

$$OLR_{\Gamma\, pred} \equiv \sum_{\sigma=0}^{7} P_{\Gamma\, pred}(\sigma) OLR\left(\overline{T_s}, \overline{T_c}, \sigma\right) \tag{3.9a}$$

where $P(\sigma)_{\Gamma pred}$ is Eq. 2.1 with $\overline{\sigma}$ calculated from the observed 3-hour σ time series and the std(σ) is predicted by the observed relationship between all observed $\overline{\sigma}$ and std(σ):

$$std(\sigma) = 0.3014 Ln\left(\overline{\sigma}\right) + 0.6727 \tag{3.9b}$$

3.3. Analysis of new cirrus observations

3.3.1. Temperature and humidity

P(Ci) maximized at -50 °C: 76% of T_c were between -35 and -60 °C (Figure 3.1). Comparison of P(Ci,T) and P(T) indicated that the availability of cold upper tropospheric air was not a strong control on minimum T_c. Like Mace et al. (2001) (hereafter MCA), we found that cirrus were higher in the summer than in the winter, but that there was no statistically significant seasonal change in T_c (Table 3.4).

Most lidar-derived in-cloud humidities were sub-saturated with respect to ice: 65% had RH_{ice} < 90% (Figure 3.2). Only 26% of our retrieved in-cloud RH_{ice} observations were supersaturated with respect to ice, 98% of our retrieved in-cloud RH_{ice} observations were below RH_{ice}=130%, and only 0.7% met the Koop et al. (2000) criterion for homogeneous freezing. Our lidar-derived in-cloud RH_{ice} were similar to CAT, who found 31% of in-cloud points were saturated with respect to ice (Table 3.1) . In-cloud humidity estimates were insensitive (± 3%) to depolarization ratio thresholds between 10 and 20% and to the es_{ice} formulation (Goff and Gratch (1946) vs. Murphy and Koop (2005)).

The lidar observations indicated that ice-free air in the upper troposphere was very dry, but that near-cloud RH_{ice} observations varied from very dry to supersaturated with respect to ice (Figure 3.2b).

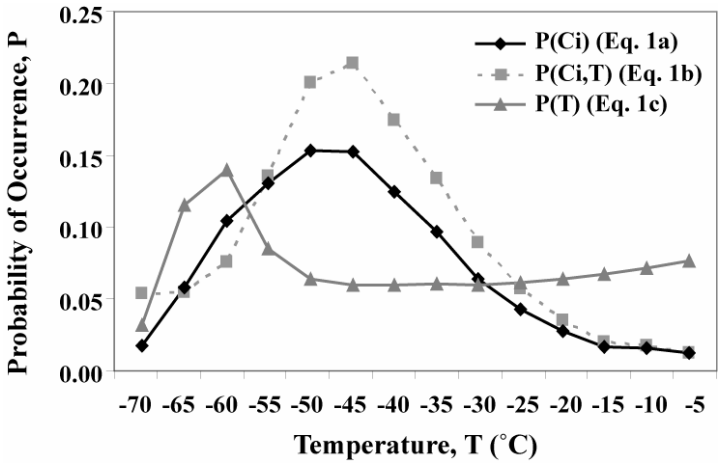

Figure 3.1: Cirrus and upper tropospheric temperatures. P(Ci) maximized at -45 °C.

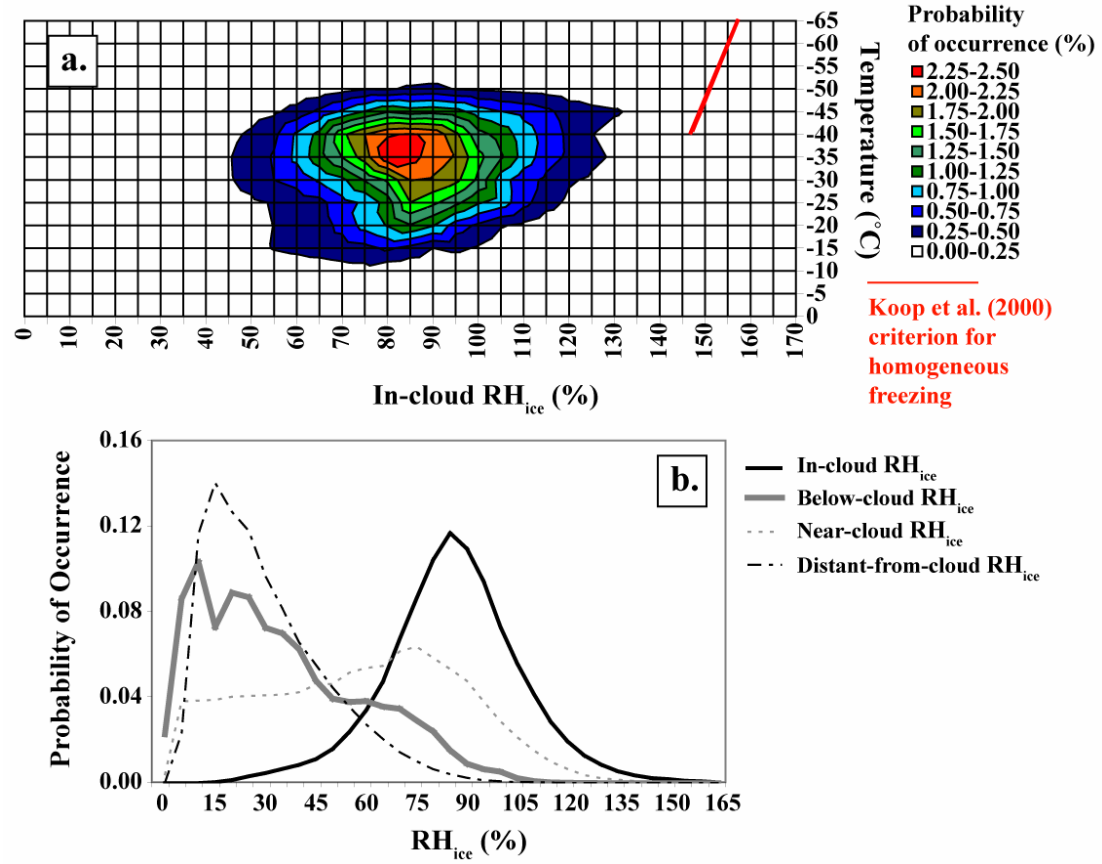

Figure 3.2: Lidar-derived humidity in and around cirrus. a) In cloud RH_{ice} as a function of T_c. In-cloud RH_{ice} increased as T_c decreased, but the majority of RH_{ice} were below ice saturation. b) RH_{ice} distributions. The air not directly associated with cirrus and below cirrus was very dry. See Table 3.3 for definitions.

Our lidar-derived RH_{ice} measurements are inconsistent with large S_i found in and around cirrus during many field campaigns (e.g., Ovarlez et al. (2002), Jensen et al. (2001)). Indeed, if our low in-cloud RH_{ice} were representative, we would be forced to conclude that rapid sublimation is occurring in most Lamont, OK cirrus. The biased sampling of our RH_{ice} observations (Figure 3.3) and the lidar resolution (Table 3.2) can explain why our observed RH_{ice} were often sub-saturated with respect to ice. T_c associated with RH_{ice} observations were 10-15 °C higher than T_c associated with high depolarization observations. Given the 200-300 m vertical resolution of the lidar, mixing of cloudy and clear air could also have biased in-cloud RH_{ice} observations (Table 3.2). For example, mixing 70% in-cloud air (RH_{ice} =100%) with 30% near-cloud air (RH_{ice} =50%) results in an RH_{ice} of 85%.

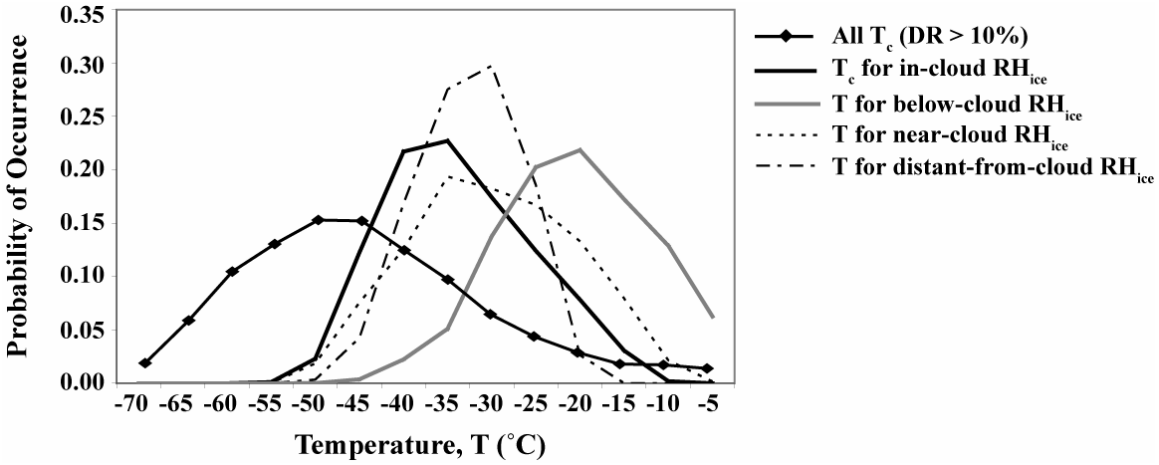

Figure 3.3: Temperature sampling of lidar observations. Temperatures associated with lidar-derived RH_{ice} observations were 10-15 °C higher than observed T_c. This temperature bias resulted because errors in the lidar-derived water vapor mixing ratios increased with height. As a result, lidar-derived RH_{ice} observations (Figure 3.2) were representative of cloud bottoms and cirrus with high T_c. See Table 3.3 for definitions of DR, T_c, in-cloud RH_{ice}, below-cloud RH_{ice}, near-cloud RH_{ice} and distant-from-cloud RH_{ice}.

Table 3.4: Cirrus properties from Lamont, OK. All values are reported as mean ± standard deviation.

	All	Day (12-24 UTC)	Night (0-12 UTC)	Winter (DJF)	Spring (MAM)	Summer (JJA)	Fall (SON)
# 12-hour periods	328	152	176	51	121	66	90
Height (km)	9.7 ± 1.7	9.8 ± 1.7	9.7 ± 1.6	9.1 ± 1.4	9.2 ± 1.6	11.3 ± 1.3	9.7 ± 1.5
T_c[1] (°C)	-43 ± 8	-43 ± 8	-43 ± 8	-43 ± 8	-42 ± 9	-47 ± 8	-42 ± 7
Duration - D (min)	37 ± 16	38 ± 16	37 ± 17	40 ± 16	38 ± 16	42 ± 19	32 ± 14
Length scale - L_{eff} (km)	64 ± 61	66 ± 62	63 ± 59	99 ± 94	67 ± 41	36 ± 21	63 ± 68
Advection speed (m/s)	25 ± 12	24 ± 12	26 ± 13	33 ± 10	27 ± 11	13 ± 5	27 ± 12
Layer thickness - Δz_{layer} (km)	1.1 ± 1.0	1.1 ± 1.0	1.1 ± 1.0	1.1 ± 0.5	1.0 ± 0.5	1.0 ± 0.5	0.9 ± 0.4
Total thickness - Δz_{total} (km)[2]	1.7 ± 1.2	1.8 ± 1.1	1.7 ± 1.2	1.6 ± 0.8	1.6 ± 0.8	1.3 ± 0.7	1.3 ± 0.7

[1.] Mean T_c were similar to those found by WS (~-45 °C) and MBV (-43 ± 10 °C).

[2.] Mean observed Δz_{total} were ~ 0.3 km thinner than MCA and ~0.6 thinner than MBV. Thinner clouds in our lidar retrievals could result from lidar attenuation or increased sampling of optically thin clouds.

3.3.2. Cirrus macrophysical properties

Distributions of macroscale cirrus cloud properties were broad, but Δz_{layer} and D distributions were dominated by small values (Figure 3.4, Table 3.4). The majority (64%) of cirrus consisted of single layer clouds, but the presence of multi-layer clouds made distributions Δz_{total} flatter than distributions of Δz_{layer}.

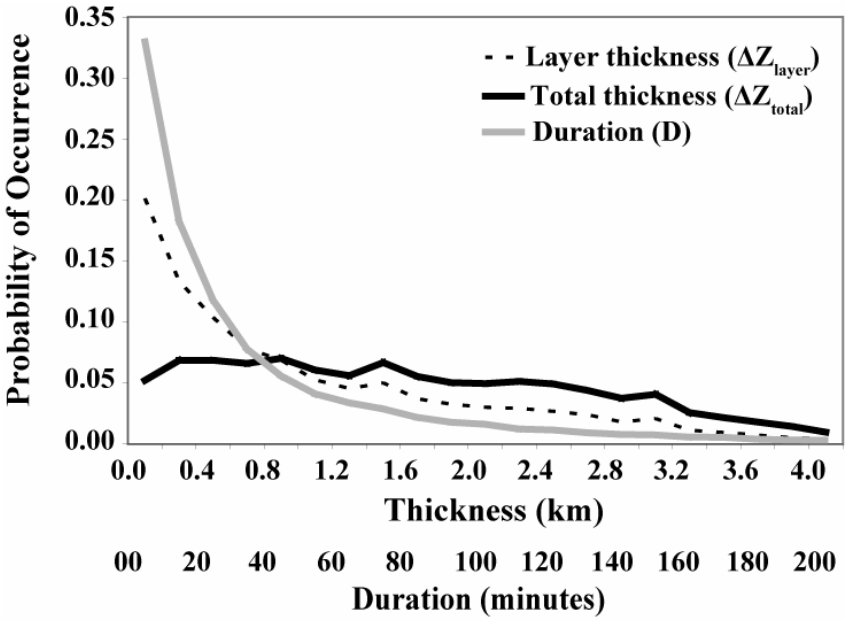

Figure 3.4: Lidar-derived cirrus macrophysical properties. Δz_{layer} and D distributions were dominated by small values. See Table 3.2 for definitions of $\Delta z_{layer,}$ Δz_{total} and D.

Like Wang and Sassen (hereafter WS) and MCA (Table 3.1), we found that cirrus macrophysical cloud properties were largely independent of season. D, Δz_{layer} and Δz_{total} did not depend on season, but seasonal shifts in upper tropospheric wind speeds did result in seasonal variation in the measured L_{eff} (Table 3.4). The lack of correlation between mid-latitude cirrus macrophysical properties and season is intriguing because MCA found that cold season cirrus form in association with synoptic weather disturbances while warm season cirrus form by convective detrainment (Table 3.1). Therefore, cirrus macrophysical properties were largely independent of formation regime.

Mean cirrus Δz_{layer}, D, and L_{eff} depended on T_c (Figure 3.5). Although large sample sizes allowed precise estimation of, and discrimination between, mean macrophysical values, large observed standard deviations suggest it would be difficult to predict the macrophysical properties of cirrus using T_c alone (Table 3.4).

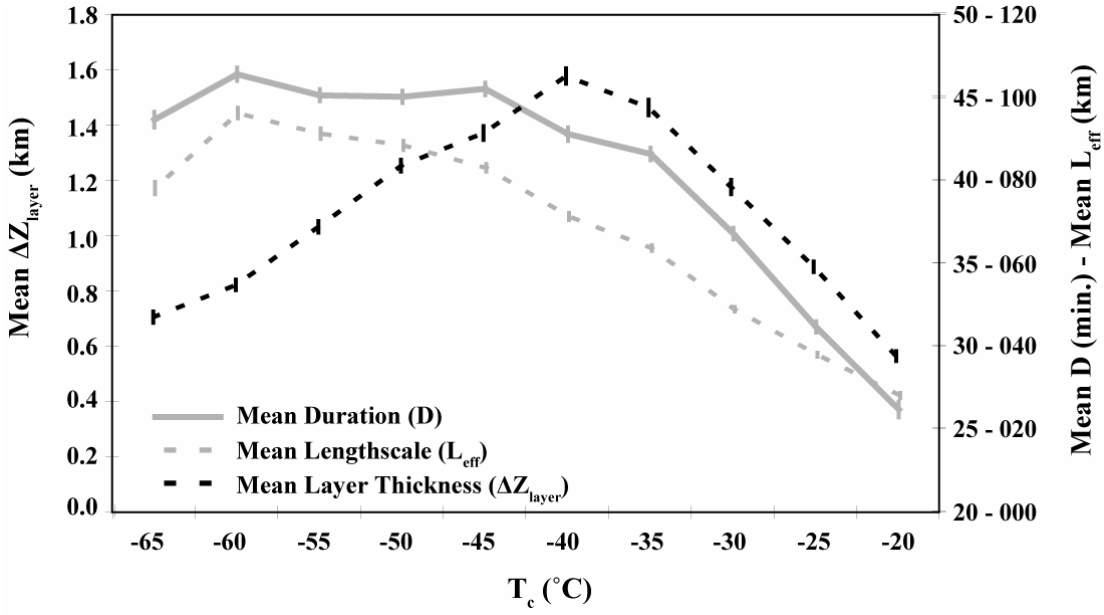

Figure 3.5: Mean cirrus macrophysical properties as functions of cirrus temperature. Error bars show the standard error of each measurement, not the standard deviation. Mean cirrus macrophysical properties depended on T_c, but large observed standard deviations (Table 3.3) suggest it would be difficult to predict cirrus macrophysical properties using T_c alone. See Table 3.2 for definitions of $\Delta z_{layer,}$ D and L_{eff}.

3.3.3. Cirrus static stability and relationship to cirrus macrophysical properties

In-cloud lapse rates were generally stable with respect to ice pseudoadiabatic processes (Φ = 1.7 ± 0.9 °C/km) , but some unstable layers were observed (Figure 3.6a, Figure 3.6b). Unstable layers indicate that there may have been turbulence and mixing within some cloud layers.

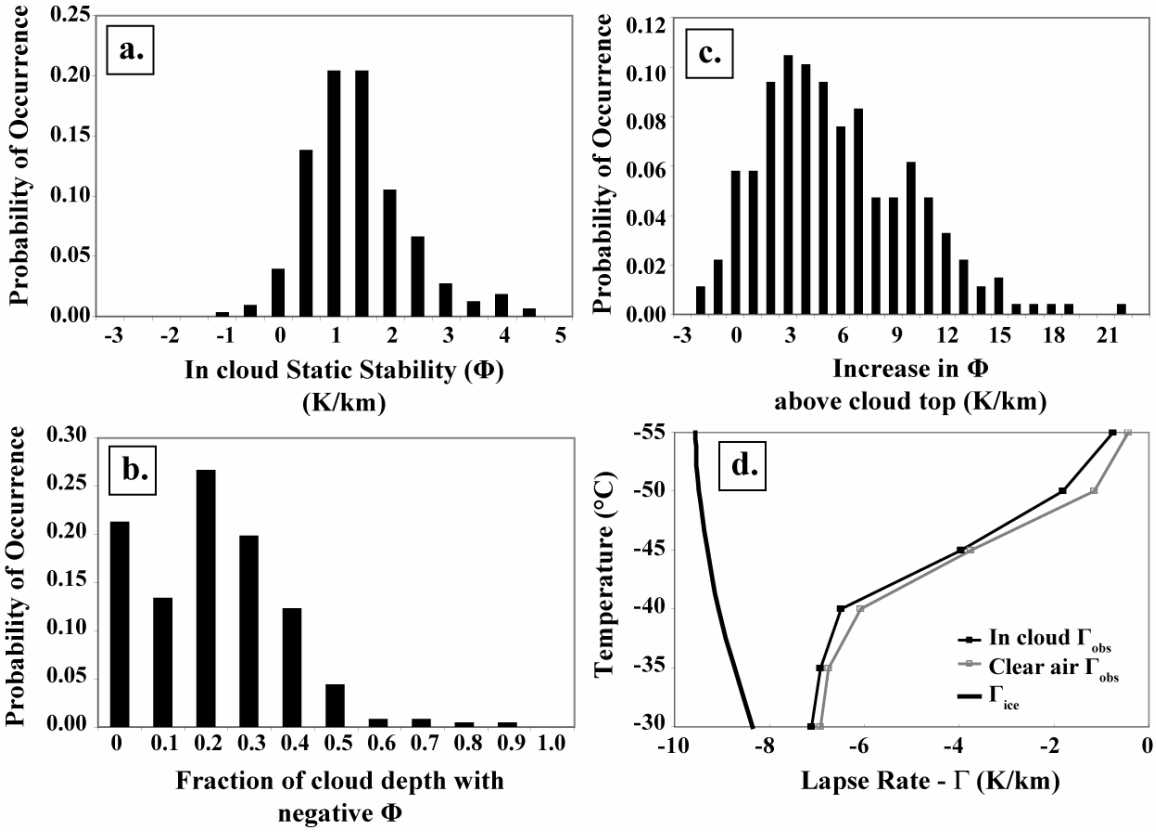

Figure 3.6: Static stability in and around cirrus. a) Cirrus Φ (Eq. 3.2). Observed in-cloud lapse rates were generally stable with respect to the ice pseudoadiabatic processes. b) Fraction of cloud with negative Φ. Individual clouds often had individual layers that were unstable with respect to the ice pseudoadiabatic processes. c) Increase in cirrus Φ above cloud top (K/km). The majority of cirrus were capped by a 500 m layer with greater Φ than the in-cloud Φ. d) Average upper tropospheric soundings with and without cirrus. The average upper troposphere Φ increased with temperature because Γ_{ice} decreased and Γ_{obs} increased.

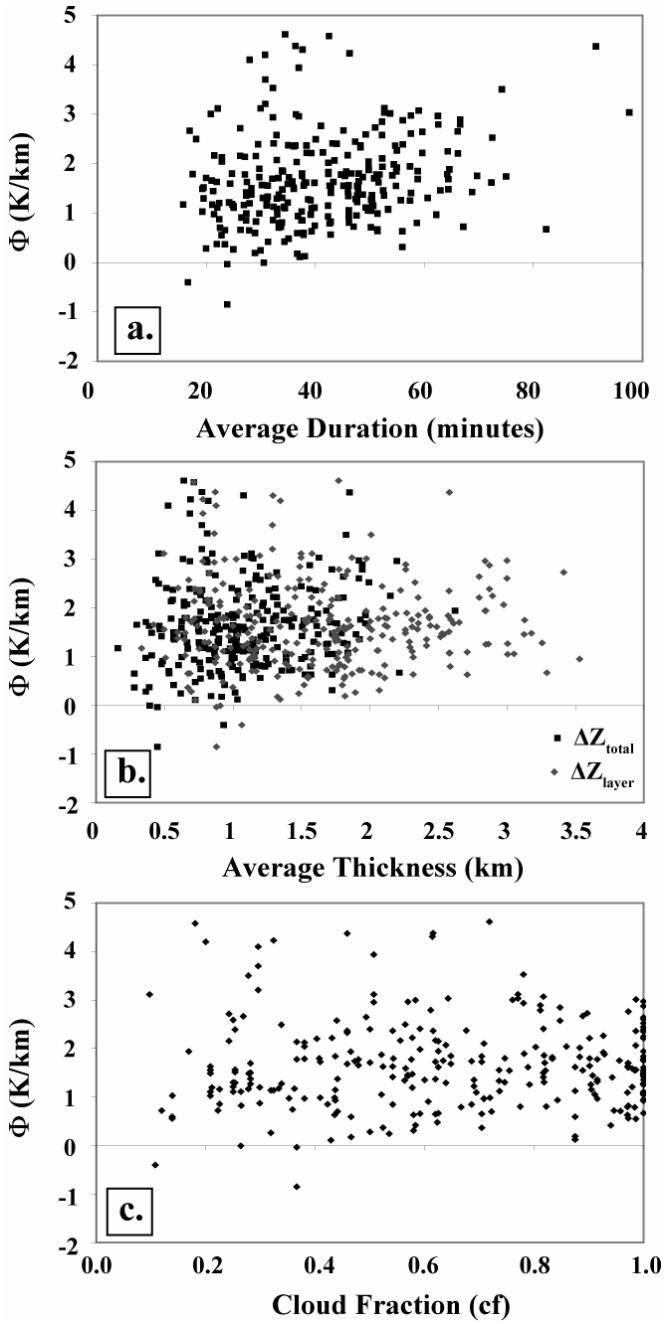

Figure 3.7: Relationship between cirrus static stability and macrophysical properties. Cirrus macrophysical properties were largely independent of in-cloud Φ. The weak positive relationship between duration and Φ could reflect the increase in both wind speed and Φ with height. See Table 3.2 for definitions of $\Delta z_{layer,}$ Δz_{total} and D.

Most cirrus were capped by air with large Φ (Figure 3.6c). In general, the average upper tropospheric Φ increased as T decreased (Figure 3.6d) because Γ_{ice} decreased and Γ_{obs} increased (Eq. 3.2). However, the increase in Φ above cirrus cloud tops was greater than the average decrease in upper tropospheric Φ with T. Therefore, minimum T_c may be partially controlled by increasing Φ above cirrus cloud tops.

Cirrus macrophysical properties were independent of in-cloud Φ for Φ > 0 (Figure 3.7). For the very small fraction of cirrus in unstable environments (Φ < 0), we observed smaller thicknesses and D. Increasing Φ and horizontal wind speed with height resulted in a weak correlation between Φ and D (Figure 3.6d, Figure 3.7a).

3.3.4. Cirrus σ and OLR calculations

Optically thin cirrus were common at Lamont, OK: 66% of observed cirrus σ were less than 0.5 (Figure 3.8a). The vast majority (>90%) of cirrus P(σ) had $\overline{\sigma} < 1$ and $1 < \nu < 3$ (Figure 3.8b). Most cirrus had monotonically decreasing P(σ). Cirrus cf occurred at all values between 0 and 1 (Figure 3.8c).

Neglecting σ variability resulted in an underestimation of OLR. OLR_{PPH} (Eq. 3.7) underestimated OLR by 4.9 ± 5.7 Wm^{-2} when compared to OLR_{var} (Eq. 3.6) (Table 3.5). As expected (Chapter 1.2), the OLR_{PPH} bias [$OLR_{var} - OLR_{PPH}$] increased with std(σ) (Figure 3.9) and the difference between T_s and T_c (not shown, see Eq. 1.5).

Table 3.5: Mean OLR biases and absolute deviations. All values are reported relative to OLR_{var} (Eq. 3.6).

	OLR_{PPH} (Eq. 3.7)	**OLR_{Γ} (Eq. 3.8)**	**$OLR_{\Gamma pred}$ (Eq. 3.9)**
Average Bias - Wm^{-2}	4.9 ± 5.7	-0.2 ± 0.8	-0.3 ± 3.3
Average Absolute Deviation - Wm^{-2}	4.9 ± 5.7	0.6 ± 0.6	2.1 ± 2.6

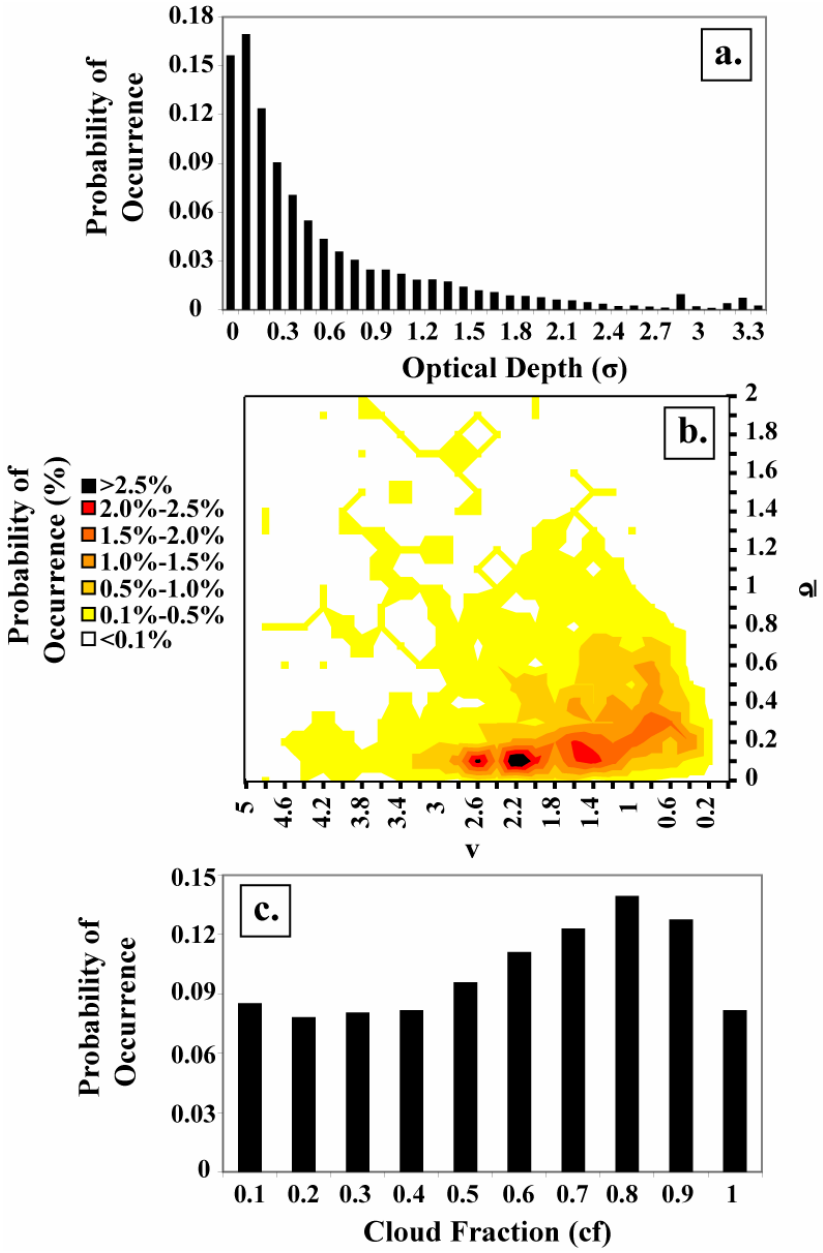

Figure 3.8: Lidar-derived cirrus σ, P(σ), and cloud fraction observations. a) Small values dominate the histogram of all σ observations. We found σ= 0.62 ± 0.68 over the entire Lamont, OK σ dataset, similar to σ statistics found by WS (σ= 0.58 ± 0.67). b) Fit parameters for $P(\sigma)_\Gamma$. Most cirrus $P(\sigma)_\Gamma$ were calculated with $\overline{\sigma} < 1$ and $1 < \nu < 3$. c) Cirrus cloud fraction (Eq. 3.4). Cirrus cf occurred at all values between 0 and 1. For definitions of $P(\sigma)_\Gamma$ and cf, see Table 3.3.

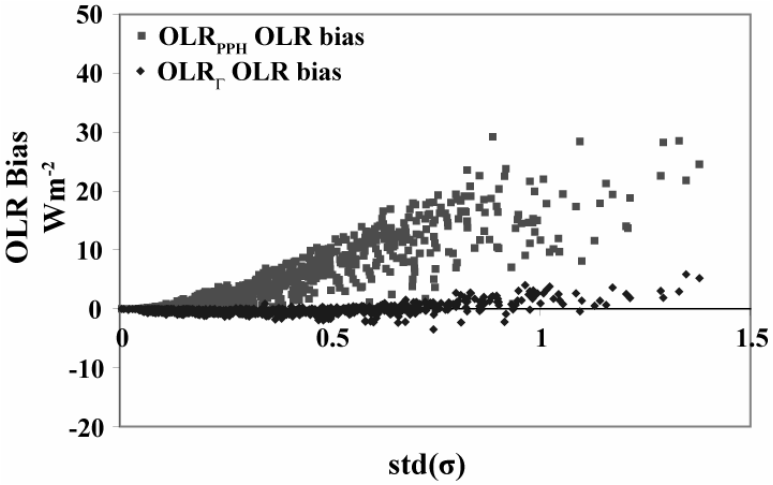

Figure 3.9: OLR biases vs. cirrus σ variability. OLR_{PPH} biases [OLR_{var} (Eq. 3.6) – OLR_{PPH} (Eq. 3.7)] increased with std(σ). Using Eq. 2.1 to represent cirrus P(σ) dramatically reduced OLR_{PPH} biases: 93% of OLR_{Γ} biases [OLR_{var} (Eq. 3.6) – OLR_{Γ} (Eq. 3.8)] < 1 Wm^{-2}.

Using OLR_{Γ} (Eq. 3.8) reduced the average OLR_{PPH} bias (Table 3.5, Figure 3.9). Reductions in OLR_{PPH} bias were largest for the P(σ) with large std(σ) and monotonically decreasing shapes (Figure 3.9, Figure 3.10). For example, using a gamma distribution to represent P(σ) reduced the OLR bias from 10.4 Wm^{-2} [OLR_{var} – OLR_{PPH}] to -0.5 Wm^{-2} [OLR_{var} – OLR_{Γ}] during a three-hour period on April 20, 2001 (Figure 3.10a, Table 3.6).

For many observed P(σ), using OLR_{Γ} (Eq. 3.8) did not affect computed OLR. Many observed cirrus P(σ) had small $\overline{\sigma}$, small std(σ), and monotonically decreasing P(σ) shapes (Figure 3.8). Although P(σ) dominated by small σ were well fit by gamma distributions, they did not generate large OLR_{PPH} biases. For example, on January 26, 1999, the gamma distribution approximation changed the OLR bias from 0.0 [OLR_{var} – OLR_{PPH}] to -0.1 Wm^{-2} [OLR_{var} – OLR_{Γ}] (Figure 3.10b, Table 3.6).

The largest residual OLR_{Γ} bias [OLR_{var} – OLR_{Γ}] resulted from a recently formed anvil cirrus with a bi-modal P(σ) (Figure 3.10c, Table 3.6). Although lidar attenuation made it difficult

to estimate the exact P(σ) shape at large σ, a single gamma distribution could not represent the observed bi-modal P(σ) shape and resulted in a residual OLR_{Γ} bias of 3.1 Wm^{-2}.

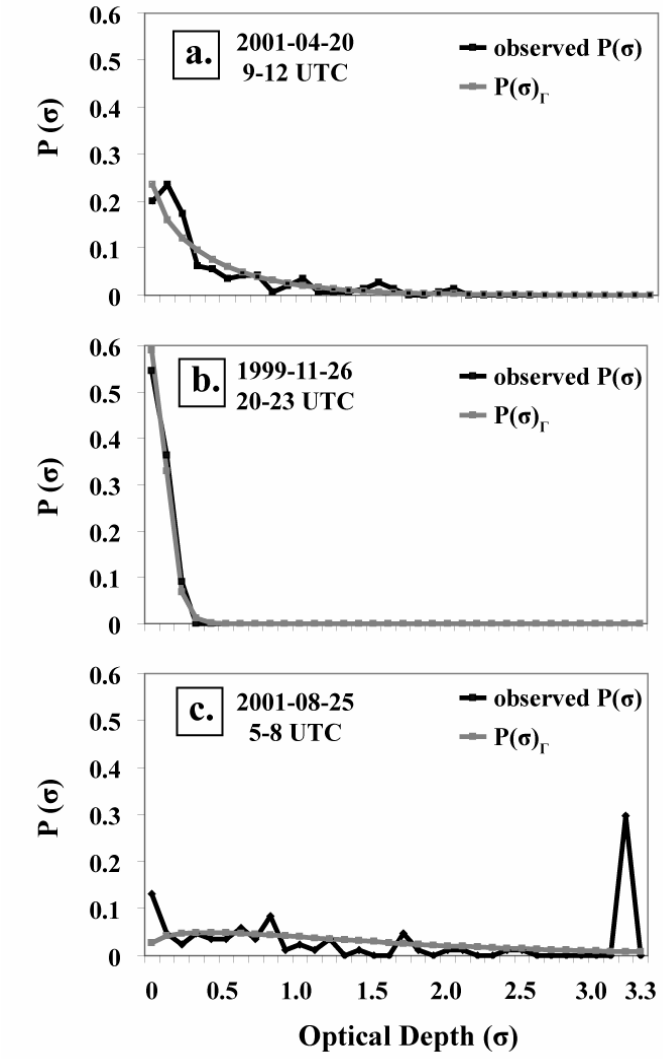

Figure 3.10: Observed P(σ) and gamma fit P(σ) for three case studies. Single gamma distributions successfully fit monotonically decreasing P(σ)**,** but not bi-modal P(σ). For computed OLR, see Table 3.6.

Table 3.6. σ variability and computed OLR for three case studies.

	2001-04-20 9-12 UTC	**1999-11-26 20-23 UTC**	**2001-08-25 5-8 UTC**
$\sigma \pm$ std(σ)	0.44 ± 0.47	0.10 ± 0.07	1.53 ± 1.29
T_s (°C)	18	18	28
T_c (°C)	-57	-49	-44
OLR_{var} (Wm^{-2}) Eq. 3.6	346.0	404.0	386.5
OLR_{PPH} (Wm^{-2}) Eq. 3.7	335.7	403.9	363.9
OLR_{Γ} (Wm^{-2}) Eq. 3.8	346.5	404.0	383.5
OLR_{var} - OLR_{PPH} (Wm^{-2})	10.4	0.0	22.6
OLR_{var} - OLR_{Γ} (Wm^{-2})	-0.5	-0.1	3.1

Average OLR_{PPH} biases were reduced by the use of $OLR_{\Gamma pred}$ (Eq. 3.9, Figure 3.11, and Table 3.5). $OLR_{\Gamma pred}$ had a larger average absolute deviation from OLR_{var} than OLR_{Γ} (Figure 3.11b, Table 3.5). Nevertheless, these results demonstrate that using the observed functional dependence of std(σ) on $\overline{\sigma}$ is an easy and useful strategy for reducing OLR biases associated with cirrus inhomogeneity.

Decreasing the temporal resolution of the σ data dramatically increased OLR biases. Averaging the σ data reduced the std(σ) and resulted in the mixing of cloudy and clear air (Figure 3.12a). As a result, the OLR_{PPH} bias [OLR_{var} (1 min.)- OLR_{PPH} (xxx min.)] increased from 4.9 ± 5.7 Wm^{-2} for 1-minute data to 15.3 ± 21.8 Wm^{-2} and 16.5 ± 21.9 Wm^{-2} for 10-minute and 1-hour data respectively (Figure 12b). Even the OLR_{Γ} biases [OLR_{var} (1 min.) - OLR_{Γ} (xx-min)] were large: 10.2 ± 18.0 Wm^{-2} and 12.4 ± 19.5 Wm^{-2} for 10-minute and 1-hour data respectively (Figure 12c). These results imply even with the gamma distribution approximation for cirrus P(σ), significant biases in the computed OLR can result if σ variability and the clear air between cirrus are unresolved.

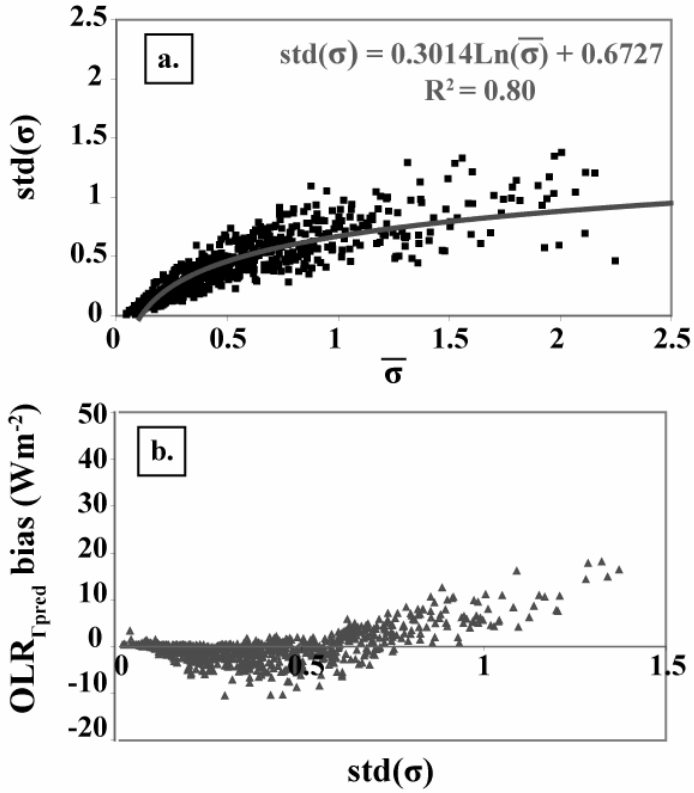

Figure 3.11. Reducing OLR bias by using the observed mean σ to predict σ variability a. Scatter plot and log fit between mean σ and std(σ) over three-hour periods. b. $OLR_{\Gamma pred}$ bias [$OLR_{var} - OLR_{\Gamma pred}$] was smaller than the OLR_{PPH} bias [$OLR_{var} - OLR_{PPH}$] (see Table 3.5). Using the observed $\overline{\sigma}$ *to estimate std(σ) reduced OLR biases.*

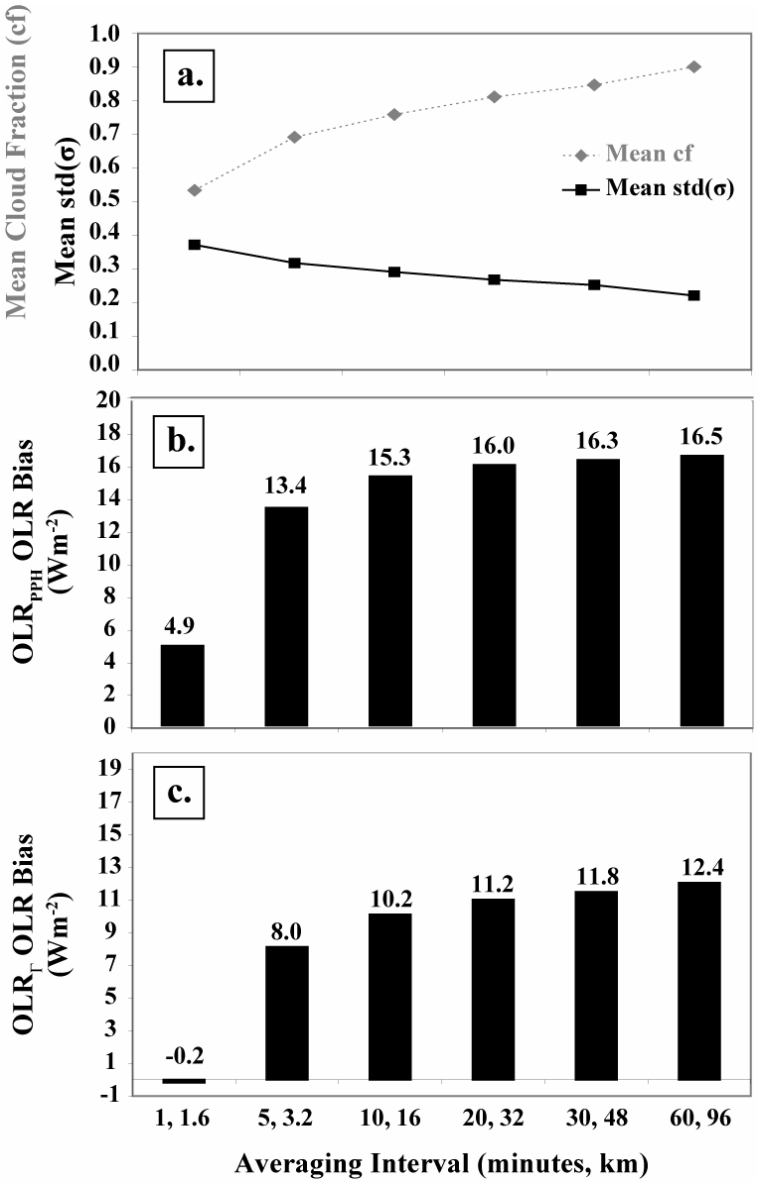

Figure 3.12: Influence of data resolution on cirrus inhomogeneity and computed OLR.
a. cf (Eq. 3.4) and std(σ). Decreasing the temporal resolution of the lidar observations resulted in the mixing of clear and cloudy air. b. OLR_{PPH} bias [OLR_{var} (1 min.) – OLR_{PPH} (xxx min.)]. c. OLR_{Γ} bias [OLR_{var} (1 min.) – OLR_{Γ} (xxx min.)]. The temporal resolution of the σ data had a large influence on the cf, cirrus std(σ), the OLR_{PPH} bias and OLR_{Γ} biases. All OLR biases increased as the apparent lidar resolution decreased.

3.4. Discussion of the physical controls on observed cirrus P(σ)

Our cirrus observations together with MCA, MBV, WS, and CAT (Table 3.1) provide one of the most detailed climatologies of cirrus properties and cirrus environments available to date. Here, we combine these observations with parcel model calculations and offer our insights into the processes that control Lamont, OK cirrus σ variability.

3.4.1 Physical picture for cloud formation and evolution

We have a simple physical picture for cirrus formation and evolution: First, lifting generates a saturated layer in the upper troposphere (T < -40 °C). When portions of this saturated layer reach the homogeneous nucleation freezing threshold (Koop et al., 2000), ice crystals form via the freezing of aerosols. In nucleating regions of the saturated layer, N_{ice} is primarily controlled by w^h because $J_{hom\text{-}max}$ increases with w^h. Externally forced mesoscale motions (spatial scale 100-1000s m) generate variability in w^h and therefore in N_{ice}. After formation, ice crystals grow and fall through the saturated layer. The T and depth of the saturated layer and N_{ice} control R_{eff} and ice crystal fall speeds. The residence time of ice crystals in the saturated layer affects the σ time evolution and the cloud lifetime. Once ice crystals fall out of the saturated layer, they sublimate in the dry air below the saturated layer. When present, large ice crystals have large survival distances below the saturated layer and can increase Δz.

In our physical picture, cirrus σ variability (Figure 3.8) is controlled by variability in w^h and by variability in the saturated layer depth and T. At a fixed saturated layer T and depth, w^h determines both N_{ice} and R_{eff}. Therefore, the saturated layer depth, saturated layer T, and w^h set the residence time of ice crystals in the saturated layer and the distance that ice crystals will fall below the saturated layer. Observations from Lamont, OK suggest that most ice crystals are small (MCA). Therefore, residence times of ice crystals below the saturated layer (τ_{sub}) are uniformly short and do not affect σ variability.

3.4.2 Justification for proposed controls on cirrus P(σ)

In the following discussion, we justify the conclusions required for the physical picture described above: 1) Homogeneous nucleation alone can explain formation of the observed cirrus. 2) Externally forced mesoscale motions are required to explain the observed N_{ice}. 3) Short cirrus

τ_{sub} (< 20 minutes) are common for Lamont, OK ice crystals. 4) Variability in mesoscale w^h and variability in saturated layer depth and T control cirrus σ inhomogeneity.

3.4.2.1. Homogeneous nucleation alone

Based on cirrus observations, simple modeling, and Occam's Razor (the simplest explanation is the most likely), we suggest homogeneous nucleation alone could explain the majority of the observed Lamont, OK cirrus formation. This assertion is supported by the following results:

a.) Observed cirrus temperatures (Figure 3.1): 75% of the observed cirrus had T_c < -40 °C. If cirrus formed close to their observation T_c, homogeneous nucleation alone could explain most observed cirrus formation. In addition, ice crystals sediment after they form, so the observed T_c could be higher than cirrus formation temperatures. Reduced homogeneous nucleation rates could have limited cirrus presence at T > -40 °C.

b.) Temperature dependent macrophysical and microphysical cloud properties: At T< -40 °C, increasing N_{ice} (MCA Table 3, MCA Figure 8), decreasing R_{eff} (MCA Table 3, WS Figure 5) and thinning clouds (Figure 3.5) are consistent with the fact that J_{hom} increases as T decreases. We feel less confident about attributing changes in R_{eff} and Δz to temperature-dependent J_{hom} for two reasons: 1) For a fixed N_{ice}, R_{eff} are smaller in colder air. 2) The saturated layer depth could change with T.

c.) Comparison of observed N_{IN} and N_{ice}: Typical upper tropospheric immersion N_{IN} (N_{IN}<0.03 cm^{-3} ((DeMott et al., 2003a), (Rogers et al.,1998))) rarely approach the average N_{ice} of 0.1 cm^{-3} reported by MCA. In the absence of ice multiplication processes and heterogeneous nucleation mechanisms of unknown atmospheric relevance (e.g., Gavish et al. (1990) Zuberi et al., (2001), Durrant and Shaw (2005)), homogeneous nucleation is required to explain the average N_{ice} and the width of the observed N_{ice} distribution. In addition, MCA may have actually underestimated N_{ice} because: 1) cloud radars have trouble detecting small ice crystals. For example, using Beesley et al. (2000) and assuming N_{ice}=0.1 cm^{-3}, the mmcr would not detect ice crystals with R_{ice} < 18 μm. Comparisons with aircraft observations suggest the Mace et al. (1998a) mmcr retrieval

for thin cirrus underestimates the N_{ice} of small R_{ice} (Mace et al., 1998b). 2) If fallout and subsequent sublimation of ice crystals has already occurred, observed N_{ice} could be lower than the original N_{ice}.

d.) Parcel model lifting experiments: Parcel model calculations suggest that plausible lifting of saturated upper tropospheric air leads to new homogeneous nucleation events. For example, if an air parcel with T= -50 °C and RH_{ice} =100% is lifted, only 360 m of vertical displacement (~3.5 °C cooling) is required to initiate homogeneous nucleation. Under typical conditions, pre-existing cirrus act to reduce the RH_{ice} generated by lifting, but homogeneous nucleation still occurred in parcels that were lifted 540 m (Table 3.7 –Research Question 1).

Table 3.7. Research questions addressed with K06 parcel model. "Typical cirrus" had N_{ice}=0.1 cm^{-3} , the average value reported by MCA (Table 3.1), and R_{eff}=36 μm. We determined R_{eff} using the N_{ice} and the supersaturated vapor mixing ratio at -50 °C. For more information about the parcel model, see Chapter 2 and K06 (Appendix A).

Research Question	***Initial Conditions***	***H (m)***	***w (cm sec^{-1})***	***Result***
1. How much lifting is required to initiate homogeneous nucleation?	T = -50 °C; RH_{ice}=100%; no cirrus or typical cirrus	100	2 or 100	With clear air, 360 m of lifting is required to initiate homogeneous nucleation. With pre-existing cirrus, the required lifting was: 380 m for w = 2 cm sec^{-1} 540 m for w = 100 cm sec^{-1}. At large w (100 cm/sec), new nucleation events were affected by the pre-existing cirrus because lifting was faster than fallout.
2. What w^h is required to form the average observed N_{ice} ?	T = -40, -50 or -60 °C ; RH_{ice}=100% no cirrus	100	7 to 11	The w^h required to generate N_{ice}=0.1 cm^{-3} were: 11 cm sec^{-1} for T = -40 °C, 9 cm $sec^{-1}$for T = -50 °C, 7 cm sec^{-1} for T = -60 °C.
3. What are cirrus sublimation timescales for MCA/MBV synoptic descent (Table 3.1)?	T = -50 °C ; RH_{ice}=100% ; typical cirrus	No fallout	-2 or -10	Complete sublimation took: 5.8 hours for w = -2 cm sec^{-1}, 2.5 hours with w = -5 cm sec^{-1}.

3.4.2.2. What generates lifting?

Mesoscale motions are required to generate the observed average N_{ice}. Synoptic w coincident with Lamont, OK cirrus observations were generally near 0 cm sec^{-1} and if ascending, rarely exceeded cm sec^{-1} (MCA Figure 5, MBV Figure 6). Assuming homogeneous nucleation, 7

$< w^h < 11$ cm sec^{-1} (cooling rates between 2.5 and 3.9 K/hour) were required to generate the MCA average N_{ice} of 0.1 cm^{-3} (Table 3.7 –Research Question 2). Therefore, observed synoptic w were too small to explain the average observed N_{ice} and the width of the N_{ice} distribution. Nevertheless, the observed N_{ice} (MCA Figure 7) were dominated by small values suggesting Lamont, OK cirrus formation did occur at $w^h < 11$ cm sec^{-1}.

Radiative and latent heating are unlikely to generate the positive buoyancy required for new homogeneous nucleation events. Therefore, lifting for new nucleation events was independent of cloud-induced instabilities. Observed in-cloud lapse rates were stable with respect to ice pseudoadiabatic processes (Figure 3.6a). Using the mean observed in-cloud Φ of 1.7 K/km and T=-50 °C, an instantaneous heating of 0.6 K is required to generate the buoyancy to lift a parcel 360 m from ice saturation to the Koop et al. (2000) homogeneous nucleation criterion. In cirrus, modeled radiative heating rates are measured in degrees/day and rarely exceed 2.3 10^{-4} K/sec (Gu and Liou, 2000). Therefore, radiative heating is unlikely to generate the buoyancy required for new nucleation events. Achieving an instantaneous heating of 0.6 K with latent heating requires the instantaneous freezing an IWC of 86 mgm^{-3}. Typical Lamont, OK IWC were < 60 mgm^{-3} (MCA Figure 8, MBV Figure 11). Therefore, latent heating is also unlikely to generate lifting for new nucleation events.

3.4.2.3. Short sublimation timescales

Previous studies have shown that τ_{sub} can be long and that ice crystals can survive long distances below cloud base ((Hall and Pruppacher (1976), O.'C Starr and Cox (1985), Heymsfield and Donner (1990)). For example, Hall and Pruppacher (1976) calculated that with R_{ice}>100 μm and sub-cloud RH_{ice} > 76%, ice crystals could fall 2 km before sublimating. O.'C Starr and Cox (1985) estimated τ_{sub} were ~1 hour with R_{ice}= 100-200 μm. These calculations are consistent with our τ_{sub} calculations for large R_{ice} (e.g., R_{ice} = 100 μm in Figure 3.13). However, Lamont, OK average R_{eff} were generally small (~ 35 μm MCA Table 2, ~50 μm WS Figure 5), so τ_{sub} primarily depended on the humidity profile. Even we had limited confidence in our lidar-retrieved RH measurements (see discussion in 3.2.1 and 3.3.1), they do suggest that below-cloud humidities were very low (Figure 3.2b). Therefore, we estimate that τ_{sub} were uniformly short (< 20 min.).

3.4.2.4. Controls on observed cirrus cloud inhomogeneity

Cirrus σ variability did not depend on N_{IN}, synoptic scale lifting and subsidence, and τ_{sub} variability. Observed N_{IN} are too small to explain observed the average or the range of cirrus N_{ice} (see section 3.4.2.1). Synoptic scale w cannot explain the observed range of σ (see section 3.4.2.2). With large scale subsidence (w <-2 cm sec^{-1}), typical Lamont, OK cirrus takes almost 6 hours to completely sublimate (Table 3.7 –Research Question 3). Although reduced IWC were associated with descending synoptic w (MBV Figure 11), the sublimation timescales for large scale subsidence are too long to explain the observed variability in σ (Figure 3.8). Finally, uniformly short τ_{sub} (< 20 minutes) (see section 3.4.2.3) cannot explain the observed σ inhomogeneity.

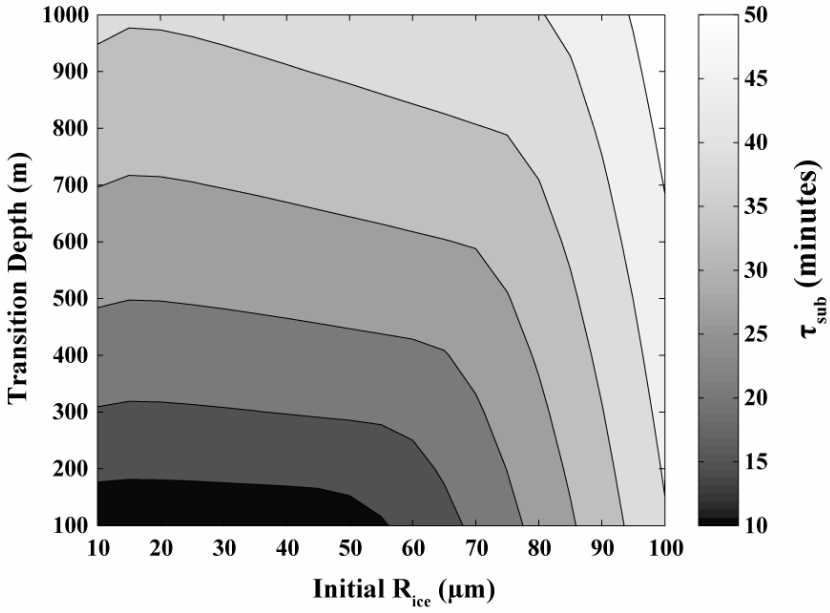

Figure 3.13: Sublimation timescales for individual ice crystals. The transition depth is the depth over which the RH_{ice} decreases linearly from ice saturation to RH_{ice} = 20%. For small ice crystals (R_{ice} < ~60 μm), τ_{sub} depended on the humidity profile, but was largely independent of ice crystal size. For large ice crystals (R_{ice} > ~60 μm), τ_{sub} depended on R_{ice}, but was largely independent of the sub-cloud humidity profile. Most Lamont, OK cirrus had small R_{eff}, and therefore probably had uniformly short τ_{sub}.

We conclude that variability in mesoscale w^h, and variability in saturated layer depth and T control the observed range of cirrus σ. Although a broad range of cirrus properties were observed, Lamont, OK σ were dominated by the smallest values. Most observed σ were small because small N_{ice} (MCA Figure 7), thin saturated layers, and short τ_{sub} were dominant (Figure 3.8a, Figure 3.8b). The observed dominance of small N_{ice} and monotonically decreasing P(σ) shapes is consistent with cirrus forming in a fallout-dominated regime (see Chapter 2 and K06).

3.4.3. Additional observations

We have presented explanations for observed cirrus inhomogeneity based on existing observations and simple modeling calculations. Here, we discuss new RH_{ice}, w, IN, and Φ observations that could be used to confirm or refute our picture of the main controls on cirrus inhomogeneity.

3.4.3.1. Humidity observations

Using Raman lidar observations, this study and CAT observed that RH_{ice} increased as T decreased, but found few portions of the cloud had high RH_{ice} (Figure 3.2, CAT Figure 1). Based on lidar-derived RH_{ice} observations, CAT concluded that "large ice supersaturation is common in cirrus clouds, which supports the theory of ice forming homogeneously." In our opinion, improved data quality and resolution are required both to assess the prevalence of ice supersaturation and to identify active homogeneous nucleation. We recommend new RH_{ice} observations that span the entire observed T_c range with high spatial resolution (± 50 m) and accuracy (± 5%).

In both this study and CAT, most retrieved in-cloud RH_{ice} values were sub-saturated with respect to ice. Sub-saturated in-cloud RH_{ice} values are not physically plausible, because they would have resulted in rapid sublimation of the existing cirrus clouds. Indeed, based the observed dominance of cirrus with small σ which correspond with small R (Eq. 2.5), we would expect persistent large in-cloud RH_{ice} values (see Chapter 2 and K06 Figure 3). As we explained in 3.3.1, low lidar-derived RH_{ice} observations resulted from the challenges associated with retrieving RH_{ice} using the current generation of Raman lidar technology. If Raman lidar

observations are to be used to assess the prevalence of ice supersaturation in cirrus, improved data quality is required.

We disagree with CAT's conclusion that existing lidar-derived RH_{ice} suggest that cirrus form by homogeneous nucleation. Less than 1% of lidar-derived in-cloud humidities achieved the supersaturation required for homogeneous nucleation to occur, and most lidar-derived RH_{ice} were subsaturated with respect to ice. With sufficient accuracy, lidar-derived RH_{ice} observations could be used to address the extent to which homogeneous nucleation is occurring above Lamont, OK. If RH_{ice} values approach the Koop criterion for homogeneous nucleation, active homogeneous freezing would be identified.

3.4.3.2 Vertical velocity observations

Mesoscale fluctuations in w have been observed in cirrus environments (e.g., above Lamont, OK (DeMoz et al.,1998), during FIRE (O'C. Starr and Wylie, 1990)). In addition, Hoyle et al. (2005) and Kärcher and Strom (2003) both suggested that variable w^h induced by mesoscale motions could explain observed N_{ice} distributions. Additional measurements of w^h in cirrus ($\pm$ 1 cm sec^{-1} at spatial scales of 100s m) would increase confidence in the conclusions from this study, Hoyle et al. (2005), and Kärcher and Strom (2003).

3.4.3.3 Observations of heterogeneous nucleation in the atmosphere

Although homogeneous nucleation alone could explain the Lamont, OK cirrus observations, existing observations cannot be used to rule out the occurrence of heterogeneous nucleation. With reproducible and representative observations of the N_{aer} fraction with an insoluble substrate at cirrus altitudes, we could better discriminate the extent to which heterogeneous nucleation contributes to cirrus formation. For example, we do not know to what extent organics (e.g., Beaver et al. (2006), Zorbrist et al. (2006), Gavish et al., 1990), efflorescence (e.g., Zuberi et al., 2001) or contact nucleation (e.g., Durrant and Shaw (2005)) contribute to heterogeneous nucleation in the atmosphere. With current immersion IN observations (e.g., DeMott et al. (2003a), Rogers et al. (1998)), however, it would be difficult to discriminate between homogeneous and heterogeneous nucleation at w below 11 cm sec^{-1} (see K06 Figure 4). Therefore, even if heterogeneous nucleation was occurring, the optical properties

of Lamont, OK cirrus may not have been affected by an occasional heterogeneous nucleation event.

3.4.3.4 Precisely co-located static stability and cirrus observations

Radiosondes are advected with upper level winds. Therefore, the profiles utilized in our analysis were not exactly co-located with lidar-observed cirrus. Given the intermittent nature of instabilities in the upper troposphere, checking the results of this study with co-located Φ and cloud observations would be useful.

3.5. Summary

Using a cirrus climatology from Lamont, OK and simple models, we found:

- Using 766 P(σ) calculated over 3-hour periods, we found that neglecting observed cirrus inhomogeneity resulted in an average OLR underestimation of 4.9 ± 5.7 Wm^{-2}. Most observed P(σ) shapes were well fit by gamma distributions with $\overline{\sigma}$ and ν derived from observations. As a result, using gamma distributions to represent observed cirrus P(σ) reduced our average calculated OLR bias to -0.2 ± 0.8 Wm^{-2}. However, even with the use of a gamma distribution, a large OLR bias of 3.1 Wm^{-2} resulted from an anvil cirrus P(σ) with a bi-modal P(σ) shape. Although bi-modal P(σ) shapes were not common in our observations, the identified anvil cirrus P(σ) misfit is concerning given the radiative importance of anvil cirrus in the Tropics.
- Most cirrus had T_c < -40 °C, were optically thin (σ < 0.5), and had monotonically decreasing P(σ) shapes. Most observed σ and P(σ) were consistent with small R.
- The observed dominance of small σ and monotonically decreasing P(σ) shapes was due to the observed N_{ice} and Δz distributions, which were both dominated by small values.
- Homogeneous nucleation alone can explain the observed cirrus N_{ice}. The mean M01 N_{ice}=0.1 cm^{-3} could be not be explained by observed background N_{IN} (N_{IN} < 0.1 cm^{-3} ((DeMott et al., 2003a); (Rogers et al., 1998)). Using parcel modeling, we demonstrated that homogeneous nucleation at w^h =7-11 cm sec^{-1} could explain the M01 mean observed N_{ice}. Plausible mesoscale w could exceed 7-11 cm sec^{-1}, while observed synoptic w rarely approached 7-11 cm sec^{-1}.

- Estimated sublimation timescales below cloud, i.e., τ_{sub}, were uniformly short (< 20 minutes) for typical crystal sizes (R_{eff}=35 μm). Therefore, observed cirrus Δz was primarily controlled by the depth and T of thin saturated layers.
- Combining the physical controls on N_{ice} and Δz, we concluded that observed P(σ) variability could result from homogeneous nucleation alone, variability in mesoscale w, and variability in the depth and T of thin saturated layers.

Our findings could be used to simplify the representation of cloud processes and radiative impacts at low temperatures (T < -40 °C). For example, homogeneous nucleation alone could be used to form cirrus. In addition, the observed dependence of std(σ) on $\overline{\sigma}$ was a useful way to estimate cirrus inhomogeneity and reduce associated OLR biases. We also, however, found some discouraging results for cirrus parameterization in large scale models. Large observed standard deviations in cloud variables suggest it would be difficult to predict the cirrus properties using T_c alone. We also found little dependence of cirrus cloud properties on Φ and on season, which served as a proxy for formation mechanism. Finally, two key variables that control cirrus σ inhomogeneity cannot be easily predicted by the current generation of climate models: meosocale variability in w^h and the depth of elevated saturated layers. Nevertheless, we recommend that the feasibility of incorporating small-scale w fluctuations and the thickness of elevated saturated layers into physically-based cirrus parameterizations should be evaluated.

Chapter 4:

MICROPHYSICAL AND DYNAMICAL CONTROLS ON OROGRAPHIC CIRRUS P(σ)

4.1. Introduction

4.1.1. Motivation

As described in Chapter 1, cirrus CRF depends on P(σ), T_c, and surface properties (Eq. 1.4). Neglecting cirrus inhomogeneity can lead to large biases in computed radiative fluxes (Fu et al. (2000), Carlin et al.(2001), Chapter 1, Chapter 3). Understanding the physical processes that influence cirrus inhomogeneity should improve the representation of cirrus cloud radiative impacts in weather and climate models.

In K06 and Chapter 2, we explored the sensitivity of cirrus σ to w, T, N_{aer} and N_{IN} along idealized lifting trajectories. For a typical range of w, N_{aer} and N_{IN}, we found that mean cirrus σ and P(σ) shape depend primarily on w. The sensitivity of mean σ to w resulted for two reasons: 1) As w^h increased, $J_{hom\text{-}max}$ increased, $N_{ice}{}^h$ increased and R_{eff} decreased. 2) As R_{eff} decreased, $\tau_{fallout}$ and cloud lifetimes increased. Background N_{IN} ($N_{IN} < 0.1$ cm^{-3}) only modified $\overline{\sigma}$ and P(σ) with large w.

For a fixed IWC and Δz, cirrus σ are controlled by N_{ice}. Therefore, understanding the physical factors that control observed N_{ice} is essential for understanding observed cirrus σ. In Chapter 3, we found that observed N_{IN} ((DeMott et al., 2003a), (Rogers et al., 1998)) and weak vertical motions could not explain the median observed N_{ice} at Lamont, OK (0.1 cm^{-3} (Mace et al, 2001)). As a result, we proposed that homogeneous nucleation and mesoscale variability in w could explain the observed N_{ice} variability. Using modeling and aircraft observations, Kärcher and Strom (2003) and Hoyle et al. (2005) have also concluded that mesoscale variability in w could explain the N_{ice} observations from the INCA and SUCCESS field campaigns. Using Lagrangian w trajectories from ECMWF with superimposed mesoscale variability in w, Haag and Kärcher (2004) found background concentrations of IN can reduce N_{ice}, but that the presence of IN did not affect where cirrus form. Taken together, Kärcher and Strom (2003), Hoyle et al.

(2005), Haag and Kärcher (2004), K06, and Chapters 2 and 3 of this dissertation all suggest heterogeneous nucleation plays a secondary role in explaining observed N_{ice} and cirrus formation.

To further investigate the atmospheric significance of these identified $w^h - N_{ice}$ connections, the influence of realistic cooling sequences on cirrus formation and evolution should be evaluated. Unfortunately, it is difficult to predict air flow and measure w along cirrus evolution pathways. Many cirrus field campaigns have focused on wave cloud case studies because wave cloud air flow trajectories are easier to predict and Lagrangian w can be measured (e.g., INTACC Field et al. (2001), FIRE II Heymsfield and Milosovich (1995)). With the exception of wave clouds, however, there is a dearth of Lagrangian atmospheric measurements of w. Many studies (e.g., Hoyle et al. (2005), Kärcher and Strom (2003), Haag and Kärcher (2004)) have used atmospheric w measurements and statistical methods to construct semi-Lagrangian air flow trajectories by superimposing mesoscale variability in w on Lagrangian displacement trajectories derived from large-scale atmospheric models. All of these studies discovered that mesoscale w variability (τ_{wave} ~ few minutes, w=3-300 cm sec^{-1}, cooling rates 1-100 K $hour^{-1}$) had a large influence on the resulting cirrus N_{ice}. In addition to the sensitivity of N_{ice} to w variability, Hoyle et al (2005) noted that N_{ice} was sensitive to the w sequencing.

Given the inherent difficulties in observing Lagrangian w in the atmosphere, kinematic trajectories extracted from a mesoscale weather model are a useful w proxy. In this chapter, we investigate cirrus processes occurring along high resolution trajectories extracted from the PSU/NCAR mesoscale model (MM5). Using the K06 adiabatic parcel model with binned ice microphysics (see Chapter 2 for description), we evaluate the effect of w sequences and IN parameterizations on cirrus evolution and $P(\sigma)$. We also compare parcel model cirrus with available cirrus observations and with the cirrus generated by a standard MM5 bulk microphysics scheme, the Reisner II scheme (Reisner et al. (1998)). Although the Reisner II scheme and the parcel model make different physical simplifications, their inter-comparison should be especially interesting because the Reisner II scheme does not include feedbacks between the w and N_{ice} (Figure 4.1).

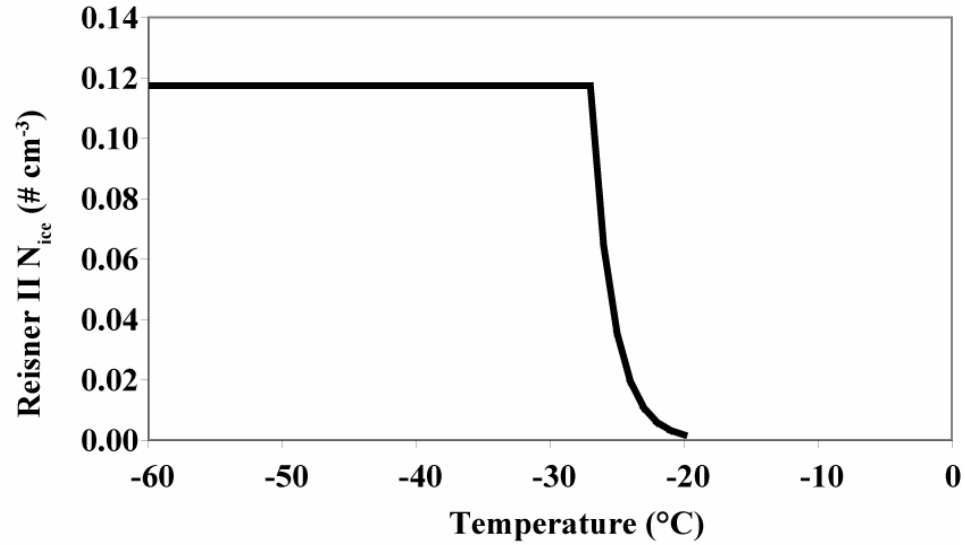

Figure 4.1: Ice number concentration predicted by the Reisner II bulk microphysical scheme. The N_{ice} predicted in a standard bulk microphysical scheme used in MM5, the Reisner II scheme (Reisner et al., 1998), does not depend on T or w in the regime where most cirrus form (T_c < 35 °C, see Figure 3.1, variable w).

Mountainous terrain provides a natural laboratory for investigating links between variable w and cirrus P(σ). Orographic cirrus are produced by mesoscale variability in w and are therefore often missed by climate models (Dean et al., 2005). Therefore, investigating the connections between MM5 w trajectories and orographic cirrus P(σ) should be both interesting and fruitful.

4.1.2. Chapter organization

In this chapter, we present an analysis of processes occurring along MM5 trajectories during an orographic cirrus event: In 4.2, infrared satellite and Raman lidar observations are used to introduce the orographic cirrus case study formation and evolution. In 4.3, we briefly review the representation of cirrus processes in our adiabatic parcel model. We also describe the methods we used to calculate trajectories along cirrus evolution pathways with the MM5. In 4.4, we present results including: 1) an overview and evaluation of the meteorology and w forecasted by MM5, 2) a description of the parcel model cirrus that formed along the MM5 trajectories with a focus on the influence of w and IN on cirrus optical properties, and 3) a comparison between the parcel model cirrus, the cirrus formed by the Reisner II scheme, hereafter Reisner II cirrus,

and the cirrus observations. Finally, in 4.5, we summarize and discuss the implications of the results presented in this chapter for parameterizing unresolved cirrus inhomogeneity.

4.2. April 19, 2001 cirrus observations

On April 19, 2001, orographic cirrus formation and evolution was observed by the GOES infrared satellite and a vertically pointing Raman lidar (Figure 4.2). From 6 to 16 UTC, GOES infrared imagery revealed cirrus formation in the lee of the Southern Rocky Mountains. After formation, the cirrus were advected east with the upper level winds. The cirrus were observed approximately 5-6 hours after formation by a ground-based Raman lidar at Lamont, OK. According to the lidar depolarization observations, the cirrus had a constant cloud top height of approximately 12 km, and a cloud base varying from 6.5 to 10 km. By 00 UTC April 20, 2001, the majority of cirrus had advected east of Lamont, OK and out of the lidar field of view.

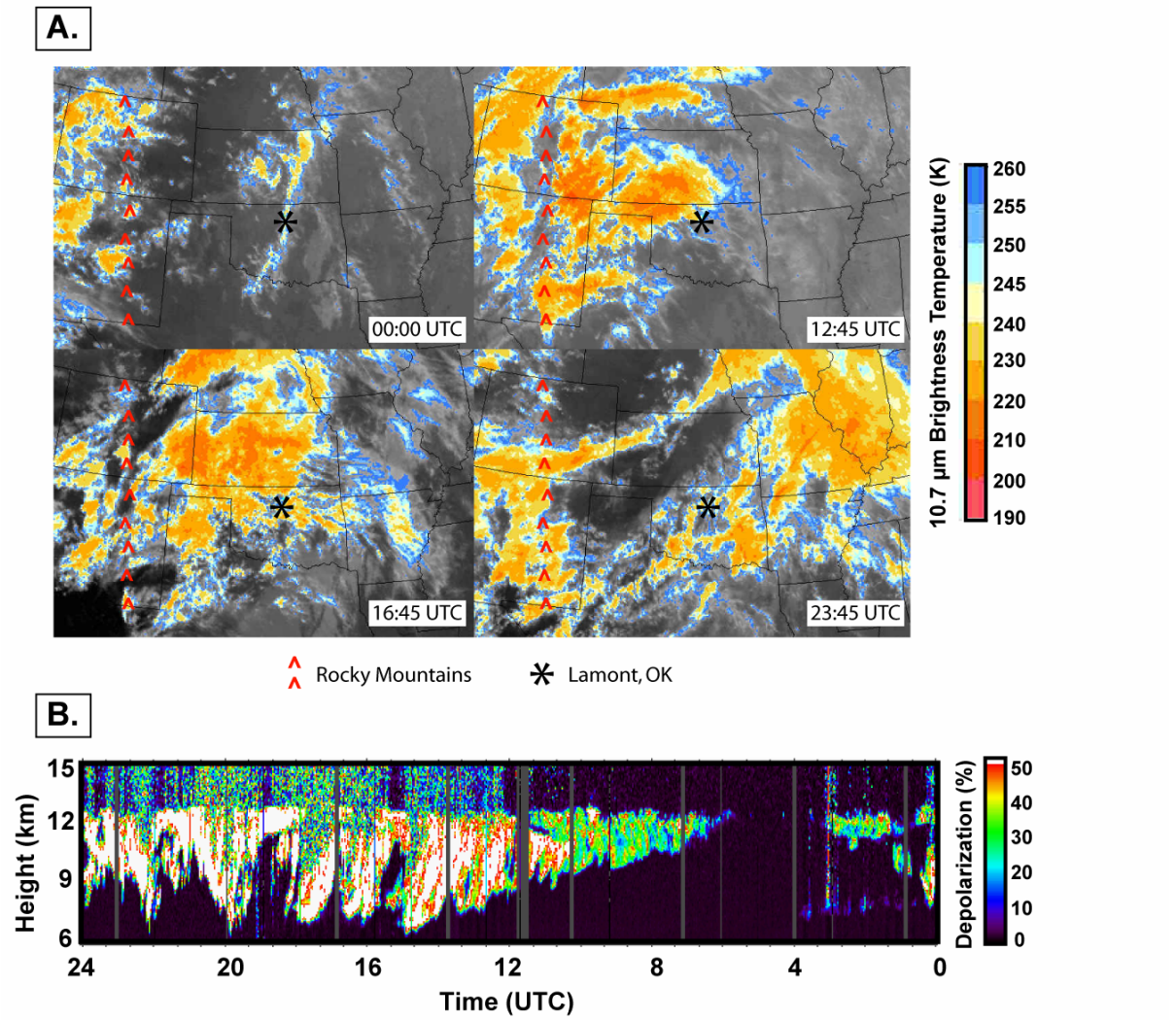

Figure 4.2: Infrared satellite and lidar depolarization observations on April 19, 2001. A. GOES infrared satellite image time series. Low brightness temperatures indicate high cloud tops. B. Vertically pointing Raman lidar depolarization observations**.** High Raman lidar depolarizations (DR > 10%) indicate ice. Cirrus formed in the lee of the Rockies and were observed ~5-6 hours after formation over Lamont, OK.

Ground-based observations from the Lamont, OK indicated cirrus were optically inhomogeneous (Figure 4.3). Two independent σ retrievals, one based on emissivity shape in the atmospheric window retrieved from Atmospheric Emitted Radiance Interferometer (AERI) observations (Turner, 2005), and the other based on Beer's law and the lidar backscatter below and above cloud, were generally consistent below an σ=3 (Figure 4.3a). Retrieved cirrus σ

increased monotonically from 6-12 UTC and then were variable, ranging from <0.1 to ~3. As a result of the σ variability, the observed P(σ) from 12-24 UTC was broad (Figure 4.3b).

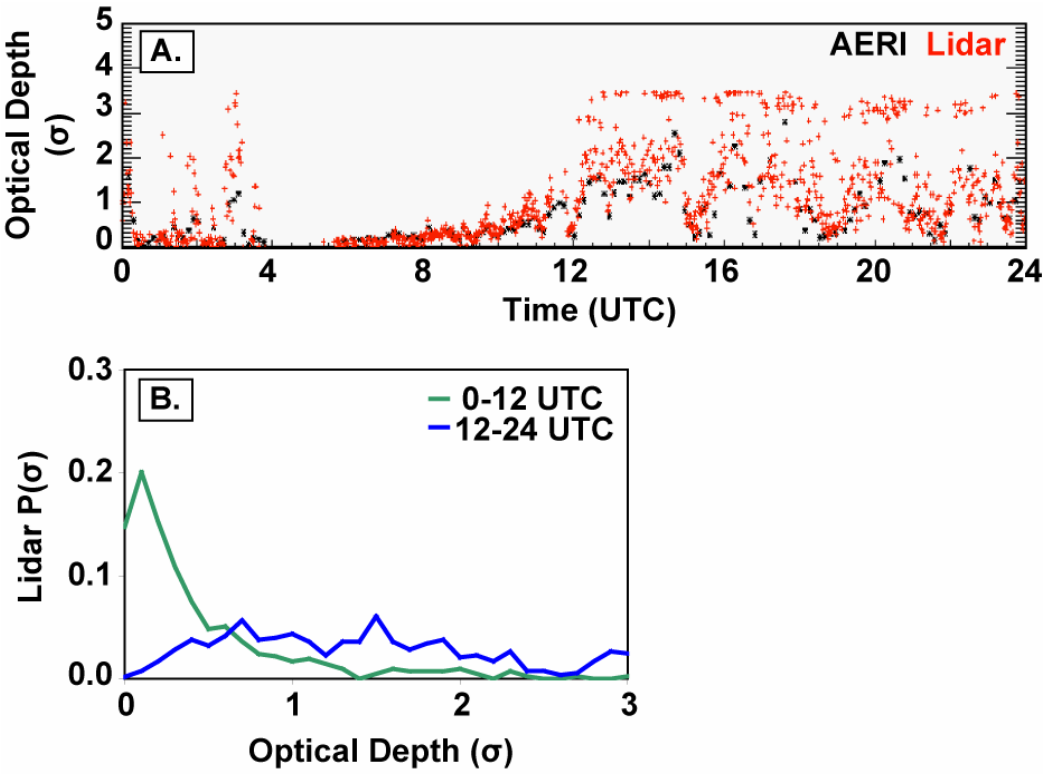

Figure 4.3: April 19, 2001 σ observations A. σ time series. Time series of cirrus σ based on two independent retrieval methods. B. 12-hour lidar-derived P(σ). From 12-24 UTC on April 19, 2001, cirrus over Lamont, OK had a broad P(σ).

Given the April 19, 2001 cirrus observations, we address the following specific research questions:

- What is the influence of w and initial conditions, including IN, on cirrus formation, N_{ice}, cirrus lifetimes, and σ along upper tropospheric w trajectories?

- What physical factors could explain the broad P(σ) observed at Lamont, OK?

4.3. Methods

4.3.1. Modeling cirrus along vertical velocity trajectories

To represent cirrus processes along w trajectories, we used the K06 parcel model and a simple conceptual framework (see Figure 2.1). With this parcel model framework, the computational requirements for estimating interactions between three-dimensional dynamics and binned microphysics are minimal. Another advantage of this parcel modeling framework is that it is relatively easy to understand and quantify interactions between the dynamics, aerosols, and cirrus cloud processes. For example, the start of a new nucleation event (i.e., $\frac{dN_{ice}}{dt} > 10^{-6}$ cm^{-3} sec^{-1}) is controlled both by the initial conditions, which set the total displacement required to start freezing, and by the displacement trajectory. If $RH_{crit\text{-}hom}$ is attained, w^h controls $J_{hom\text{-}max}$, and the resulting N_{ice} (see discussion in 2.3.2 and 2.4). If $RH_{crit\text{-}het}$ is attained, N_{IN} determines the resulting N_{ice}. Once cirrus form, their σ evolution is controlled by microphysical and dynamical timescales (Eq. 2.2 and Eq. 2.3).

Despite the described advantages, there are limitations for using a parcel model to represent cirrus processes along w trajectories. First, as described in Chapter 2, 100 m is a reasonable but ad hoc estimate for depth of the ice formation region (H). Cloud evolution is sensitive to H and vertically resolved cloud processes would be more realistic. Although the quantitative value of σ depends on H, the trends in σ and P(σ) shape are largely independent of H. Second, the observed cloud includes both the ice formation region and the ice fallout region, so as described in Chapter 2, we estimate cloud σ using the parcel model N_{ice} and R_{eff} and assuming Δz=1000 m. A constant cloud depth and a linear scaling of the formation region properties may not always be justified. For example, variable microphysical processes below the formation layer could result in nonlinear scaling. In addition, in Chapter 3, we found that Δz variability contributes to σ variability. However, we also demonstrated that sublimation below cloud is unlikely to contribute to σ variability.

4.3.2. MM5 trajectory calculations and cirrus modeling strategies

We ran the MM5 with three nested domains (D1, D2, D3) for 36 hours starting at 12 UTC April 18, 2001 (Figure 4.4, Table 4.1). All domains included both the Front Range of the

Rocky Mountains where the GOES imagery revealed orographic cirrus formation, and Lamont, OK where the inhomogeneous cirrus were observed by the Raman lidar. The fidelity of the MM5 forecast was evaluated using National Weather Service (NWS) reanalysis at fixed pressure levels and radiosonde stability and wind observations. Using the MM5 wind fields saved at 3.6 minute intervals, we calculated 8-hour kinematic w trajectories ending above Lamont, OK.

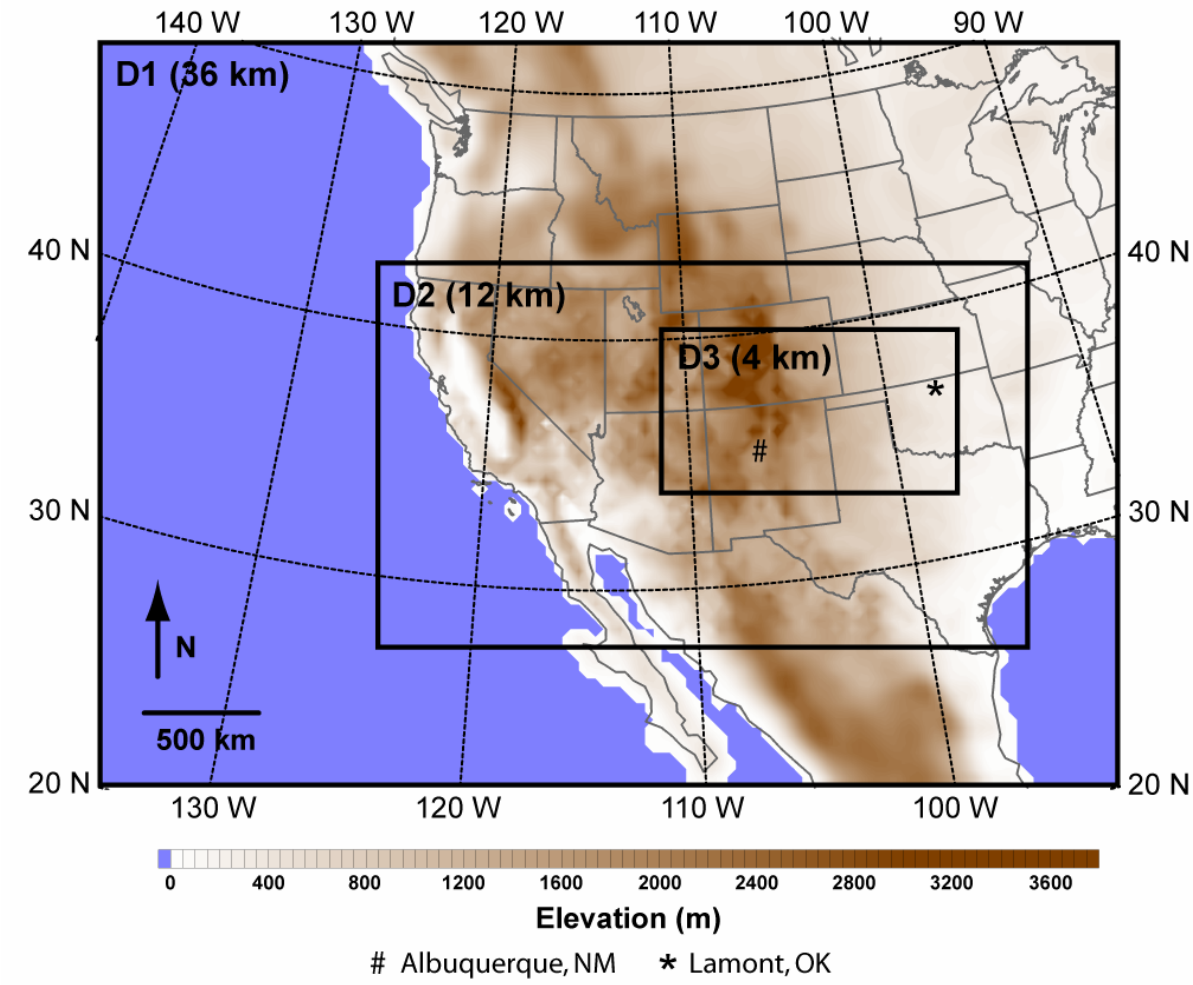

Figure 4.4: Domain configuration used for the April 18-20, 2001 MM5 forecast.

Table 4.1: MM5 V3.7.3 configuration used in this study

MM5 model specification	Value
Forecast duration	36 hours starting at 12 UTC April 18, 2001
Spatial resolution	D1 – 36 km, D2 – 12 km, D3 – 4 km
Temporal resolution	D1 – 240 seconds, D2 – 80 seconds, D3 – 27 seconds
Vertical resolution and extent	50 levels from 0 to 100 km, average vertical resolution 6-13 km ~500 m
Initialization	NCER/NCAR Reanalysis Project
Microphysics parameterization (IMPHYS)	Reisner II (Reisner et al., 1998)
Cumulus parameterization (ICUPA)	Kain Fritsch
Shallow convection option (ISHALLO)	No shallow convection
Radiation parameterization (FRAD)	CCM2
Nudging	none

Given the observed cirrus cloud top and timing (Figure 4.2), we focused our modeling efforts on cirrus formation and evolution along trajectories ending 12 km above Lamont, OK from 8 to 24 UTC. We calculated cirrus evolution with our parcel model along trajectories that ended over Lamont, OK every 3.6 minutes. We compared the $P(N_{ice})$ and $P(\sigma)$ calculated along trajectories derived from the 4 km and 12 km MM5 domain (Table 4.2). We also evaluated the effect of IN on cirrus $P(N_{ice})$ and $P(\sigma)$ along trajectories using both a fixed background concentration (IN=0.03 cm^{-3}) and the commonly used Meyers et al (1992) IN parameterization. Finally, we compared parcel model cirrus to the cirrus produced by the Reisner II bulk microphysical scheme, i.e., the Reisner II cirrus, and the lidar cirrus observations.

Table 4.2 Parcel model runs along MM5 vertical velocity trajectories. All parcel model (PM) runs are named as follows: PM_"MM5 Domain"_"ice nuclei parameterization (if applicable)". All parcels were initialized with sulfuric acid aerosols (dry mass of 10^{-16} kg, N_{aer}=100 cm^{-3}).

Parcel Model (PM) Run	IN Parameterization	Source for initial conditions (T, P, and RH_{ice})	Source for vertical velocity trajectories (w)
PM_D3	None	From MM5 D3	From MM5 D3
PM_D3_IN	"background IN" : N_{IN}=0.03 cm^{-3} shifted water activity freezing threshold (Kärcher and Lohmann, 2002) with critical RH_{ice} ~130%	From MM5 D3	From MM5 D3
PM_D3_Meyers	"Meyers": N_{IN} is an exponential function of ice supersaturation. (Meyers et al. (1992), K06 Eq. 4)	From MM5 D3	From MM5 D3
PM_D1	none	From MM5 D1	From MM5 D1

4.4. Results

4.4.1. Overview of results

We first describe and evaluate the meteorological conditions (4.4.2) and w (4.4.3) forecasted by the MM5. Next, we describe the effect of w sequences and IN parameterization on parcel model cirrus processes and statistics (section 4.4.4). Then, we contrast cirrus formed by the parcel model with the Reisner II cirrus (section 4.4.5). Finally, we compare the modeled cirrus to the cirrus observations and explain why the inhomogeneity, but not the timing, of the observed cirrus can be reproduced by the parcel model (section 4.4.6).

4.4.2 MM5 meteorology on April 19, 2001

On April 19, 2001, the MM5 forecasted a broad upper level ridge over the central USA, relatively warm air in the lee of the Rocky Mountains, and a low pressure system centered in south east Montana. At 12 UTC, the upper level ridge resulted in southwesterly flow across the Rocky Mountains (Figure 4.5a). Lee cyclogenesis in Montana occurred at ~6 UTC in association with an upper level short wave. By 12 UTC, the developing Montana low pressure had an 850 mb central geopotential height of 1332 m (Figure 4.5b). In the lee of the Rockies, a region of low pressure termed a "lee trough" formed in association with adiabatic warming of descending air. A cross section of equivalent potential temperatures shows the lee trough, a cold front aloft above the Rockies, and a warm front approaching northern Oklahoma (Figure 4.5c). Both the lee trough and the developing low contributed to the weak North-South trending warm front. Circulation vectors with the mean motion of the cold front removed demonstrate that air above 8 km had net westerly air flow.

The MM5 forecast (Figure 4.5) was broadly consistent with the NWS reanalysis observations, however, the MM5 had weaker dynamics in the south central US. Compared to the reanalysis, the MM5 had a stronger and tighter Montana low, and a reduced gradient in, and lower overall, 500 mb geopotential heights over the Rockies. In the south central USA, these model geopotential height biases indicate that the MM5 forecast had reduced wind speeds over the Rockies, and weaker frontal lifting than what was observed.

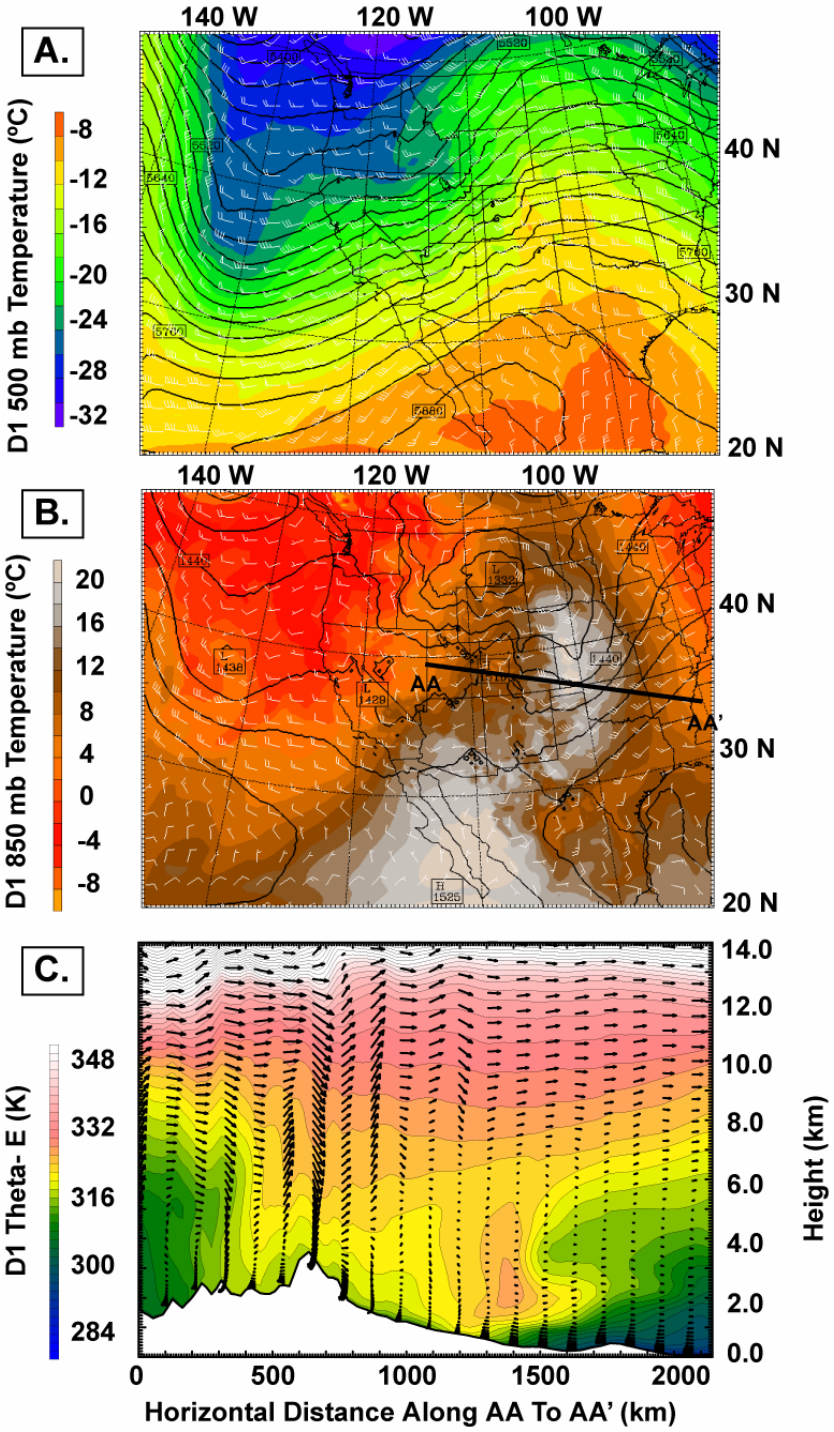

Figure 4.5: MM5 meteorology at 12 UTC on April 19, 2001 A. 500 mb temperatures and geopotential heights B. 850 mb temperatures and geopotential heights. C. Cross section through AA-AA'. Circulation vectors have the mean speed of the cold front removed (12.7 $msec^{-1}$).

4.4.3. MM5 vertical velocities on April 19, 2001

Above the Rockies in New Mexico and Colorado, the MM5 forecasted large and variable w within the 4 km MM5 domain (D3) (Figure 4.6).

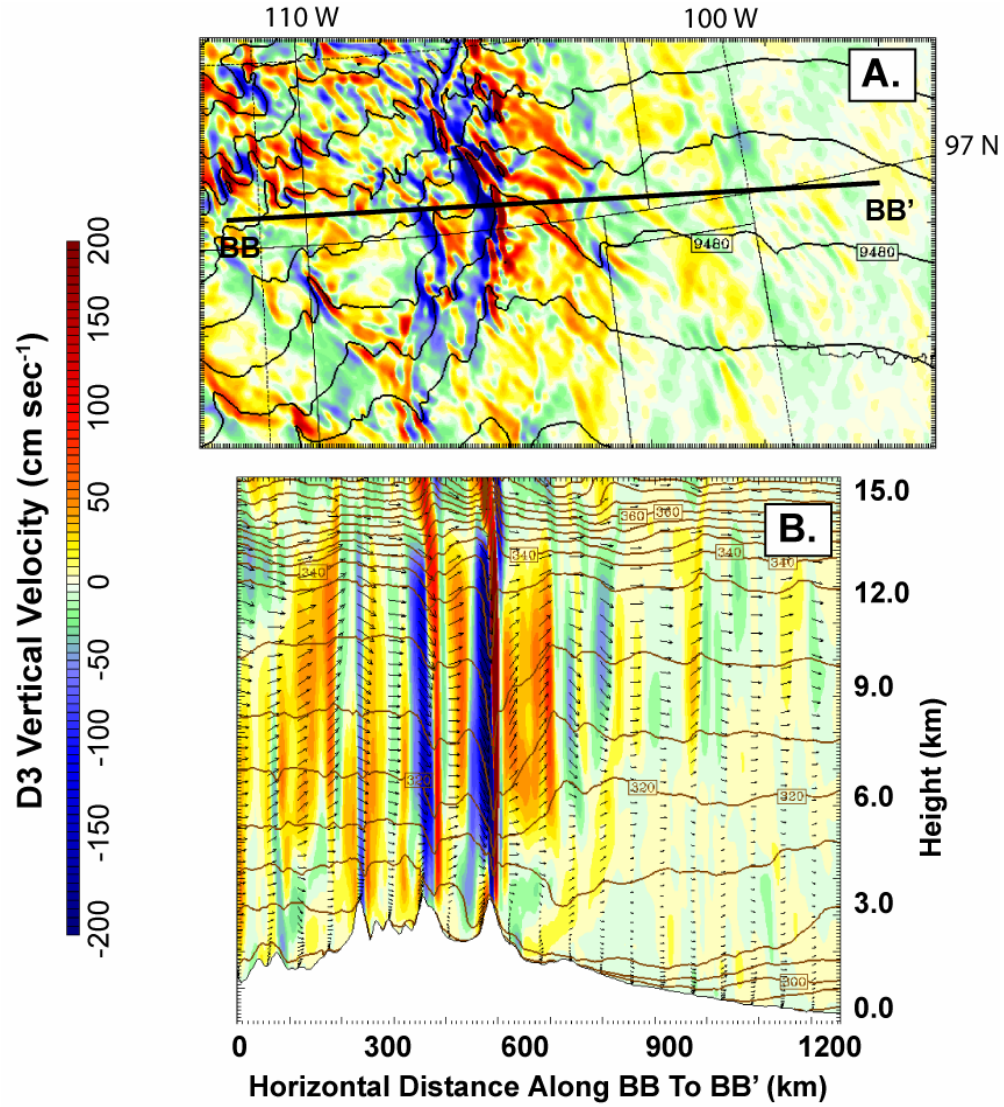

Figure 4.6: MM5 vertical velocities at 12 UTC on April 19, 2001. A. D3 300 mb vertical velocity B. D3 vertical velocity cross section. Location of cross section BB-BB' is indicated on A. The MM5 forecasted large and variable vertical velocities in the lee of the Rockies.

On April 19, 2001, upper level winds were broadly perpendicular to the Rockies and resulted in vertically propagating orographic gravity waves with large (> 100 cm/sec) and variable w. The strongest vertical motions resulted from 12-15 UTC when the upper level winds were perpendicular to the Front Range and the cold front aloft approached the western edge of the lee trough. The complex topography resulted in non-hydrostatic gravity waves downwind of the Rockies, but w beyond the mountainous topography were generally smaller (<50 cm/sec).

The orographic gravity waves and the changing upper level wind direction influenced the T and w along D3 trajectories ending 12 km above Lamont, OK. The path of the 12 km trajectories evolved with time reflecting shifts in the upper level winds (Figure 4.7), but all 12 km trajectories traveled over the high topography of the Rocky Mountains 5 to 7 hours before arriving at Lamont, OK (Figure 4.8a). T and w along the 12 km trajectories show the Lagrangian dynamical forcing important for cirrus formation and evolution (Figure 4.8b, Figure 4.8c). Cooling occurred along the 12 km trajectories 5-6 hours and 2-3 hours prior to arrival at Lamont, OK. The 12 km trajectories had large w associated with the vertically propagating orographic gravity waves 5-6 hours before arriving at Lamont, OK. For the last 4 hours prior to arrival at Lamont, OK, the 12 km trajectories had smaller vertical motions.

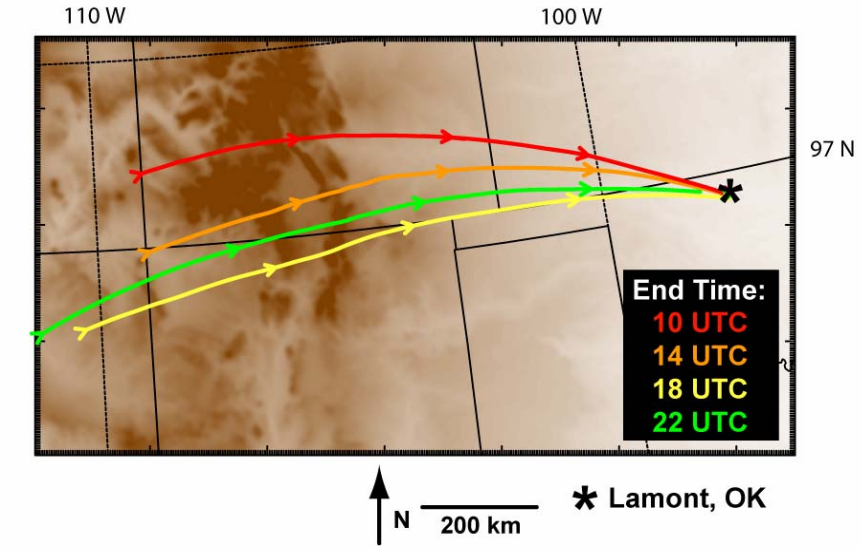

Figure 4.7: Planar view of D3 MM5 trajectories ending 12 km above Lamont, OK. Trajectories pathways changed as the upper level winds evolved.

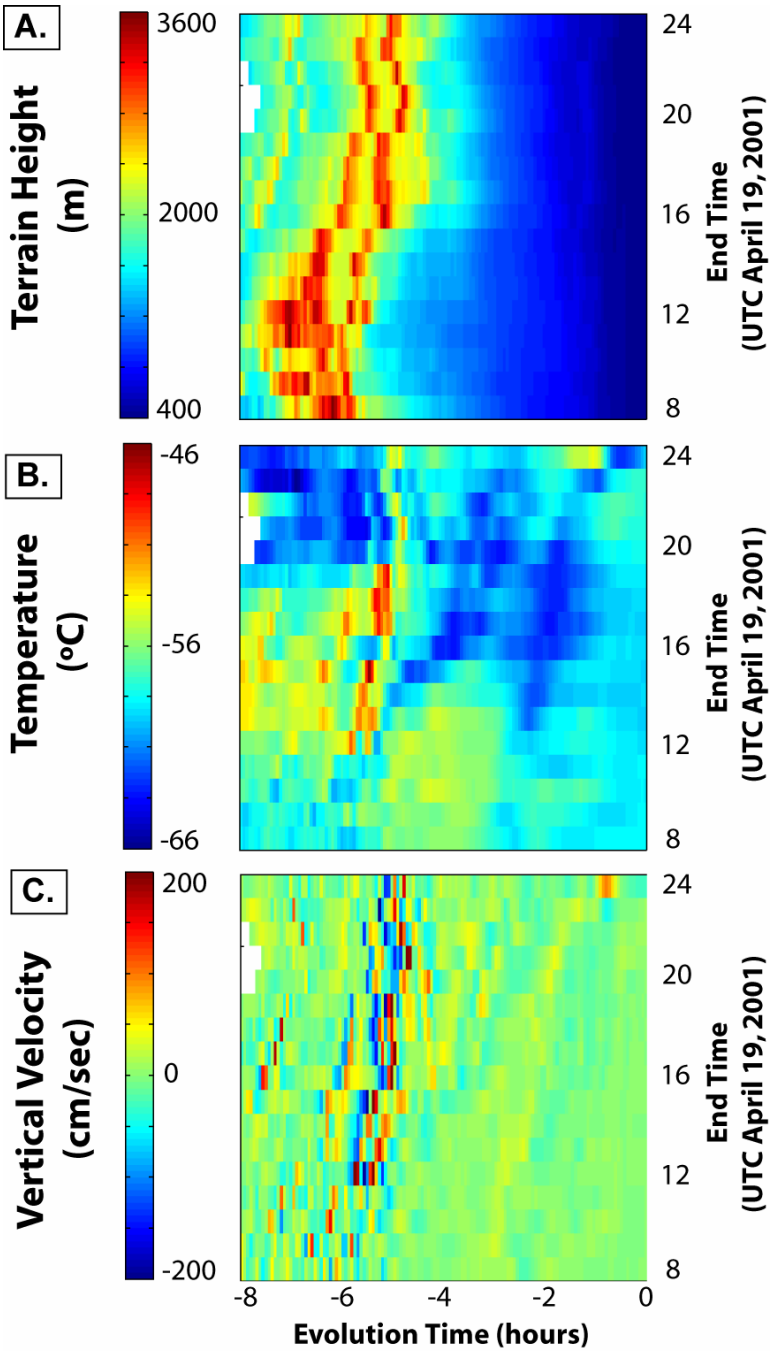

Figure 4.8: Terrain, temperature, and vertical velocity along MM5 trajectories ending 12 km above Lamont, OK. These time-time plots show the Lagrangian evolution of the MM5 dynamical forcing on air parcels arriving 12 km above Lamont, OK. The y-axis indicates the parcel arrival time at Lamont. The x-axis indicates the time before parcel arrival at Lamont. Cooling in the lee of the Rockies from evolution time -6 to -4 could explain the observed cirrus formation (Figure 4.2).

The spatial resolution of the MM5 domain influenced the amplitude and spatial scale of w along the 12 km trajectories (Figure 4.9). With 4 km resolution, MM5 D3 had a larger range of w than the 36-km MM5 domain 1 (D1) (Figure 4.9a). D3 also had greater spectral power at larger frequencies (spatial equivalent 20-60 km) than D1 (Figure 4.9b, Figure 4.9c). Given these dynamical differences, contrasting cirrus properties along the 12 km w trajectories derived from D1 and D3 should help elucidate the importance of mesoscale w variability and amplitude for cirrus formation and evolution.

The sensitivity of the modeled w to model domain resolution and the lack of w observations made it difficult to quantitatively validate the MM5 w amplitudes and variability. As a result, we qualitatively assessed the MM5 w forecasts within the context of the two main drivers of orographic wave development: the mountain range topography and the upwind atmospheric stability and wind profile (Durran, 2003).

Within the 4 km domain, orographic wave development was consistent with simple mountain wave theory and models. Mountain wave theory suggests that given the large width of the Front Range, vertically propagating hydrostatic waves should result for most atmospheric stability and wind profiles. Thus, the vertically propagating gravity waves in MM5 are consistent with expectations from simple mountain wave theory (Figure 6b). With the relatively steep leeward slope of the Front Range, idealized calculations suggest hydrostatic gravity waves could generate positive displacement at cirrus heights (see Durran (2003), Figure 20.11). At upper levels, persistent positive w in the lee of the Rockies resulted from 6-12 km (Figure 4.6b).

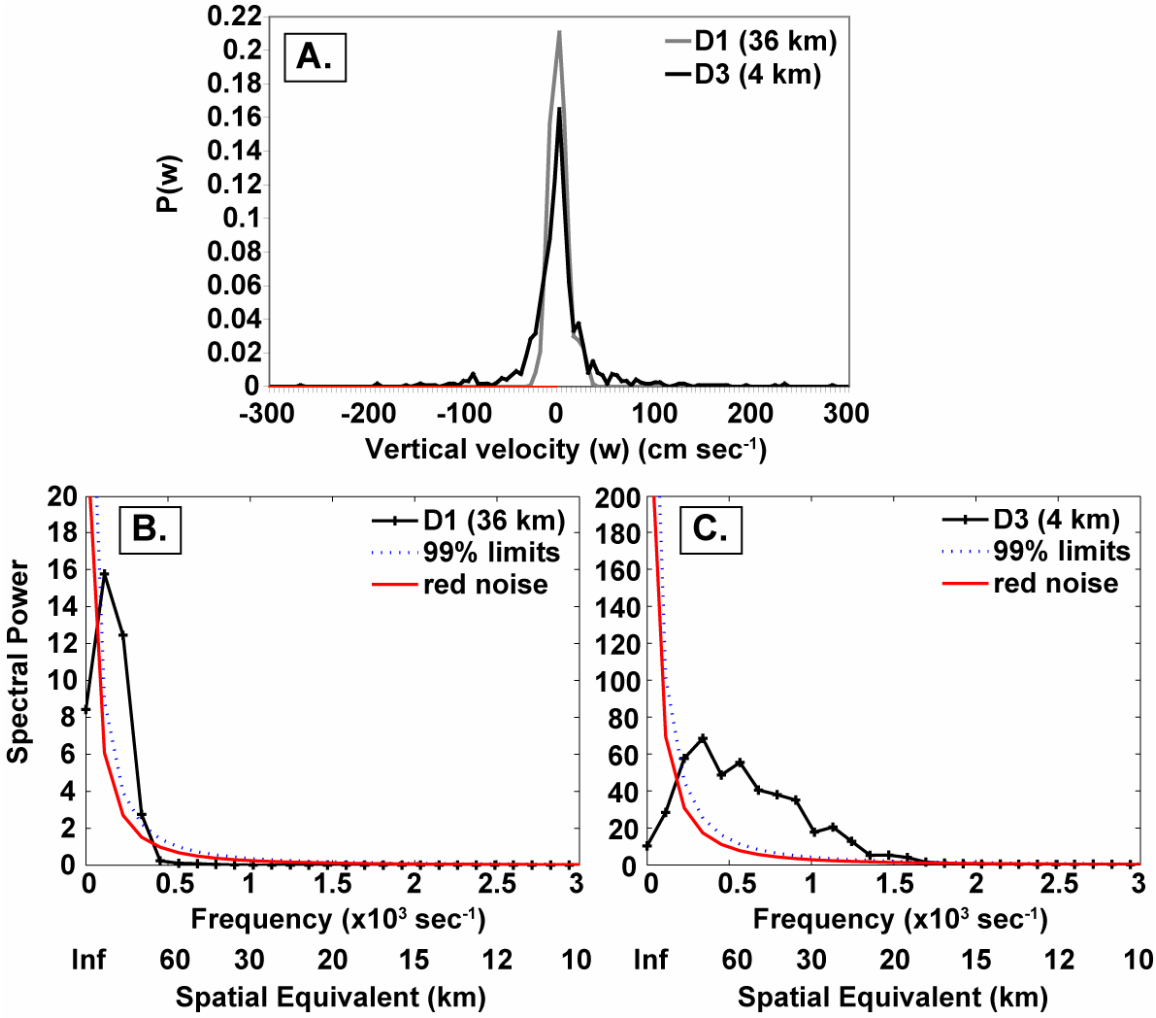

Figure 4.9: The effect of MM5 domain resolution on vertical velocity amplitude and frequency structure. D3 had a larger range of w and more mesoscale variability in w than D1. Note: To calculate a spatial equivalent for frequency, we assumed a horizontal wind speed of 30 m sec^{-1}.

To evaluate MM5's representation of the wind and stability profiles important for gravity wave evolution, we compared the modeled and observed soundings at Albuquerque, New Mexico (ABQ). The MM5 D3 sounding was qualitatively similar to the ABQ radiosonde sounding, increasing confidence in the MM5 upstream boundary conditions for orographic wave formation (Figure 4.10). Both the observed and modeled ABQ sounding had a stable atmospheric potential temperature profile and increasing wind speed with height. Differences between the MM5 and

the observed ABQ sounding included: 1) the MM5 ABQ sounding was more stable and 2) the MM5 ABQ sounding had less vertical wind speed shear above 8 km.

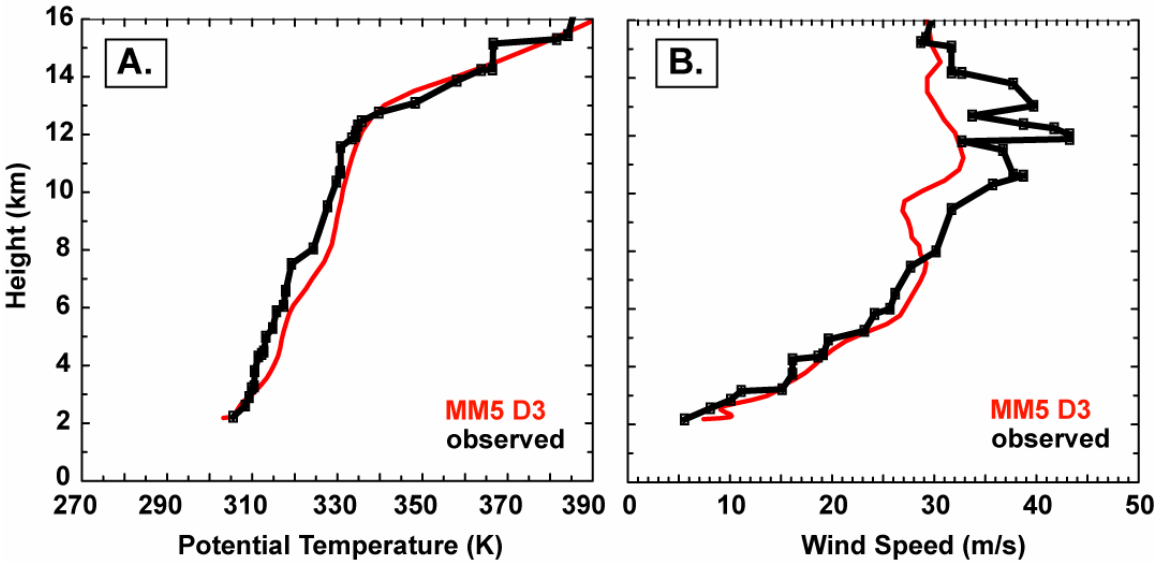

Figure 4.10: ABQ April 19, 2001 12 UTC sounding comparison a. MM5 vs. observed stability profile b. MM5 vs. observed wind speed profile

4.4.4. Parcel model cirrus along MM5 trajectories

Contrasting parcel model cirrus evolution along two example trajectories highlights the effect of w on cirrus N_{ice}, σ, and lifetimes (Figure 4.11). Both the 12 km trajectory ending at 15 UTC and the 12 km trajectory ending at 16 UTC had large w and cooling from evolution time -6 to -4 (Figure 4.11a, Figure 4.11b). As a result, both parcels reached large RH_{ice} (Figure 4.11c), formed cirrus (Figure 4.11d, Figure 4.11e, Figure 4.11f), and were dehydrated as ice crystals fell out (Figure 4.11g). With homogeneous nucleation only (solid lines), the N_{ice} along the 16 UTC trajectory was larger than along the 15 UTC trajectory because the 16 UTC trajectory had a larger w^h and $J_{hom\text{-}max}$. As a result of the large N_{ice}, the cirrus along the 16 UTC trajectory also had smaller R_{eff}, larger σ, and a longer lifetime.

Adding background IN (N_{IN}=0.03 cm^{-3}) to the parcel changed the timing and magnitude of homogeneous nucleation (Figure 4.11). Along the 15 UTC trajectory, the addition of IN altered $J_{hom\text{-}max}$, but not the timing of homogeneous nucleation and w^h. As a result, the addition of

IN had a minor influence on the resulting N_{ice}, IWC, σ, and dehydration evolution. In contrast, along the 16 UTC trajectory, IN changed $J_{hom\text{-}max}$, the homogeneous nucleation timing, and w^h. As a result, the addition of IN increased N_{ice} and resulted in an optically thicker cloud with a longer lifetime and less dehydration. Contrasting the influence of IN on the cirrus formed along these two trajectories affirms the sensitivity of cirrus evolution to initial conditions and w sequences. In addition, the contrasting influence of IN along these two trajectories demonstrates that it is difficult to predict the influence of IN along any individual Lagrangian trajectory.

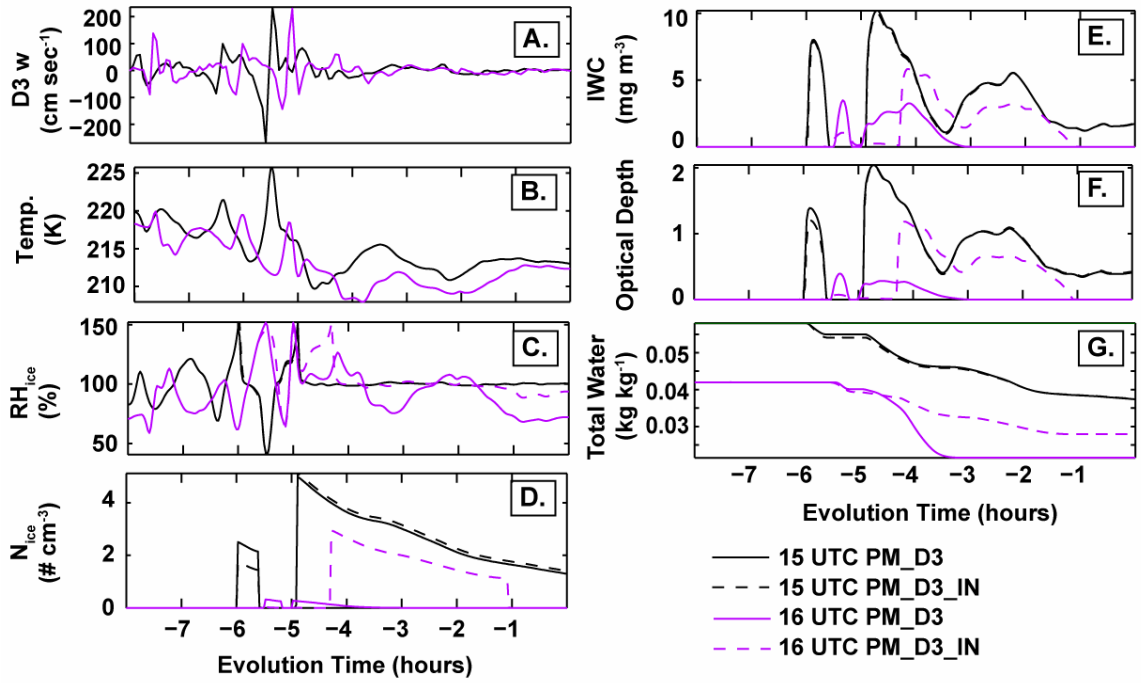

Figure 4.11: Parcel model cirrus evolution along two trajectories. Parcel model cirrus properties are plotted for trajectories ending 12 km above Lamont, OK at 15 UTC and 16 UTC. A. MM5 D3 vertical velocity trajectories B. Parcel model temperature C. Parcel model RH_{ice} D. Parcel model N_{ice} E. Parcel model IWC F. Parcel model σ, assuming 10x scaling G. Parcel model total water

Variability in total displacement, w^h, and initial conditions resulted in a range of cirrus formation times, N_{ice}, R_{eff}, and cloud lifetimes along 12-km trajectories upwind of Lamont, OK (Figure 4.12). For many trajectories, cooling in the lee of the Rockies led to homogeneous nucleation 3-5 hours before arriving at Lamont, OK (Figure 4.8, Figure 4.12). Cirrus evolution was variable, but three general classes of evolution could be categorized by arrival time at

Lamont, OK. Along trajectories arriving above Lamont, OK from 12-14 UTC, cirrus formed by homogeneous nucleation at evolution time -5, but then sublimated in descending motions. After a cloud-free period, a second homogeneous freezing event occurred at evolution time -3 and these cirrus persisted to Lamont, OK. Along trajectories arriving above Lamont, OK from 15-19 UTC, cirrus formed from evolution time -5 to -3 hours. Variability in w^h led to a range of N_{ice} and cloud lifetimes. Only the trajectories with large N_{ice} and little descending motion persisted over many hours and arrived at Lamont, OK. Finally, along trajectories ending from 20-24 UTC, cirrus formed from evolution time -8 to -7, but no cirrus formed in the lee of the Rockies, and no cirrus arrived at Lamont, OK.

The addition of background IN concentrations increased cirrus cloud cover and changed the timing and magnitude of homogeneous nucleation events (Figure 4.13). Although IN did change the resulting cirrus evolution along trajectories upwind of Lamont, OK, the timing of cloud formation, the variability in N_{ice} and cloud lifetimes, and the cirrus arriving at Lamont, OK were not dramatically changed by the addition of background IN.

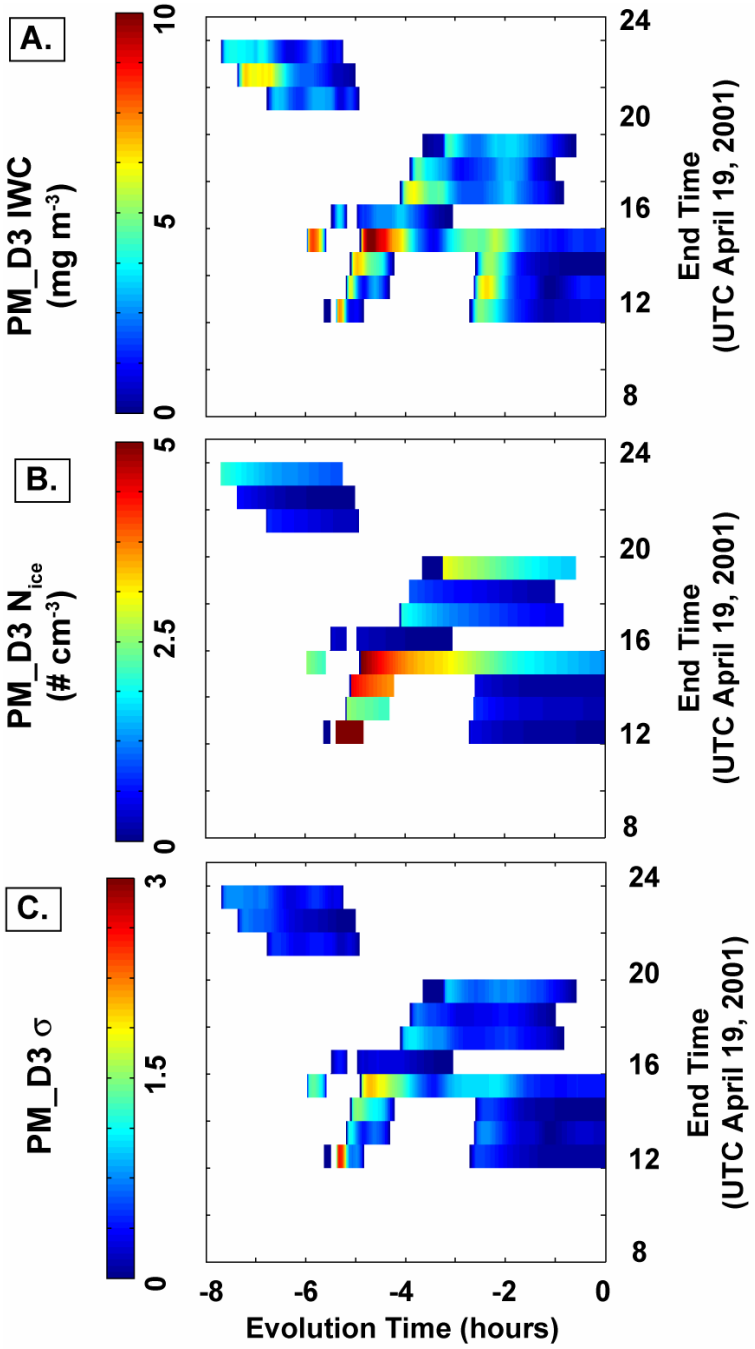

Figure 4.12: Parcel model cirrus along hourly trajectories: homogeneous nucleation only. IWC, N_{ice} and σ from the parcel model are plotted along Lagrangian trajectories ending every hour 12 km above Lamont, OK. White indicates no cloud was present (IWC < 0.001 mg m^{-3}). See Table 4.2 for parcel model configuration details and naming conventions. See Figure 4.8 for a description of time-time plots.

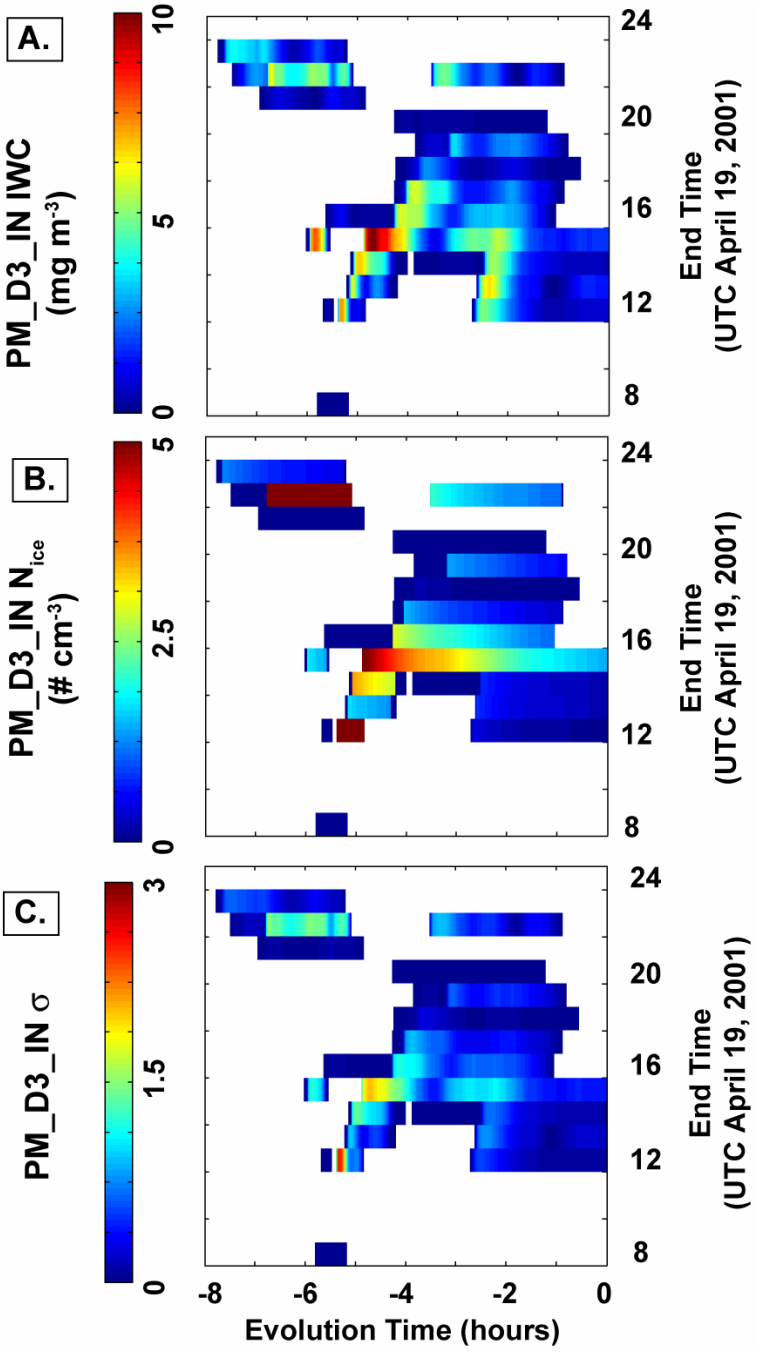

Figure 13. Parcel model cirrus along hourly trajectories: homogeneous and heterogeneous nucleation IWC, N_{ice} and σ from the parcel model are plotted along Lagrangian trajectories ending every hour 12 km above Lamont, OK. White indicates no cloud was present (IWC < 0.001 mg m^{-3}). See Table 4.2 for parcel model configuration details and naming conventions. See Figure 4.8 for a description of time-time plots.

We compared $P(N_{ice})$ and $P(\sigma)$ derived from 200 trajectories to statistically assess the influence of domain resolution on parcel model cirrus. By comparing cirrus formed along D1 (36 km spatial resolution) and D3 (4 km spatial resolution) trajectories, we found the mesoscale w variability and larger w amplitudes in D3 broadened $P(\sigma)$ and shifted $P(N_{ice})$ towards larger values (Figure 4.14). Given that larger D3 N_{ice} led to longer D3 fallout timescales and longer D3 cloud lifetimes, we were surprised to find that the horizontal resolution of the MM5 domain did not have a large impact on overall cloud cover. Owing to their differing dynamics, however, MM5 trajectories derived from D1 and D3 had different overall cooling evolutions. This suggests that the influence of w (i.e., cooling rate) on cloud lifetimes and cloud cover may not be revealed by our simple D1 and D3 comparisons.

For $P(N_{ice})$ and $P(\sigma)$ derived from 200 trajectories, the addition of IN always increased the cloud fraction by increasing the occurrence of cirrus with low N_{ice} and small σ (Figure 4.15). The increase in optically thin cirrus resulted because aerosols with IN had a lower freezing threshold than aerosols without IN. The impact of IN on optically thick cirrus, however, depended on the IN parameterization Due to scavenging and their relatively low concentrations, background IN had little impact on the large σ and large N_{ice} cirrus that formed by homogeneous nucleation. In contrast, the use of the Meyers parameterization suppressed homogeneous nucleation and the occurrence of large N_{ice} and large σ cirrus. The Meyers et al (1992) parameterization produced more IN than are typically observed in the atmosphere (Meyers $N_{IN} > 0.3$ cm^{-3}). Therefore, we suggest that our background N_{IN} modeling results are more likely to represent the typical influence of IN on cirrus.

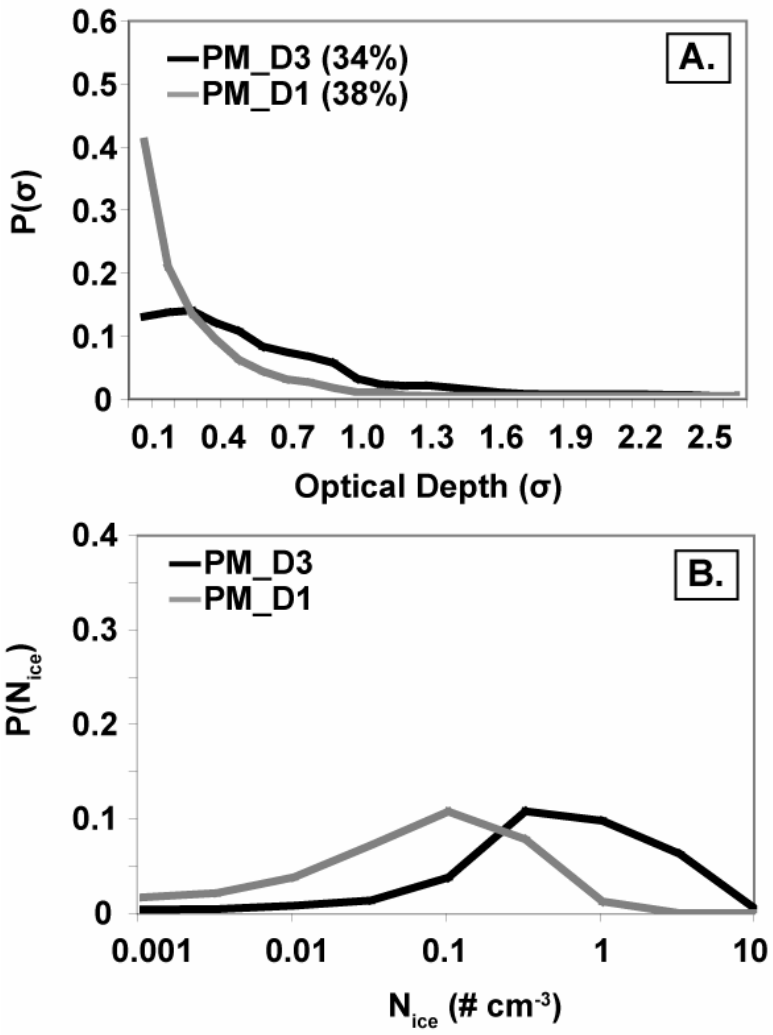

Figure 4.14: Influence of MM5 domain resolution on parcel model P(σ) and P(N_{ice}).
P(σ) and P(N_{ice}) were calculated along trajectories ending 12 km above Lamont, OK from 12-24 UTC. The cloud fraction (cf) is listed in () after the parcel model run name. Cloudy air must have an IWC greater than 0.001 mg m^{-3}. P(N_{ice}) were calculated for N_{ice} > 0.001 cm^{-3}. P(σ) were calculated for σ > 0.1. See Table 4.2 for parcel model configuration details and naming conventions.

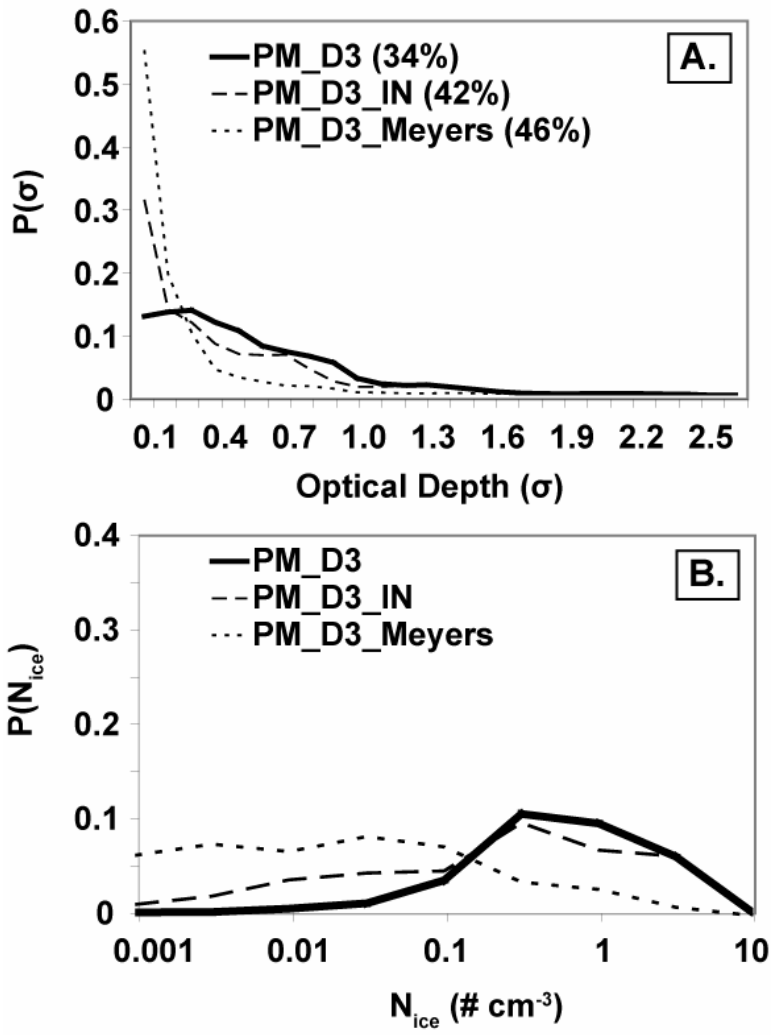

Figure 4.15: Influence of IN on parcel model P(σ) and P(N_{ice}). P(σ) and P(N_{ice}) were calculated along trajectories ending 12 km above Lamont, OK from 12-24 UTC. The cloud fraction (cf) is listed in () after the parcel model run name. Cloudy air must have an IWC greater than 0.001 mg m^{-3}. P(N_{ice}) were calculated for $N_{ice} > 0.001$ cm^{-3}. P(σ) were calculated for $\sigma > 0.1$. See Table 4.2 for parcel model configuration details and naming conventions.

4.4.5. Reisner II cirrus along MM5 trajectories

Like the parcel model, the Reisner II bulk microphysical scheme generated cirrus in the lee of the Rockies (Figure 4.16). Unlike the parcel model cirrus, the Resiner II cirrus had a fixed maximum N_{ice} of ~0.12 cm^{-3} that was unrelated to the w along the trajectories (Figures 4.1, 4.16, and 4.17). Also unlike the parcel model cirrus, the Resiner II cirrus had a similar evolution along

trajectories arriving at Lamont, OK from 12-20 UTC: Resiner II cirrus formed in the lee of the Rockies from -6 to -3 evolution time, sublimated, formed again at evolution time -2, and then sublimated. With the exception of 8-12 UTC, no Resiner II cirrus were present over Lamont, OK.

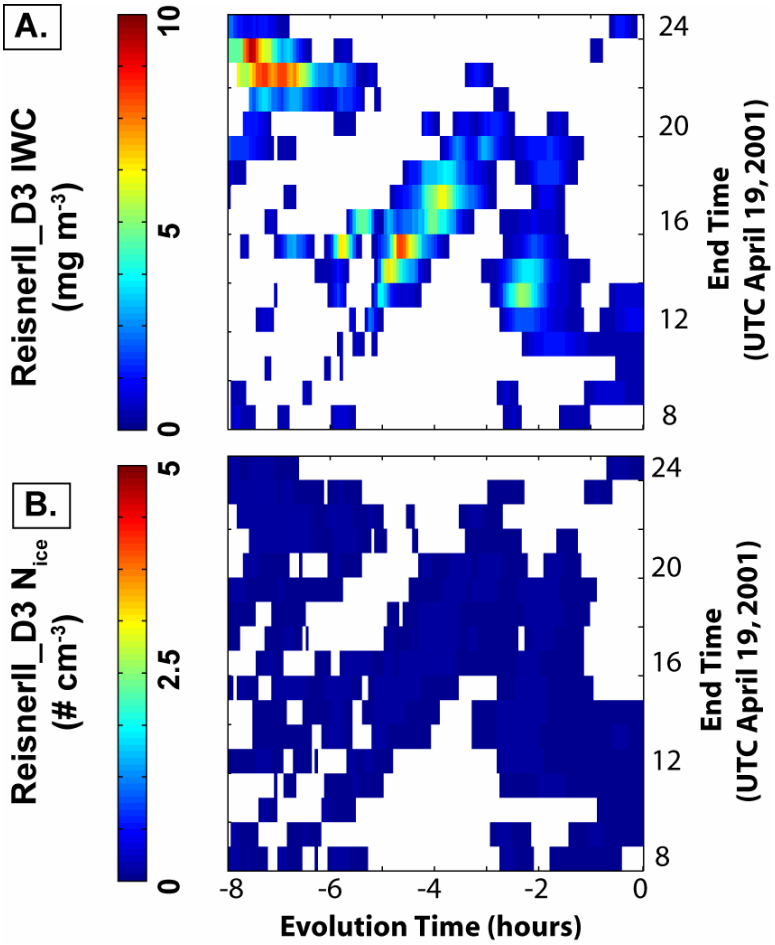

Figure 4.16: Reisner II cirrus along hourly trajectories. IWC and N_{ice} generated by the Reisner II microphysical scheme in MM5 D3 are plotted along trajectories ending every hour 12 km above Lamont, OK. White indicates no cloud was present.

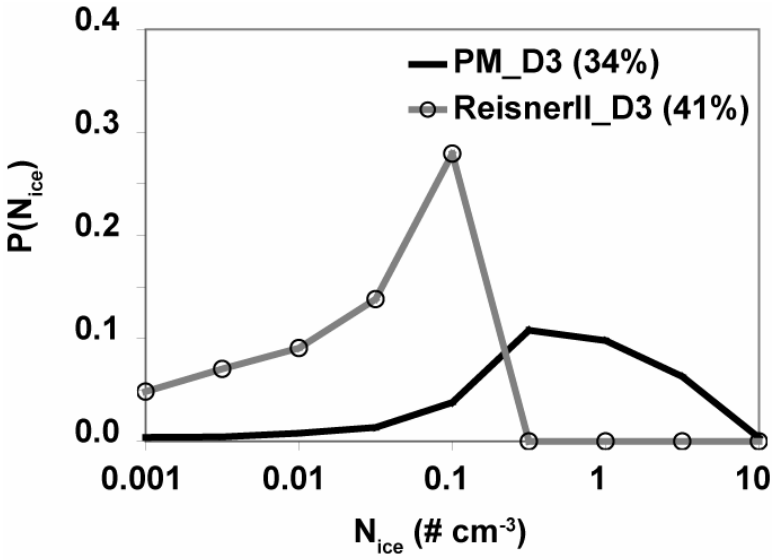

Figure 4.17: Comparison of parcel model and Reisner II P(N_{ice}). P(N_{ice}) were calculated along trajectories ending 12 km above Lamont, OK from 12-24 UTC. The cloud fraction (cf) is listed in () after the parcel model run name. Cloudy air must have an IWC > 0.001 mg m^{-3}. P(N_{ice}) were calculated for N_{ice} > 0.001 cm^{-3}. See Table 4.2 for parcel model configuration details and naming conventions.

4.4.6. Comparison of modeled and observed cirrus

Both the parcel model and Reisner II scheme failed to reproduce the observed cirrus presence above Lamont, OK. The lidar depolarization showed cirrus occurring continuously from 8-24 UTC, yet both the Reisner II and parcel model resulted in essentially no cirrus above Lamont, OK after 16 UTC (Figure 4.18, Figure 4.2). Modeled RH_{ice} above Lamont, OK was below ice saturation after ~15 UTC (Figure 4.19). Low RH_{ice} resulted from net warming in the two hours before trajectories arrived at Lamont, OK (Figure 4.8). Given the low RH_{ice}, it is not surprising that few model cirrus arrived at Lamont, OK.

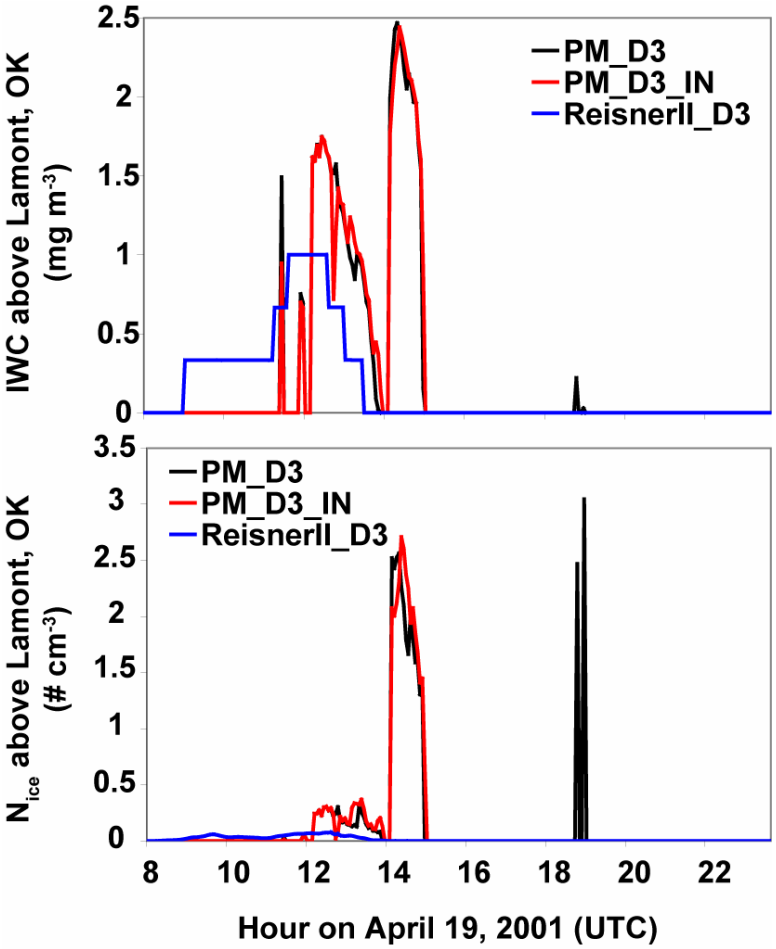

Figure 4.18. Model cirrus 12 km above Lamont, OK. Compared to the observations (Figure 4.2), both the parcel model (PM_D3, PM_D3_IN) and the Reisner II scheme (ResinerII_D3) underestimated cirrus presence 12 km above Lamont, OK on April 19, 2001.

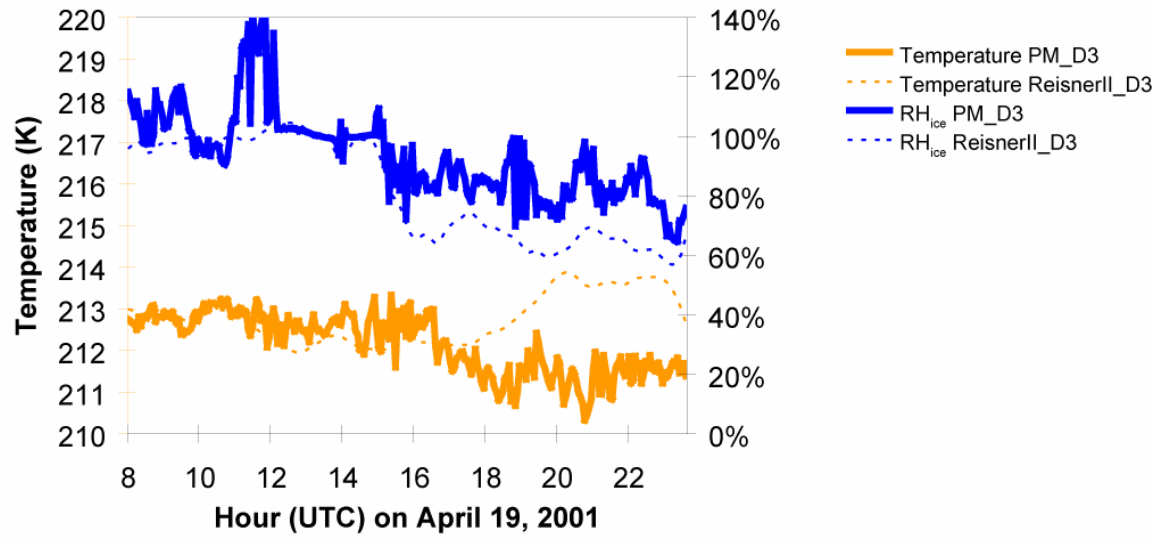

Figure 4.19: Model humidity and temperature 12 km above Lamont, OK. In both the parcel model (PM_D3) and the Reisner II scheme (ReisnerII_D3), the air at cirrus levels above Lamont, OK was sub-saturated with respect to ice.

A lack of moisture along trajectories upwind of Lamont, OK could explain the differing cirrus presence in the models and the observations. With additional moisture, the modeled RH_{ice} could have remained near ice saturation and more modeled cirrus may have arrived at Lamont, OK. In addition, additional moisture and small scale lifting could have generated sufficient RH_{ice} to generate new freezing events.

We suggest the MM5 moisture deficit could have resulted from a lack of warm frontal lifting. The reduced southern extent of Montana low in the MM5 forecast as compared to the NWS reanalysis supports the hypothesis that a lack of warm frontal lifting may have contributed to the lack of modeled cirrus above Lamont, OK. Even with increasing temperatures, mixing along the MM5 trajectories could have increased the total water, maintained high RH_{ice}, and increased model cirrus over Lamont, OK. The MM5 total water along trajectories upwind of Lamont, OK, however, demonstrated little limited evidence for mixing in of new water (Figure 4.20). Total water content differences between the MM5, which in principle contains mixing, and the parcel model, which lacks mixing, were small and primarily related to differences in dehydration.

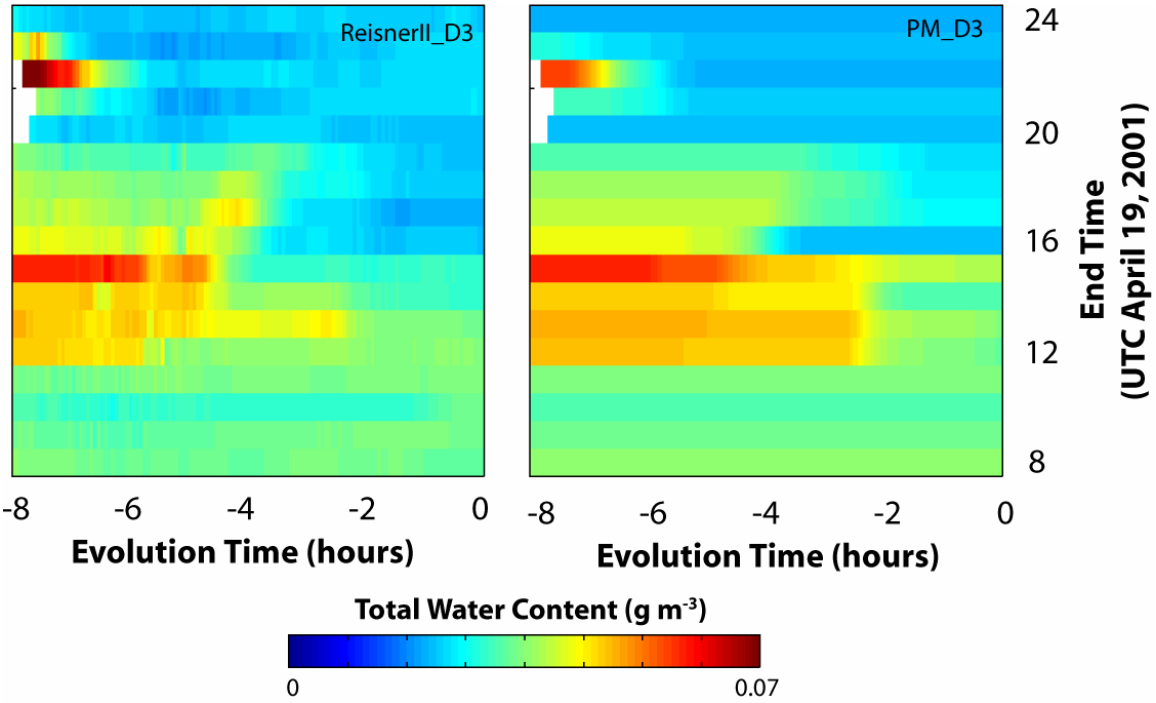

Figure 4.20: Model total water content along hourly trajectories. Total water content is plotted along trajectories ending every hour 12 km above Lamont, OK. Dehydration occurred coincident with fallout of cirrus ice crystals. No mixing of new water occurred along modeled trajectories.

Table 4.3: Cirrus properties above Lamont, OK. The range of cirrus N_{ice}, R_{eff} and σ are given from 8-24 UTC on April 19, 2001. IWC > 0.1 mg m^{-3}

Source	N_{ice} (# cm^{-3})	R_{eff} (μm)	σ
PM_D3	0.01 - 2.56	3 – 25	0.02 – 0.7[1]
PM_D3_IN	0.01 - 2.71	6 – 30	0.03 – 0.7[1]
PM_D3_Meyers	0.002 - 1.04	5 – 25	0.01 – 0.3[1]
Reisner II_D3	0.02 - 0.08	25-36	N/A
Lidar and AERI Observations	N/A	N/A	0 – 3 +

Despite obvious differences between the observed and modeled cirrus presence, modeled cirrus did form in the lee of the Rockies and were advected to Lamont, OK (Figures 4.12, 4.13, and 4.16). As a result, we were able to compare observed and modeled cirrus properties. We found that our parcel model reproduced the cirrus observations in two ways. First, assuming ice crystals above Lamont, OK formed in the lee of the Rockies, the observed broad P(σ) at Lamont, OK (Figure 4.3) could be partially explained by variable parcel model N_{ice} resulting from w^h

variability associated with the orographic gravity waves (Table 4.3). Second, large parcel N_{ice} resulted in long modeled cirrus lifetimes and could explain the observed persistence of cirrus over many hours in the GOES imagery. In contrast, the Reisner II cirrus arriving at Lamont, OK had a narrow distribution of cloud N_{ice}. Therefore, the Reisner II N_{ice} could not explain the observed σ variability and long cirrus lifetimes.

4.5. Summary and discussion

Using Lagrangian w trajectories derived from a mesoscale weather model and a parcel model with binned ice microphysics, this chapter highlights the influence of w and IN parameterization on cirrus N_{ice}, and inhomogeneity during an orographic cirrus case study. The primary findings were:

- Large N_{ice}, large σ, and long cirrus lifetimes resulted along upper tropospheric trajectories with large w^h (Figure 4.11, Figure 4.12). $P(N_{ice})$ and $P(\sigma)$ derived along trajectories with a range of w were broad (Figures 4.14).

- The addition of IN to parcels decreased the average σ, and increased the cloud fraction. Whereas background N_{IN} ($N_{IN} = 0.03$ cm^{-3}) presence had little influence on the occurrence of large σ, the presence of large N_{IN} ($N_{IN} > 0.3$ cm^{-3}), resulting from use of Meyers et al. (1992) parameterization, decreased the occurrence of large σ by suppressing homogeneous nucleation. In general, the Meyers et al (1992) parameterization produced more IN than are typically observed in the atmosphere ($N_{IN} <$ 0.1 cm^{-3} ((DeMott et al., 2003a), (Rogers et al.,1998)). Therefore, we concluded that our background N_{IN} modeling results are more likely to represent the influence of IN on cirrus in the atmosphere.

- The Reisner II parameterization did not include the feedback between w^h and N_{ice}. As a result, Reisner II cirrus had less variability in N_{ice}, and more uniform cloud histories when compared to the parcel model cirrus (Figure 4.16, Figure 4.17).

- All models had fewer cirrus than were observed at Lamont, OK because of a lack of moisture along MM5 trajectories. However, parcel model cirrus reproduced the observed cirrus in the following sense: 1) Broad P(σ) observed by the Lamont, OK lidar could be explained by variable N_{ice} arriving along parcel model cirrus trajectories (Table 4.3), 2) Larger N_{ice} resulted in long cirrus lifetimes and could explain the persistence of cirrus over many hours.

Although there are limitations associated with using an adiabatic parcel model and trajectories to represent cirrus, the results from this orographic cirrus case study demonstrate clear connections between w variability, N_{IN}, and cirrus inhomogeneity. In general, we found that calculating cloud property distributions along multiple trajectories was more informative than describing events along individual trajectories. Indeed, along individual cirrus evolution trajectories, the influence of w and IN on cirrus evolution were not always predictable or representative.

All of the models utilized in this study did a poor job reproducing the observed cirrus presence above Lamont, OK. A mesoscale model forecast is an initial value problem with a single realization. Therefore, we were not surprised to find deviations between the modeled and observed atmospheric dynamics and cirrus presence. We could have generated MM5 forecasts until we reproduced the observed cirrus presence at Lamont, OK. We do plan to further investigate the MM5 moisture deficit above Lamont, OK and to address the extent to which cirrus formation occurred in the lee of the Rockies or above Lamont, OK. However, our goal was not a detailed reproduction of the observations. Instead, our goal was to understand the physical processes that generate cirrus inhomogeneity. The observations were invaluable because they helped us identify April 19, 2001 as a good case study, not because they provided a benchmark for evaluating the ability of models to exactly reproduce observations. Using our parcel model, we accomplished our goal: we offered explanations for the observed inhomogeneity and evaluated the influence of w and IN on distributions of cloud properties.

Many bulk microphysical schemes, such as the Reisner II, were designed for precipitating clouds. As a result, they include a simplistic treatment of cirrus cloud processes. Yet, neglecting

cirrus processes can lead to inaccurate cirrus inhomogeneity and radiative fluxes. Therefore, the representation of cirrus processes in bulk microphysical schemes should be improved, especially as mesoscale weather forecasting models are starting to be used for regional climate modeling. Based on our results, we recommend that an explicit connection between w and N_{ice} should be included in all model microphysical schemes.

Given the limitations of using a parcel model to represent three-dimensional cirrus processes, and that this is only a single case study, the influence of w and IN on cirrus cloud properties should be explored further. There are interesting parallels between the w-N_{ice}-cloud lifetime-cloud cover connections described in this study and the indirect effects of aerosols on stratus albedos, lifetimes, and cloud cover (e.g., Twomey (1974), Albrecht (1989)). Understanding microphysical and dynamical controls on cirrus inhomogeneity should improve as model resolution increases and new observations are made.

Chapter 5:
SUMMARY AND CONCLUSIONS

In this dissertation, we used analytical approximations, parcel modeling along trajectories, and observations to address the following research question: How do physical processes affect cirrus inhomogeneity?. Throughout our research, we measured inhomogeneity using $P(\sigma)$. Cirrus $P(\sigma)$ determines the influence of cirrus on radiative fluxes and climate (see Chapter 1). In addition, assessing controls on $P(\sigma)$ shape provided a framework for relating physical processes to cirrus radiative impacts. Improving the physical basis for cirrus $P(\sigma)$ in climate models should help reduce uncertainties in CRF. In this final chapter, we review findings from K06 and each research chapter. We then discuss the most important conclusion from our work. We conclude by offering suggestions for future research based on our findings.

In Chapter 2 and K06, we evaluated the microphysical and dynamical controls on cirrus $P(\sigma)$ using analytical expressions and parcel model experiments along idealized trajectories. The main findings of Chapter 2 and K06 were:

- Along constant vertical velocity trajectories, cirrus $P(\sigma)$ shape depended on R, the ratio of τ_{fall} to τ_{growth}. With $R > 1$, cirrus had long lifetimes and $P(\sigma)$ peaked at large values ($\sigma > 1$). With $R < 1$, cirrus had short lifetimes and $P(\sigma)$ decreased monotonically.
- Within an atmospherically relevant range of N_{aer}, N_{IN}, temperatures, and vertical velocities (w), w was the most important control on R and $P(\sigma)$.
- With observed background N_{IN} ($N_{IN} < 0.1$ cm^{-3} ((DeMott et al., 2003a), (Rogers et al., 1998)) and scavenging, IN had little influence on cirrus optical depths. IN never prevented homogeneous nucleation and IN influenced $P(\sigma)$ shape only when $R > 1$.
- Temperature oscillations influenced $P(\sigma)$ when $\tau_{growth} < \tau_{wave} < \tau_{fallout}$, or when τ_{wave} approached or exceeded $\tau_{reezing}$. When $R > 1$, mesoscale waves with appreciable ΔT (e.g., $\Delta T = 2$ K in our experiments) broadened $P(\sigma)$.
- When surface resistance to growth (i.e., $\alpha_{ice} << 0.1$) was included in our parcel model experiments, N_{ice} and the sensitivity of N_{ice} to N_{aer} increased dramatically. We were intrigued by these results given recent laboratory measurements that found $\alpha_{ice}=0.006$

(Magee et al., 2006). However, atmospheric observations from the INCA field campaign revealed little dependence of N_{ice} on N_{aer} (Kärcher and Strom, 2003) and are therefore inconsistent with $\alpha_{ice} << 0.1$. Based on the INCA observations and our parcel modeling experiments, we suggest $\alpha_{ice} > 0.1$ in the atmosphere.

In Chapter 3, we contributed new observational analyses and OLR bias calculations to a pre-existing Lamont, OK cirrus climatology. Then, by combining observations and simple modeling with a simple physical picture for cloud formation, we described the main controls on cirrus inhomogeneity. The main findings of Chapter 3 were:

- Using 766 $P(\sigma)$ calculated over 3-hour periods, we found that neglecting observed cirrus optical depth inhomogeneity resulted in an average OLR underestimation of 4.9 Wm^{-2}. Most observed $P(\sigma)$ shapes were well fit by gamma distributions with $\overline{\sigma}$ and ν derived from observations. As a result, using gamma distributions to represent observed cirrus $P(\sigma)$ reduced our average calculated OLR bias to -0.2 ± 0.8 Wm^{-2}. However, even with the use of a gamma distribution, a large OLR bias of 3.1 Wm^{-2} resulted from an anvil cirrus $P(\sigma)$ with a bi-modal $P(\sigma)$ shape. Although bi-modal $P(\sigma)$ shapes were not common in our observations, the identified anvil cirrus $P(\sigma)$ misfit is concerning given the radiative importance of anvil cirrus in the Tropics.
- Most cirrus occurred at temperatures less than -40 °C, were optically thin ($\sigma < 0.5$), and had monotonically decreasing $P(\sigma)$ shapes. Most observed σ and $P(\sigma)$ were consistent with small R.
- The observed dominance of small optical depths and monotonically decreasing $P(\sigma)$ shapes was due to the observed N_{ice} and Δz distributions, which were both dominated by small values.
- The mean M01 N_{ice}=0.1 cm^{-3} could be not be explained by observed background N_{IN} (N_{IN} < 0.1 cm^{-3} ((DeMott et al., 2003a); (Rogers et al., 1998)). Using parcel modeling, we demonstrated that homogeneous nucleation at w =7-11 cm sec^{-1} could explain the M01 mean observed N_{ice}. Plausible mesoscale w (100-1000s m) could exceed 7-11 cm sec^{-1}, while observed synoptic w rarely approached 7-11 cm sec^{-1}.

- Estimated sublimation timescales below cloud (τ_{sub}) were uniformly short (τ_{sub} < 20 minutes) for typical crystal sizes (R_{eff}=35 μm). Therefore, observed cirrus Δz was primarily controlled by the depth and temperature of thin saturated layers.
- Combining the physical controls on N_{ice} and Δz, we concluded that observed P(σ) variability could result from homogeneous nucleation alone, variability in mesoscale w, and variability in the depth and temperature of thin saturated layers.

In Chapter 4, we modeled cirrus along Lagrangian trajectories derived from a mesoscale weather model (MM5). Our goal was to assess the influence of w and IN on cirrus P(N_{ice}) and P(σ) along cirrus evolution pathways. We focused our analysis on an orographic cirrus case study during which cirrus formed over the Rockies and were advected to Lamont, OK. The main findings of Chapter 4 were:

- By calculating distributions of cirrus properties along multiple upper tropospheric trajectories using the K06 parcel model, we found: 1) Large N_{ice}, broad P(σ), and long cirrus lifetimes resulted along trajectories with large w during homogeneous nucleation. 2) The addition of IN to parcels resulted in a decrease in the average N_{ice} and optical depth, and an increase in the cloud fraction. Whereas background N_{IN} (N_{IN} = 0.03 cm^{-3}) had little influence on the occurrence of large N_{ice} and optical depths, the presence of large N_{IN} (N_{IN} > 0.3 cm^{-3}), resulting from use of Meyers et al. (1992) parameterization, decreased the occurrence of large N_{ice} and optical depths by suppressing homogeneous nucleation. In general, the Meyers et al (1992) parameterization produced more IN than are typically observed in the atmosphere (N_{IN} < 0.1 cm^{-3} ((DeMott et al., 2003a), (Rogers et al.,1998)). Therefore, we concluded that our background N_{IN} modeling results are more likely to represent the influence of IN on cirrus in the atmosphere.
- Cirrus produced by a standard bulk microphysical scheme used in MM5, the Reisner II scheme (Reisner et al., 1998), lacked a connection between N_{ice} and w. As a result, the cirrus generated by the Reisner II scheme had more uniform cloud properties and histories than the parcel model cirrus and observed cirrus.
- Both the parcel model and the cirrus generated by the Reisner II scheme did not reproduce the observed cirrus presence at Lamont, OK. We suggest that this failure resulted primarily from a lack of moisture. Nevertheless, we found that variability in

parcel model cirrus cloud properties above Lamont, OK could help explain the broad observed P(σ).

The most significant finding from our research was: Cirrus P(σ) were more sensitive to plausible variations in dynamic forcing than to plausible variations in aerosol forcing. With α_{ice}, N_{aer}, N_{IN}, and w ranges constrained atmospheric observations, cirrus P(σ) in our parcel model depended primarily on the w during homogeneous nucleation. We determined that the w required to generate observed N_{ice} could come from plausible mesoscale w. From the observations and simple modeling, we also demonstrated that the observed Δz was primarily controlled by thin saturated layers, not sub-cloud processes.

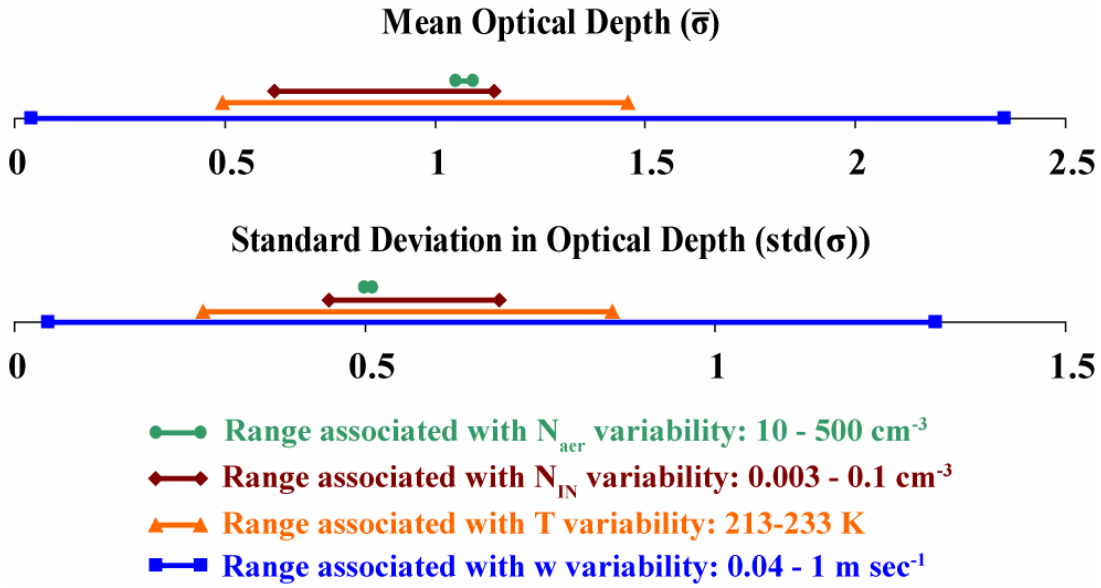

Figure 5.1: The sensitivity of cirrus optical depth to plausible variations in aerosol number concentration, ice nuclei number concentration, temperature, and vertical velocity. For each unique set of parameters, we lifted a parcel 1000 m starting at RH_{ice}=100% at a constant w and recorded the in-cloud mean σ and std(σ). For each parameter (N_{aer}, N_{IN}, T, and w), we stepped through the full range of parameter values and calculated the average mean σ and std(σ) over all runs holding the parameter value constant. The plotted range in average mean σ and std(σ) indicates the sensitivity of cirrus σ to plausible variations in each parameter. As in K06, α=1.

Aerosols had little influence on N_{ice} and $P(\sigma)$. Modeled cirrus N_{ice} and $P(\sigma)$ were not sensitive to N_{aer} except with low $\alpha_{ice.}$ Our parcel modeling revealed that low α_{ice} was not consistent with atmospheric observations (Kärcher and Strom, 2003). With parcel modeling constrained by observed N_{IN}, we found that heterogeneous nucleation had little influence on mean optical depths. Heterogeneous nucleation with observed N_{IN} could not explain most cirrus N_{ice} observations. Although exotic heterogeneous nucleation mechanisms may exist, homogeneous nucleation occurring at a range of w could explain observed cirrus N_{ice}.

Cirrus inhomogeneity is important for calculating radiative fluxes and climate feedbacks in large scale models. Because we found that most cirrus properties can be largely explained by homogeneous nucleation alone and that N_{ice} is relatively insensitive to N_{aer}, we suggest that aerosols are not important for many calculations of cirrus $P(\sigma)$ radiative impacts.

We conclude this dissertation by suggesting directions for future research based on our findings:

- Parcel modeling and the observed sensitivity of N_{ice} to N_{aer} could be used to place additional constraints on α_{ice} values in the atmosphere. In addition, the use of a parcel model with an aerosol size distribution could be used to assess the sensitivity of N_{ice} to aerosols with low $\alpha_{ice.}$
- Research addressing the interesting parallels and lack of parallels between the microphysical processes occurring in warm and cold clouds could be fruitful. For example, future work could identify the extent to which the impact of N_{aer} variability on stratus droplet number concentrations, $P(\sigma)$, and cloud cover (e.g., Twomey (1974), Albrecht (1989)) is similar to the impact of w on cirrus N_{ice}, $P(\sigma)$, and cloud cover.
- The w-$P(\sigma)$-cloud lifetime connections described in this work merit additional research. Many of our findings were based on a zero-dimensional parcel model and a simple cirrus conceptual model. Calculating R and $P(\sigma)$ with a more sophisticated model would be a useful test of our findings.
- New observations are required to test the findings of this study and to address long-standing uncertainties in model initial conditions and dynamical forcing. In particular, high accuracy and resolution measurements of upper tropospheric RH_{ice} (accuracy ± %5,

spatial resolution 100 m) and mesoscale w (accuracy ± 1 cm sec^{-1}, spatial resolution 100 m) are needed. With new RH_{ice} and w measurements, future researchers could address remaining uncertainties regarding the extent to which heterogeneous nucleation is required to explain cirrus formation and presence.

REFERENCES

Albrecht, B. (1989), Aerosols, cloud microphysics and fractional cloudiness, *Science*, 245, 1227-1330.

Barker, H. W. (1996), A parameterization for computing grid-averaged solar fluxes for inhomogeneous marine boundary layer clouds .1. Methodology and homogeneous biases, *Journal of the Atmospheric Sciences*, 53 (16): 2289-2303.

Beaver M. R., M. J. Elrod, R. M. Garland and M. A. Tolbert (2006), Ice nucleation in sulfuric acid/organic aerosols: implications for cirrus cloud formation, *Atmospheric Chemistry and Physics*, 6, 3231-3242.

Beesley, J.A., C. S.Bretherton, C. Jakob, E. L. Andreas, J. M Intrieri, and T. A. Uttal (2000), A comparison of cloud and boundary layer variables in the ECMWF forecast model with observations at Surface Heat Budget of the Arctic Ocean (SHEBA) ice camp, *Journal of Geophysical Research*, 105 (D10): 12337-12349.

Boville, B. A., P. J. Rasch, J. J. Hack, and J. R. McCaa (2006), Representation of clouds and precipitation processes in the community atmosphere model version 3 (CAM3), *Journal of Climate*, 19, 2184-2195.

Boville, B.A., J. T. Kiehl, P. J. Rasch and F. O. Bryan (2001), Improvements to the NCAR CSM-1 for transient climate simulations. *Journal of Climate*, 14, 164-179.

Carlin, B., Q. Fu, U. Lohmann, G. Mace, K. Sassen, and J. Comstock (2002), High-cloud horizontal inhomogeneity and solar albedo bias, *Journal of Climate*, 15 (17), 2321-2339.

Chabouureau, J-P., and P. Bechtold (2002), A simple cloud parameterization derived from cloud resolving model data: diagnostic and prognostic applications, *Journal of the Atmospheric Sciences*, 59, 2362-2372.

Chen, T., W. B. Rossow, and Y. Zhang (2000), Radiative effects of cloud-type variations, *Journal of Climate*, 13, 264-286.

Comstock, J. M., T. P. Ackerman, and D. D. Turner (2004), Evidence of high ice supersaturation in cirrus clouds using ARM Raman lidar measurements, *Geophysical Research Letters*, 31.

Davis A., A. Marshak, R. Cahalan, and W. Wiscombe (1997), The Landsat scale break in stratocumulus as a three-dimensional radiative transfer effect: implications for cloud remote sensing, *Journal of the Atmospheric Sciences*, 54, 2, 241-260.

Dean, S. M., B. N. Lawrence, R. G. Grainger, and D. N. Heuff (2005), Orographic cloud in GCM: the missing cirrus, *Climate Dynamics*, 24, 771-780.

Delgenio, A. D., M. Yao, W. Kovari, and K. K-W. Lo (1996), A prognostic cloud water

parameterization for global climate models, *Journal of Climate*, 9, 270-304.

Delworth T. L., A. J. Broccoli, A. Rosati, R. J. Stouffer, V. Balaji, J. A. Beesley, W. F. Cooke, K.W. Dixon, J. Dunne, K.A. Dunne, J. W. Durachta, K. L. Findell, P. Ginoux, A. Gnanadesikan, C. T. Gordon, S. M. Griffies, R. Gudgel, M. J. Harrison, I. M. Held, R. S. Hemler, L. W. Horowitz, S. A. Klein, T. R. Knutson, P. J. Kushner, A. R. Langenhorst, H. C. Lee, S. J. Lin, J. Lu, S. L. Malyshev, P. C. D. Milly, V. Ramaswamy, J. Russell, M. D. Schwarzkopf, E. Shevliakova, J. J. Sirutis, M. J. Spelman, W. F. Stern, M. Winton, A. T. Wittenberg, B. Wyman, F. Zeng and R. Zhang (2006), GFDL's CM2 global coupled climate models. Part I: Formulation and simulation characteristics, *Journal of Climate,* 19 (5): 643-674.

DeMott, P. J., D. J. Cziczo, A. J. Prenni, D. M. Murphy, S. M. Kreidenweis, D. S. Thomson, R. Borys, and D. C. Rogers (2003a), Measurements of the concentration and composition of nuclei for cirrus formation, *Proceedings of the National Academy of Sciences*, 100:25, 14655-14660.

DeMott, P. J., K. Sassen, M. R. Poellot, D. Baumgardner, D.C. Rogers, S. D. Brooks, J. Prenni, and S. M. Kreidenweis (2003b), African dust aerosols as atmospheric ice nuclei, *Geophysical. Research Letters*, 30-14, 1732.

DeMott, P. J., D. C. Rogers, and S. M. Kreidenweis (1997), The susceptibility of ice formation in upper tropospheric clouds to insoluble aerosol components, *Journal of Geophysical Research*, 102 (D16), 19575-19584.

Demoz B. B., D. O. Starr, K. R. Chan, and S. W. Bowen (1998), Wavelet analysis of dynamical processes in cirrus, *Geophysical Research Letters.*, 25 (9), 1347-1350.

Durant, A. J., and R. A. Shaw (2005), Evaporation freezing by contact nucleation inside-out. *Geophysical Research Letters*, 32, L20814, doi:10.1029/2005GL024175.

Durran, D. R. (2003), Lee Waves and Mountain Waves in Encyclopedia of Atmospheric Science, Ed. J. Holton, J. Pyle, and J. Curry, Academic Press.

Field, P. R., R. J. Cotton, N. Noone, P. Glantz, P. H. Kaye, E. Hirst, R. S. Greenaway, C. Jost, R. Gabriel, T. Reiner, M. Andreae, C. P. R. Saunders, A. Archer, T. Choularton, M. Smith, B. Brooks, C. Hoell, B. Bandy, D. Johnson, and A. Heymsfield (2001), Ice nucleation in orographic wave clouds: Measurements made during INTACC, *Quat. Jour. Roy. Meteor. Soc.*, 127, 575, 1493-1512.

Fu, Q., M. Baker, and D. Hartmann (2002), Tropical cirrus and water vapor: an effective Earth infrared iris feedback?, *Atmospheric Chemistry and Physics*, 2 , 31-37.

Fu, Q., B. Carlin, and G. Mace (2000), Cirrus horizontal inhomogeneity and OLR bias, *Geophysical Research Letters*, 27 (20), 3341-3344.

Fu, Q., and K. N. Liou (1993), Parameterization of the radiative properties of cirrus clouds,

Journal of the Atmospheric Sciences, 50, 2008-2025.

Fowler, L. D., Randell, D. A., and S. A. Rutledge (1996), Liquid and ice cloud microphysics in the CSU general circulation model. Part I: Model description and simulated microphysical processes, *Journal of Climate*, 9, 489-529.

Garrett, T. J., H. Gerber, D. G. Baumgardner, D. G., C. H. Twohy, and E. M. Weinstock (2003), Small, highly reflective ice crystals in low-latitude cirrus, *Geophysical Research Letters*, 30, 2132, doi:10.1029/2003GL018153.

Gavish G., R. Popovitz-Biro, M. Lahav, and L Leiserowitz (1990), Ice nucleation by alcohols arranged in monolayers at the surface of water drops, *Science*, 250, 4923, 973-975.

Gierens, K. M., M. Monier, and J. Gayet (2003), The deposition coefficient and its role for cirrus clouds, *Journal of Geophysical Research*, 108 (D2).

Goff, J. A., and S. Gratch (1946) Low-pressure properties of water from -160 to 212 F, in Transactions of the American society of heating and ventilating engineers, pp 95-122, presented at the 52nd annual meeting of the American society of heating and ventilating engineers, New York.

Goldsmith, J. E. M., F. H. Blair, S. E. Bisson, and D. D. Turner (1998), Turn-key Raman lidar for profiling atmospheric water vapor, clouds and aerosols, *Applied Optics*, 37, 4979-4990.

Gordon, C., C. Cooper, C.A. Senior, H. T. Banks, J. M. Gregory, T. C. Johns, J. F. B. Mitchell and R. A. Wood (2000), The simulation of SST, sea ice extents and ocean heat transports in a version of the Hadley Centre coupled model without flux adjustments, *Climate Dynamics*, 16, 147-168.

Gu, Y. and K. N. Liou (2006), Cirrus cloud horizontal and vertical inhomogeneity effects in a GCM, *Meteorology and Atmospheric Physics*, 91, 223-235.

Gu, Y. and K. N. Liou (2000), Interactions of radiation, microphysics, and turbulence in the evolution of cirrus clouds, *Journal of the Atmospheric Sciences* 57 (15), 2463-2479.

Haag, W. and B. Kärcher (2004), The impact of aerosols and gravity waves on cirrus clouds at mid-latitudes, *Journal of Geophysical Research*, 109 (D12), doi:10.1029/2004JD004579.

Hall, D. P., and H. R. Pruppacher (1976), The survival of ice particles falling from cirrus clouds in subsaturated air, *Journal of the Atmospheric Sciences*, 33, 1995-2006.

Hartmann, D. L., M. E. Ockert-Bell, and M. L. Michelsen (1992), The effect of cloud type on Earth's energy balance: global analysis, *Journal of Climate*, 5, 1281-1304.

Haynes, D. R., N. J. Tro, and S. M. George (1992), Condensation and evaporation of H20 on ice surfaces, *Journal of Physical Chemistry*, 96, 8502-8509.

Heymsfield, A. J., and L. J. Donner (1990), A scheme for parameterizing ice-cloud water content in general circulation models, *Journal of the Atmospheric Sciences*, 47 (15), 1865-1877.

Heymsfield, A. J. and L. M. Milosovich (1995), Relative humidity and temperature influences on cirrus formation and evolution: observations from wave clouds and FIRE II, *Journal of the Atmospheric Sciences.*, 52, 23, 1995.

Houghton, J. T., Y. Ding, D. J. Griggs, M. Noguer, P. J. Van der Linden, and D. Xiaosu (Eds.) (2001), Climate Change 2001: The Scientific Basis Contribution of Working Group I to the Third Assessment Report of the Intergovernmental Panel on Climate Change (IPCC), Cambridge University Press, UK.

Hoyle, C. R., B. P. Luo, and T. Peter (2005), The origin of high ice crystal number densities in cirrus clouds, *Journal of the Atmospheric Sciences*, 62, 2568-2579.

Jensen, E. J. and O. B. Toon (1994), Ice freezing in the upper troposphere: sensitivity to aerosol number density, temperature and cooling rate, *Geophysical Research Letters*, 21 (18), 2019-2022.

Jensen, E. J., O. B. Toon, S. A. Vay, J. Ovarlez, R. May, T. P. Bui, C. H. Twohy, B. W. Gandrud, R. F. Pueschel, and U. Schumann (2001), Prevalence of ice-supersaturated regions in the upper troposphere: Implications for optically thin ice cloud formation, *Journal of Geophysical Research,* 106 (15), 17253-17266.

Kay, J., M. Baker, and D. Hegg (in press), Microphysical and dynamical controls on cirrus cloud optical depth distributions, *Journal of Geophysical Research.*

Kärcher, B. and U. Lohmann (2002), A parameterization of cirrus cloud formation: Homogeneous freezing of supercooled aerosols, *Journal of Geophysical Research*, 107 (D2), doi:10.1029/2002JD003220.

Kärcher, B. and U. Lohmann (2003), A parameterization of cirrus cloud formation: heterogeneous freezing, *Journal of Geophysical Research*, 108 (D14), doi:10.1029/2002JD003220.

Kärcher, B. and J. Strom (2003), The roles of dynamical variability and aerosols in cirrus cloud formation, *Atmospheric Chemistry and Physics*, 3, 823-838.

Koop, T., B. Luo, A. Tslas, and T. Peter (2000), Water activity as the determinant for homogeneous ice nucleation in aqueous solutions, *Nature*, 406, 611-614.

Lin, R.-F., D. O. O'Starr, J. Reichardt, and P. J. DeMott (2005), Nucleation in synoptically forced cirrustratus, *Journal of Geophysical Research.*, 110, D08208, doi:10.1029/2004D005362.

Lin, R.-F., D. O. O'Starr, P. J. DeMott, , R. Cotton, K. Sassen, E. Jensen, B. Kärcher, and

X. Liu (2002), Cirrus parcel model comparison project. Phase 1: The critical components to simulate cirrus initiation explicitly, *Journal of the Atmospheric Sciences*, 59 (15), 2305-2329.

Lohmann, U. and E. Roecker (1996), Design and performance of a new cloud microphysics scheme developed for the ECHAM general circulation model, *Climate Dynamics*, 12, 557-572.

Lynch, D. K., K. Sassen, D. O'C.Starr, and G. Stephens Editors (2002), *Cirrus*, Oxford University Press, New York, New York.

Mace, G. G., T. P. Ackerman, P. Minnis and D. F. Young (1998a). Cirrus layer microphysical properties from surface-based millimeter radar and infrared interferometer data, *Journal of Geophysical Research*, 103:18, 23207-23216.

Mace, G. G., K. Sassen, S. Kinne, and T. P. Ackerman (1998b) An examination of cirrus cloud characteristics using data from millimeter wave radar and lidar: The 24 April SUCCESS case study, *Geophysical Research Letters*, 25:8, 1133-1136.

Mace, G. G., E. E. Clothiaux, and T. P. Ackerman (2001), The composite characteristics of cirrus clouds: bulk properties revealed by one year of continuous cloud radar data, *Journal of Climate*, 14, 2185-2203.

Mace, G. G., S. Bensen, and E. Vernon (2006), Cirrus Clouds and the Large-Scale Atmospheric State: Relationships Revealed by Six Years of Ground-Based Data , *Journal of Climate,* 19 (13): 3257-3278.

Magee, N., A. M. Moyle, and D. Lamb (2006), Experimental determination of the deposition coefficient of small cirrus-like ice crystals near −50°C, *Geophysical Research Letters*, 33 (L17813), doi:10.1029/2006GL026665.

Manabe, S., R.J. Stouffer, M. J. Spelman and K. Bryan (1991), Transient responses of a coupled ocean-atmosphere model to gradual changes of atmospheric CO_2. Part I: Annual mean response. *Journal of Climate*, 4, 785-818.

Manabe, S. J. and R.J. Stouffer (1996), Low-frequency variability of surface air temperature in a 1000-year integration of a coupled atmosphere-ocean-land model. *Journal of Climate*, 9, 376-393.

Minikin, A., A. Petzold , J. Strom, R. Krejci, M. Seifert, P. van Velthoven, H. Schlayer, and U. Schumann (2003), Aircraft observations of the upper tropospherice fine particle aerosol in the Northern and Southern Hemispheres at mid latitudes, *Geophysical Research Letters*, 30 (10), doi:10.1029/2002GL016458.

Meyers et al., P. J., DeMott, P. J., and W. R. Cotton (1992), New primary ice-nucleation parameterization in an explicit cloud model, *Journal of Applied Meteorology*, 55, 2039-2052.

Murphy, D. M. and T. Koop (2005), Review of the vapor presser of ice and supercooled water for atmospheric applications, *Q. J. R. Meteorol. Soc.*, 131 (608), 1539-1565.

O'C. Starr, and D. P. Wylie (1990), The October 1986 FIRE Cirrus Case Study: Meteorology and Clouds, *Monthly Weather Review*, 118, 2259-2287.

O' C. Starr, D. and S. K. Cox (1985), Cirrus Clouds Part II: Numerical experiments on the formation and maintenance of cirrus, *Journal of the Atmospheric Sciences*, 42:23, 2682-2694.

Ovarlez, J., J-F Gayet, K. Gierens, J. Strom, H. Ovarlez, F. Auriol, R. Busen and U. Schumann (2002), Water vapour measurements inside cirrus clouds in Northern and Southern hemispheres during INCA, *Geophysical Research Letters*, 29(16), 1813, 10.1029/2001GL014440.

Peter,T., M. Baker, P. Spichtinger, C. Marcolli, T. Corti, and T. Koop, The high supersaturation puzzle, in preparation for Nature.

Pope, V. D., M. Gallani, P. R. Rowntree and R. A. Stratton (2000), The impact of new physical parameterizations in the Hadley Centre climate model - HadAM3. *Climate Dynamics*, 16, 123-146.

Pruppacher, H. R. and J. D. Klett (1997), *Microphysics of Clouds and Precipitation*, Kluwer Academic Publishers, Boston.

Rasch, P. J., and J. E. Kristjansson (1998), A comparison of the CCM3 model climate using diagnosed and predicted condensate parameterizations, *Journal of Climate*, 11, 1587-1614.

Reisner, J., Rasmussne, R. M., and R. T. Bruintjes (1998), Explicit forecasting of supercooled liquid water in winter storms using the MM5 mesoscale model, *Quat. Jour. Roy. Meteor. Soc.*, 124,1071-1107.

Roeckner, E., G. Bäuml, L. Bonaventura, R. Brokopf, M. Esch, M. Giorgetta, S. Hagemann, I. Kirchner, L. Kornblueh, E. Manzini, A. Rhodin, U. Schlese, U. Schulzweida, and A. Tompkins (2003), The atmospheric general circulation model ECHAM5. Part I: Model description. Max Planck Institute for Meteorology Rep. 349, 127 pp. [available from MPI for Meteorology, Bundesstr. 53, 20146 Hamburg, Germany]

Rogers, D. C., P. J. DeMott, S. M. Kredenweis, and Y. Chen (1998), Measurements of ice nucleating aerosols during SUCCESS, *Geophysical Research Letters*, 25:9, 1383-1386.

Russell, G.L., J.R. Miller and D. Rind (1995), A coupled atmosphere-ocean model for transient climate change studies. *Atmosphere-Ocean*, 33, 683-730.

Sassen K. (1991), The polarization lidar technique for cloud research, a review and current assessment, *Bulletin of the American Meteorological Society*, 72, 12, 1848-1866.

Schmidt, G. A, R. Ruedy, J. E. Hansen, I. Aleinov, N. Bell, M. Bauer, S. Bauer, B. Cairns, V. Canuto, Y. Cheng, A. DelGenio, G. Faluvegi, A. D. Friend, T. M. Hall, Y. Hu, M. Kelley, N. Y. Kiang, D. Koch, A. A. Lacis, J. Lerner, K. K. Lo, R. L. Miller, L. Nazarenko, V. Oinas, J. Perlwitz, J. Perlwitz, D. Rind, A. Romanou, G. L. Russell, M. Sato, D. T. Shindell, P. H. Stone, S. Sun, N. Tausnev, D. Thresher, M. Yao (2005), Present day atmospheric simulations using GISS ModelE: Comparison to in-situ, satellite and reanalysis data, *Journal of Climate*, 19, 153-192.

Seeley, L. H., and G. T. Seidler (2001), Two-dimensional nucleation of ice from supercooled water, *Physical Review Letters*, 87, 5, 1-4.

Soden, B. J. and I. M. Held (2006), An assessment of climate feedbacks in coupled ocean-atmosphere models, *Journal of Climate*, 19, 3554-3360.

Smith, S. A. and A. D. DelGenio (2001), Analysis of Aircraft, Radiosonde, and Radar Observations in Cirrus Clouds Observed during FIRE II: The interactions between Environmental Structure, Turbulence, and Cloud Microphysical Properties, *Journal of the Atmospheric Sciences*, 451-461.

Sundqvist, H., E. Berge, J. E. Kristjansson (1989), Condensation and cloud parameterization studies with a mesoscale numerical weather prediction model, *Monthly Weather Review*, 117 (8): 1641-1657.

Turner, D. D. (2005), Arctic mixed-phase cloud properties from AERI lidar observations: Algorithm and results from SHEBA, Journal of Applied Meteorology, 44 (4): 427-444.

Twomey, S. A. (1974), Pollution and the planetary albedo, *Atmospheric Environment*, 8, 1251-1256.

Wang Z and K. Sassen (2002), Cirrus cloud microphysical property retrieval using lidar and radar measurements. Part II: Midlatitude cirrus microphysical and radiative properties, *Journal of the Atmospheric Sciences*, 59 (14): 2291-2302, 2002.

Zobrist B., C. Marcolli, T. Koop, B.P. Luo, D.M. Murphy, U. Lohmann, A. A. Zardini, U.K. Krieger, T. Corti, D. J. Cziczo, S. Fueglistaler, P. K. Hudson, D.S. Thomson and T. Peter (2006), Oxalic acid as a heterogeneous ice nucleus in the upper troposphere and its indirect aerosol effect, *Atmospheric Chemistry and Physics*, 6: 3115-3129.

Zuberi, B., A. K. Bertram, T. Koop, L. T. Molina, and M. J. Molina (2001), Heterogeneous freezing of aqueous particles induced by crystallized $(NH_4)_2SO_4$ Ice and Letovicite, *Journal of Physical Chemistry A*, 105, 6458-6464.

APPENDIX A: KAY ET AL. (IN PRESS)

Abstract

We assess microphysical and dynamical controls on cirrus cloud optical depth distributions [P(σ)] along idealized air parcel trajectories. We find P(σ) shape depends primarily on the ratio of the ice crystal fallout timescale to timescales of other microphysical and dynamical processes. With homogeneous freezing only, two P(σ) regimes emerged. In the limited-fallout regime, relatively slow fallout allows complete depletion of the ice supersaturation and P(σ) has a peak at large optical depth values ($\sigma > 1$). In contrast, in the fallout-dominated regime, relatively rapid fallout results in persistent high ice supersaturation, multiple freezing events, and P(σ) has a monotonically decreasing shape dominated by small optical depth values. The addition of heterogeneous freezing alters the homogeneous freezing P(σ) shape only in the limited-fallout regime. Here, glaciated ice nuclei (IN) do not inhibit homogeneous freezing, but can change P(σ) by reducing the optical depth of the P(σ) peak and adding a monotonically decreasing tail at low optical depth values. Surprisingly, glaciated IN do not significantly change P(σ) values or shape in the fallout-dominated regime. Fluctuations in vertical velocity and accompanying temperature changes have relatively little impact on P(σ) unless the fluctuation timescales are shorter than fallout timescales, but longer than ice crystal growth timescales. As temperature fluctuations increase in amplitude, new freezing events affect P(σ) as long as fluctuation timescales approach or exceed freezing timescales. Our modeled P(σ) qualitatively resemble observed P(σ), indicating these results could aid in GCM cirrus P(σ) parameterization and help diagnose the controls on cirrus P(σ).

1. Introduction

Research interest in cirrus clouds results from their importance for radiative transfer in the atmosphere. The sign and magnitude of cirrus radiative forcing depends on cloud altitude and the cirrus optical depth (σ [dimensionless]) which is a function of the effective ice crystal radius (R_{eff} [m]), and the number concentration of ice crystals (N_{ice} [m^{-3}]) (Fu and Liou, 1993). Not surprisingly, cirrus cloud inhomogeneity complicates calculation of the magnitude and the sign of cirrus radiative impacts. Cirrus cloud inhomogeneity can be represented by optical depth distribution functions ($P(\sigma)$), i.e., the fraction of optical depths occurring at a given optical depth. Climate and weather models use $P(\sigma)$ because they do not resolve cirrus processes at the smallest relevant scale, the radiative smoothing scale (~100 m (Smith and DelGenio, 2001)). The goal of our research is to understand the controls on cirrus $P(\sigma)$ by considering the complex interactions between microphysical processes and upper tropospheric dynamics. The audience for our research is climate modelers who want to develop physically based parameterizations of cirrus radiative impacts and members of the general climate community who are interested in the microphysical and dynamical controls on cirrus cloud radiative impacts.

Recent research highlights the sensitivity of radiative transfer calculations to cirrus $P(\sigma)$ (Fu et al. 2000; Carlin et al., 2002). In climate and weather models, $P(\sigma)$ is usually approximated as a gamma distribution whose two fit parameters ($\overline{\sigma}$,ν) are determined by the mean optical depth ($\overline{\sigma}$) and the standard deviation in optical depth [$std(\sigma)$] (Fu et al., 2000):

$$P(\sigma) = \frac{1}{\Gamma(\nu)}\left(\frac{\nu}{\overline{\sigma}}\right)^{\nu} \sigma^{\nu-1} \exp^{-\frac{\nu\sigma}{\overline{\sigma}}} \qquad (1)$$

where $\nu = \left(\frac{\overline{\sigma}}{std(\sigma)}\right)^2$ and $\Gamma(\nu)$ is the gamma function.

Though gamma distributions seem to describe many observations of cirrus variability, the microphysical and dynamical factors determining gamma distribution fit parameters remain unexplained. In addition, gamma distributions do not always capture observed $P(\sigma)$ shapes.

Figure 1 shows P(σ) observations and gamma distribution fits using observed $\overline{\sigma}$ and std(σ) from the Atmospheric Radiation Measurement (ARM) Raman lidar in Lamont, Oklahoma (36° N 97° W). Though the isolated cirrus and orographic ridge cirrus gamma distribution P(σ) adequately match the observed P(σ) shapes, the anvil cirrus gamma distribution P(σ) misses the observed P(σ) peak at high optical depth values.

Field campaigns and laboratory measurements provide constraints for modeling cirrus cloud processes and P(σ). High supersaturation with respect to ice (S_i [%]) (Jensen et al., 2001; Gierens et al, 2000), a range of vertical velocities (w [m sec^{-1}]) (Gultepe and Starr, 1995; Demoz et al., 1998), and variable aerosol and ice nuclei (IN) concentrations (DeMott et al., 2003; Rogers et al. 1998; Minikin et al. 2003) are observed in cirrus environments. Pioneering modeling studies explored processes determining N_{ice} and cirrus optical depths at upper tropospheric temperatures (T [K]) where both homogeneous and heterogeneous freezing can occur (T < 238 K). DeMott et. al. (1997) documented the importance of heterogeneous freezing at low w. Kärcher and Strom (2003) suggested that mesoscale variability in w in combination with homogeneous freezing account for most of the observed variance in N_{ice}. Hoyle et al. (2005) used aircraft observations and a parcel model to demonstrate that small-scale temperature fluctuations can result in large cooling rates, large homogeneous freezing rates, and large N_{ice}. Haag and Kärcher (2004) found that IN present at concentrations less than 0.03 cm^{-3}, especially those with freezing thresholds near ice saturation, modify cirrus properties but do not control cirrus formation. Despite these advances, there is still debate about the relative importance of aerosols and dynamics for cirrus evolution. One obvious reason this debate continues is that we lack observations of IN concentrations, IN glaciation functions, and upper tropospheric w. (Throughout this study, we use the term “glaciation function” to refer to the dependence of freezing rates on S_i and T.)

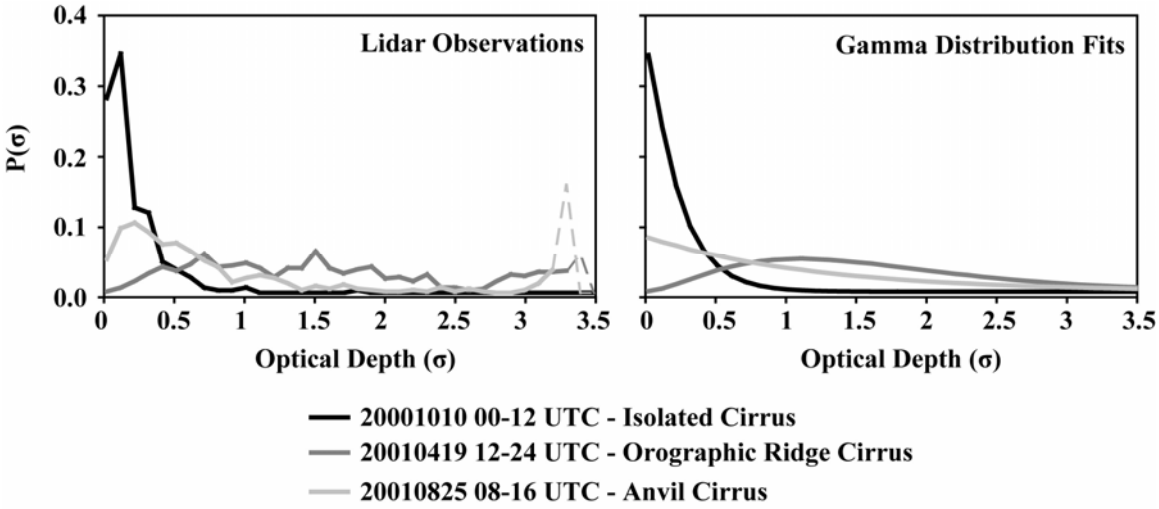

Figure 1: Observed P(σ) and gamma distribution fits from Lamont, OK (USA). Gamma distribution fits (Eq. 1) do a reasonable job of reproducing optical depth variability for the isolated and orographic ridge cirrus observations, although the anvil cirrus gamma distribution P(σ) misses a peak at large optical depths in the observed P(σ). The goal of this paper is to understand the dynamical and microphysical parameters controlling these P(σ). Notes about plotted P(σ): 1) All P(σ) are normalized. They are computed with an σ interval of 0.1. 2) P(σ) do not include clear sky. For radiative transfer calculations, both P(σ) and the cloud fraction are required. 3) The exact σ values and P(σ) shape are uncertain when the attenuation limit for the lidar was reached (indicated with dashed line). Here, P(σ) calculations assume attenuated observations were equivalent to the maximum observed σ, which is a lower limit on the real σ. Although P(σ) are more uncertain when dashed, variability in cloud depth, which is proportionally to σ, supports a peak at large σ for the anvil cirrus P(σ), and a broader P(σ) at large σ for the orographic ridge cirrus.

To incorporate existing and new cirrus observations into calculations of cirrus radiative impacts, we must understand how upper tropospheric dynamics and microphysical processes affect cirrus P(σ). In this paper, we find the primary controls on cirrus P(σ) in an adiabatic parcel model that includes freezing, growth, and fallout by simulating cirrus evolution along idealized trajectories consisting of uniform w ($\overline{w}$ [m sec^{-1}]) and w waves. We expand on the existing modeling literature by focusing specifically on P(σ) and including ice crystal fallout, which is neglected by many parcel modeling studies. We constrain our modeling with dynamical and aerosol observations from cirrus aircraft field campaigns and laboratory measurements. In the next section (section 2), we describe the formulation and validation of our parcel model and our modeling approach. In section 3, we present the impact of cirrus microphysics and dynamics on

cirrus evolution and P(σ) in our parcel model. Finally, in section 4, we state our modeling conclusions, compare parcel model P(σ) to observed P(σ), and discuss limitations of our research.

2. Methods

2.1 Parcel model description and validation

Following Lin et al. (2002), Kärcher (2003) and Jacobson (1999), we developed an adiabatic parcel model with explicit binned ice microphysics. The parcel model calculates the size and concentration of sulfuric acid aerosols, water drops, and ice crystals along prescribed trajectories using specified phase transition criteria and standard diffusion equations. The vapor pressures over ice and supercooled water are specified from a recent compilation by Murphy and Koop (2005). We use surface tension and density of aqueous sulfuric acid parameterizations from laboratory measurements by Myhre et al. (1998). Aerosol concentrations are set at 100 cm^{-3} based on aircraft observations in the upper troposphere (e.g., Rogers et. al., 1998). In agreement with published research (Jensen and Toon,1994; Kärcher and Strom, 2003), we find cirrus evolution is relatively insensitive to aerosol number concentration. We utilize homogeneous freezing rates (J_{hom} – cm^{-3} sec^{-1}) derived as functions of aerosol water activity following Koop et al. (2000) (hereafter Koop):

$$\log 10(J_{\hom}(a_w, T)) = -906.7 + 8502(a_w - a_w^{ice}(T)) - \ldots \\ 26924(a_w - a_w^{ice}(T))^2 + 29180(a_w - a_w^{ice}(T))^3 \quad (2)$$

where

$$a_w^{ice}(T) = \exp\left(\frac{210368 + 131.438T + \frac{-3.2373 * 10^{-6}}{T} + -41729.1\ln(T)}{8.31441T}\right),$$

a_w is the aerosol water activity and a_w^{ice} is the activity of water in a solution in equilibrium with ice.

Laboratory freezing experiments show agreement between the Koop parameterization and measured sulfuric acid particle freezing rates (Möhler et al. 2003). In our work, we assume a_w equals the relative humidity with respect to water (i.e., equilibrium).

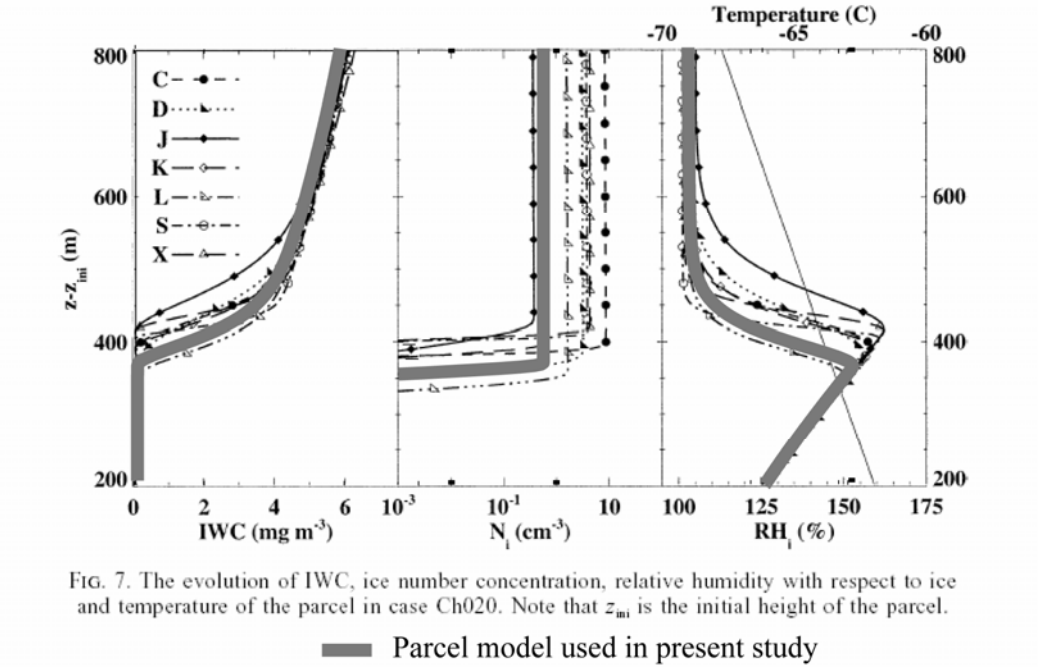

Figure 2: Evolution of IWC, N_{ice} and RH_{ice} from the parcel model developed for this study compared with Lin et al. (2002). Results from the parcel model developed for this study are within the range of parcel model results for an inter-comparison study completed by Lin et al. (2002).

To validate our parcel model, we compared it to seven published cirrus parcel models used in the Lin et al. (2002) cirrus parcel model inter-comparison study (Figure 2). Following Lin et al. (2002), we allowed only homogeneous freezing and neglected particle fallout for our comparisons. For parcel model simulation uc020_hom ($\overline{w}$=20 cm sec^{-1}, initial "cold" temperature T_o [K] = 213 K, initial pressure P_o = 17000 Pa and initial supersaturation with respect to ice S_{io} =0%), our model had a similar evolution of ice water content (IWC [mg kg^{-1}]) and is within the model spread for N_{ice} and the drawdown of S_i by diffusional growth. In the Lin et al. (2002) uc020_hom simulations, N_{ice} ranged from 0.3 cm^{-3} (model J - Jensen and Toon (1994)) to 8 cm^{-3} (model C - Spice et al. (1999)). Our uc020_hom model run predicted N_{ice} of

0.60 cm^{-3}, similar to the Kärcher model (model K – see Kärcher (2003)), which also used the Koop homogeneous freezing parameterization.

2.2 Parcel model additions: Heterogeneous freezing and fallout formulation

In addition to the standard ice microphysics used in the Lin et al. (2002) model comparison study, our parcel model includes both heterogeneous ice crystal freezing and fallout.

Traditionally, homogeneous and heterogeneous freezing have been distinguished by the number concentrations of aerosols available for freezing (i.e., hydrated aerosols with IN vs. hydrated aerosol without IN), and their glaciation functions. Therefore, our parcel model includes a range of IN concentrations and two contrasting glaciation functions. Guided by field observations, we varied IN concentrations in our parcel model from 0.003 cm^{-3} to 0.1 cm^{-3}. Atmospheric observations from Storm Peak, Colorado show IN concentrations are generally less than 0.03 cm^{-3} (DeMott et al., 2003). IN concentrations measured during SUCCESS flights in the Western USA ranged from 0.0001 to 0.5 cm^{-3}, with 60% of the observations between 0.002 and 0.02 cm^{-3} (Rogers et al.,1998). We selected two contrasting IN glaciation functions from published research: 1) a "burst" IN glaciation function following Kärcher and Lohmann (2003) (hereafter KL) and recent papers by Khvorostyanov and Curry (2004,2005). 2) a more gradual IN glaciation function following Meyers et al. (1992) and Lin et al. (2002) (hereafter M).

Heterogeneous freezing rates (J_{het} [cm^{-3} sec^{-1}]) for the KL "burst" IN glaciation function are based on a shifted water activity:

$$J_{het}(a_w, T) = \Delta * J_{\hom}(a_w + \delta a_w, T) \tag{3}$$

where $\delta a_w = [S_{cr}^{\hom} - S_{cr}^{het}]a_w^{ice} \approx 0.2 a_w^{ice}$ is the shifted water activity,

$S_{cr}^{\hom}(T) = 1.418 - \left(\frac{\mathrm{T}}{245.68}\right)$ is the critical ice supersaturation for homogeneous nucleation

, Δ is the ratio of the homogeneous and heterogeneous kinetic pre-factors (~30 nm), $S_{cr}^{\hom}$ is the

critical S_i for homogeneous freezing based on an aerosol size of 0.25 μm (~50% see Kärcher and Lohmann (2003)), and S_{cr}^{het} is the critical S_i for heterogeneous freezing.

When using the KL formulation, we set S_{cr}^{het}=30%. With the KL formulation, IN glaciate at rates similar to the Koop homogeneous freezing formulation (Eq. 2), but at a lower S_i (30 %) and with N_{ice} limited by the IN concentration.

The more gradual glaciation function, the M formulation, nucleates IN as an exponential function of S_i:

$$N_{IN-\max} = \exp(6.269 + 12.96(S_i)) \quad (4)$$

where $N_{IN\text{-}max}$ is the maximum number concentration of IN glaciated (m^{-3}).

Instead of specifying J_{het}, the M formulation determines the total IN nucleated as a function of the maximum parcel S_i. Developed for higher T and lower S_i, the M formulation exceeds observed IN concentrations in the upper troposphere at high S_i (e.g., $N_{IN\text{-}max}$=0.34 cm^{-3} when S_i=50%). Therefore, we also include a modified Meyers glaciation function (hereafter M _capped) where $N_{IN\text{-}max}$ is capped at 0.026 cm^{-3} when S_i=30%:

For S_i < 30%: Eq. 4

For S_i > 30%: $N_{IN-\max} = \exp(6.269 + 12.96(30\%))$ (5)

To incorporate ice crystal fallout into our parcel model simulations, we follow the method of Kärcher (2003). In each parcel model time step (dt - sec), a fraction of ice particles (F - dimensionless) falls out of each parcel model bin:

$$F = \frac{V_{fall}(R_{ice}) * \Delta t}{H} \quad (6)$$

where V_{fall} (R_{ice}) is the fallout velocity (m sec^{-1}), R_{ice} is the ice crystal radius in each bin (m), and H is the parcel depth (m).

In our parcel model simulations, H is set to 100 m, 500 m or ∞, but optical depth calculations always assume a cloud depth (Δz) of 1000 m. Parcel evolution is sensitive to H, while Δz is simply a scalar required for optical depth calculations. Physically, H represents the depth an ice crystal must fall before it is removed from the parcel. H is smaller than Δz to account for the fact that cloud particles do not have to fall through the entire Δz to be removed from the generating region of the cloud. For example, Δz could be greater than H if clouds do not have freezing occurring through their entire depth. When presenting our results, we often focus on H=100 m runs which represent the maximum realistic impact from fallout.

2.3 Parcel modeling approach

2.3.1. Parcel model experiments

To investigate the processes controlling cirrus P(σ) calculated over the duration of parcel runs, we completed two experiments (Table 1). For experiment 1, we first lifted a parcel 1000 m varying $\overline{w}$, T_o, P_o, IN glaciation function and concentration, and H (Table 2). For the second experiment, we superimposed idealized atmospheric waves having w(t) of the form:

$$w(t)= \overline{w} + A\sin(2\pi t/\tau_{wave}) \tag{7a}$$

where τ_{wave} is the wave period (sec), and A is the w amplitude (m sec^{-1}).

Eq. 7a corresponds to temperature perturbations of the form:

$$T(t) = T_o + \overline{w}\Gamma_{ice}t + \Gamma_{ice}A\frac{\tau_{wave}}{2\pi}\left(\cos\left(\frac{2\pi t}{\tau_{wave}}\right)-1\right) \tag{7b}$$

where Γ_{ice} is the lapse rate (K m^{-1}) – pseudoadiabatic with respect to ice processes.

When $\overline{w}$=0, Eq. 7b results in a maximum temperature excursion (ΔT [K]) of:

$$\Delta T = A\Gamma\left(\frac{\tau_{wave}}{2\pi}\right) \tag{7c}$$

The idealized wave trajectories helped us identify scales that affect cirrus optical depth evolution, but do not necessarily imitate observed atmospheric motions. Using a typical upper tropospheric horizontal wind speed of 30 m sec^{-1}, a wave of period τ_{wave} can be associated with different spatial scales in the atmosphere: turbulent scale (τ_{wave}=10 seconds or 0.3 km), convective scale (τ_{wave}=100 seconds or 3 km), mesoscale (τ_{wave}=1000 seconds or 17 minutes, 30 km), and synoptic scale (τ_{wave}=10,000 seconds or 167 minutes, 300 km).

Table 1: Dynamics and ice formation mechanism for parcel model experiments.
Experiment 1 runs are labeled with a "u" indicating a uniform vertical velocity.
Experiment 2 runs are labeled with an "s" indicating a sinusoidally varying vertical velocity.

Experiment	**Vertical velocity (w) (Eq. 7):**	**Freezing rate (J)**	
		Homogeneous	***Heterogeneous***
Exp. 1	Uniform Vertical Velocity $\overline{w} \neq 0$; A = 0	Koop (Eq. 2)	KL (Eq. 3), M (Eq. 4) or M_capped (Eq. 5)
Exp. 2A.	Superimposed Waves $\overline{w}$=0; A, $\tau_{wave} \neq 0$	N_{ice} (t=0)≠ 0	
Exp. 2B	Superimposed Waves $\overline{w}$, A, $\tau_{wave} \neq 0$	Koop (Eq. 2)	KL (Eq. 3), M (Eq. 4) or M_capped (Eq. 5)

Depending on τ_{wave} and ΔT, waves can influence both the evolution of existing, and the formation of new, cirrus cloud crystals. To separate the impacts of waves on cirrus formation and cirrus evolution, we completed parcel model runs lasting 2.7 hours (10,000 seconds) with: a) prescribed initial cirrus clouds, $\overline{w}$= 0. b) explicit cirrus formation, $\overline{w}$= 10 cm sec^{-1}. (Table 1 – Experiments 2A and 2B).

2.3.2. Calculation of P(σ) and comparison of modeled and observed P(σ)

In this paper, we determine the influence of specific processes on P(σ) calculated over the duration of Lagrangian parcel model experiments. For experiment 1, we calculated P(σ) from cirrus formation to the end of the experiment. For experiment 2a, P(σ) was calculated over the entire duration of the experiment. For experiment 2b, P(σ) was calculated from cirrus formation to the end of the experiment. All P(σ) were normalized and were computed with an σ interval of 0.1.

Observations and climate models represent P(σ) over spatial and temporal domains that differ from our Lagrangian parcel model experiments. For example, P(σ) derived from ground-based lidars represent observations at a single location and P(σ) in climate models represent a large spatial domain in a single model time step. Clearly, direct comparisons of our calculated P(σ) to other observational and modeling frameworks requires temporal stationarity and spatial uniformity assumptions that do not always apply. However, our goal is to diagnose the processes controlling the overall shapes of P(σ). As a result, our results should be useful for understanding the causes for P(σ) shape, regardless of the time period or spatial domain under consideration.

2.3.3. Attributing P(σ) to microphysical and dynamical processes

We identify the processes determining P(σ) by comparing freezing, growth and fallout timescales diagnosed from the parcel model experiments. To illustrate how freezing, growth and fallout timescales influence P(σ), we approximate cirrus optical depth as:

$$\sigma = 2\pi {R_{eff}}^2 N_{ice} \Delta z \tag{8}$$

By taking the time derivative of Eq. 8 and substituting the diffusional growth equation and the time derivative of N_{ice} due to freezing and fallout, we arrive at Eq. 9:

.

$$\frac{d\sigma}{dt} = 2\pi\Delta z {R_{eff}}^2 P_{freezing}(J, r_o) N_{CCN} + \frac{4\pi\Delta z}{\rho_{ice}} D\rho_{sat}(T,P) S_i N_{ice} \ldots$$

$$- \frac{\sigma V_{fall}(R_{eff})}{H} \tag{9}$$

where $P_{freezing}$ is the probability of aerosol freezing (sec^{-1}), J is the freezing rate (m^{-3} sec^{-1}), r_o is the aerosol radius (m), N_{CCN} is the number concentration of aerosol (m^{-3}), D=diffusion coefficient ($m^2 sec^{-1}$), ρ_{sat}=saturation vapor density (kg m^{-3}), P=pressure (Pa) and ρ_{ice}=density ice (kg m^{-3}).

The microphysical processes with the shortest timescales will dominate the optical depth evolution and determine $P(\sigma)$. We rewrite Eq. 9, a simplified algebraic equation, in a schematic form with characteristic timescales:

$$\frac{d\sigma}{dt} \sim \frac{\sigma}{\tau_{freezing}} + \frac{\sigma}{\tau_{growth}} - \frac{\sigma}{\tau_{fallout}} \tag{10}$$

Using our parcel model output, we can estimate the characteristic timescales in Eq.10 and diagnose the processes responsible for $P(\sigma)$. We diagnose the timescales in Eq. 10 for a resolved size distribution with coupled microphysical and dynamical processes from our parcel model output as follows:

i) Freezing timescale ($\tau_{freezing}$): model time from the start (N_{ice}=0) to the end (N_{ice}= $N_{ice\text{-}max}$) of freezing.

ii) Growth timescale (τ_{growth}): model time for S_i to decrease to 1/e of its maximum value due to deposition. We compute τ_{growth} at a constant T (T when N_{ice}= $N_{ice\text{-}max}$) with no fallout (N_{ice}= $N_{ice\text{-}max}$) starting at the maximum S_i.

iii) Fallout timescale ($\tau_{fallout}$): average model time for ice crystals to fall the distance H. $\tau_{fallout}$ is found by finding R_{eff} and averaging the resulting fall speed at each model time step from the end of freezing until all ice has fallen out or another freezing event begins.

In addition to the microphysical processes in Eq. 10, the imposed dynamics influence cirrus $P(\sigma)$ by controlling the time evolution of S_i and T (see S_i and T dependence in Eq. 9).

Therefore, we also calculate parcel model dynamical timescales for comparison to microphysical timescales. For experiment 1, we calculate a lift S_i generation timescale ($\tau_{lift\text{-}hom}$ or $\tau_{lift\text{-}het}$) the time required to generate the critical S_i for homogeneous ($\tau_{lift\text{-}hom}$) or heterogeneous freezing ($\tau_{lift\text{-}het}$) by adiabatic lifting at $\overline{w}$ starting from S_i =0%. For experiment 2, we compare τ_{wave} to the microphysical timescales in Eq. 10.

3. Results

3.1. Summary of all results

In this section, we describe the primary results from the uniform updraft and idealized wave model experiments. More detailed descriptions of results are found in section 3.2 for the uniform updraft experiment and section 3.3 for the superimposed wave experiment.

With uniform updraft trajectories, we found the most important control on cirrus $\overline{\sigma}$ and P(σ) shape was $\tau_{fallout}$. Indeed, $\tau_{fallout}$ segregated cirrus P(σ) shape into two distinct regimes: a fallout-dominated regime and a limited-fallout regime. For the uniform updraft experiment with H≠∞, the fallout-dominated regime occurred at small $\overline{w}$, resulted in small $\overline{\sigma}$ and had a monotonically decreasing P(σ) while the limited fallout regime occurred at large $\overline{w}$, resulted in large $\overline{\sigma}$ and had a P(σ) peaked at large optical depths (Figure 3). The addition of IN had the largest impact on cirrus $\overline{\sigma}$ and P(σ) in the limited-fallout regime (Figure 4). Here, IN limited the maximum S_i, decreased the maximum N_{ice}, reduced the optical depth of the P(σ) peak, and added a monotonically decreasing tail at small optical depths. In contrast, $\overline{\sigma}$ and P(σ) shape were independent of IN concentration in the fallout-dominated regime (Figure 4). In section 3.2, we present and discuss in greater detail how $\overline{w}$, temperature, H, IN concentration, and IN glaciation function influence cirrus timescales, σ evolution, and P(σ).

For the superimposed wave experiment, wave ΔT and the comparison of wave τ_{wave} to $\tau_{fallout}$, τ_{growth}, and $\tau_{freezing}$ determined the influence of waves on the optical depth evolution and P(σ). To perturb the optical depth evolution of a pre-existing cirrus cloud, waves had to generate

significant changes in S_i, have large $\tau_{wave}/\tau_{growth}$ and have small $\tau_{wave}/\tau_{fallout}$. Only mesoscale waves superimposed on limited-fallout regime cirrus met these criterion and had broadened $P(\sigma)$ (Figure 5). In section 3.3, we present how idealized waves influence pre-existing cirrus by comparing the mean σ and std(σ) in parcel model runs with and without idealized waves.

In addition to affecting the evolution of pre-existing cirrus σ, superimposed waves also generated new freezing events that modified $P(\sigma)$. ΔT, $\tau_{fallout}$ and τ_{growth} affected the ability of waves to generate new freezing events by influencing S_i and the total water in the parcel. To cause new homogeneous freezing events, waves had to generate high S_i over the duration of typical $\tau_{freezing}$. In section 3.3, we present which idealized waves generated new freezing events and how wave amplitude and τ_{wave} affected N_{ice}.

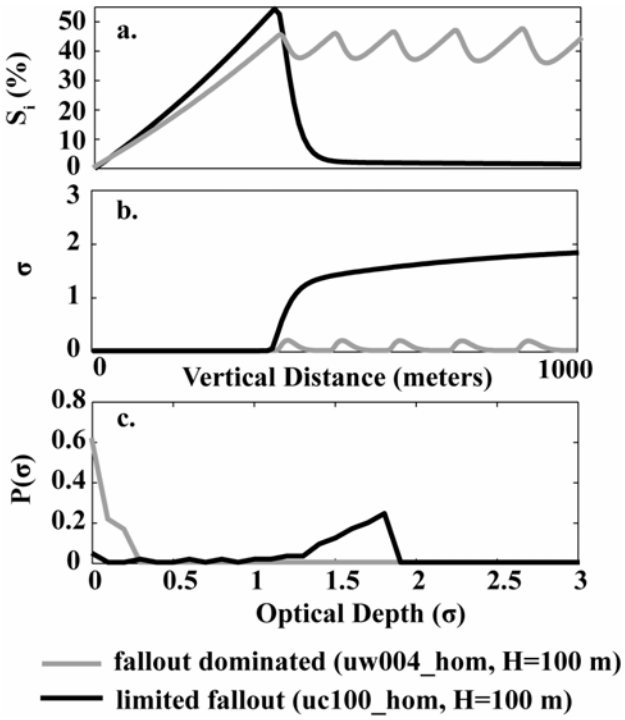

Figure 3. The fallout dominated and limited fallout regimes: a. S_i evolution b. Optical depth evolution c. $P(\sigma)$ along trajectory. In the fallout-dominated regime, $\tau_{fallout} < \tau_{growth}$ and $\tau_{lift\text{-}hom}$ resulting in large S_i, small optical depths, and a monotonically decreasing $P(\sigma)$. In the limited-fallout regime, $\tau_{fallout} > \tau_{growth}$ and $\tau_{lift\text{-}hom}$, resulting in lower S_i, larger optical depths and a skewed $P(\sigma)$ centered at large optical depths.

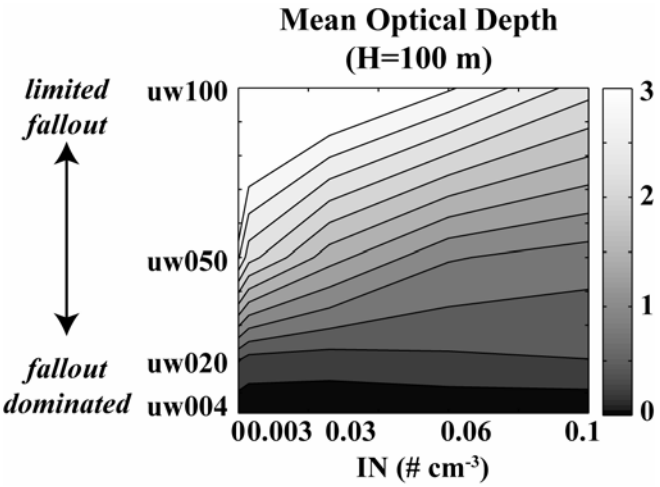

Figure 4: Mean optical depth as a function of IN concentration and P(σ) regime. In the fallout-dominated regime, mean optical depth is independent of IN concentration. In the limited-fallout regime, mean optical depth depends strongly on IN concentration. The $\overline{\sigma}$ is contoured in 0.25 increments. Values are computed from Experiment 1 runs with Koop homogeneous freezing and KL heterogeneous freezing (Table 2).

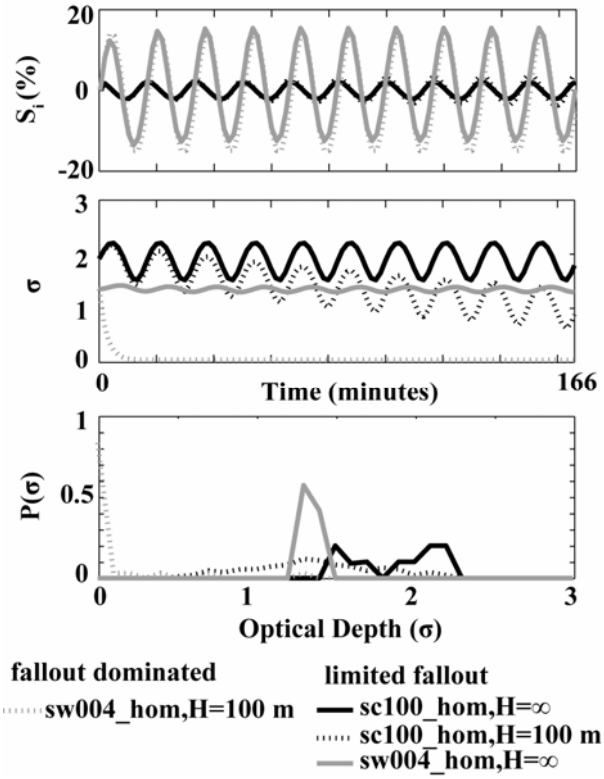

Figure 5: Cirrus evolution with superimposed mesoscale waves for fallout-dominated and limited-fallout initial cirrus clouds: a. S_i evolution b. Optical depth evolution c. P(σ) along trajectory. For the sw004_hom limited-fallout case, ice crystal growth could not keep pace with wave-induced changes in S_i ($\tau_{wave} / \tau_{growth} < 1$). For the sw004_hom fallout-dominated case, waves have little influence on cirrus P(σ) because $\tau_{wave} / \tau_{growth} < 1$ and $\tau_{wave} / \tau_{fallout} > 1$. For the sc100_hom limited-fallout cases, waves caused a broadening of P(σ) because $\tau_{wave} / \tau_{growth} > 1$ and $\tau_{wave}/\tau_{fallout} << 1$. For all model runs, $\Delta T = 2$ K, $\overline{w}=0$ and $S_{io}=0\%$.

3.2. Experiment 1: Uniform updraft experiment results

With uniform updrafts, the cirrus microphysical properties and timescales that determine P(σ) depended on the freezing mechanism and the supersaturated vapor content [ρ_v (kg m^{-3})]. Given the importance of freezing processes for microphysical timescales, we summarize the results of experiment 1 first for runs with only homogeneous freezing and then for runs with both heterogeneous and homogeneous freezing (Table 2).

Table 2: Experiment 1 initial temperature (T_o) and pressure (P_o), $\overline{w}$, and lift S_i generation rates. For all uniform updraft experiment runs, a parcel is lifted 1000 m at $\overline{w}$ with S_{io} = 0% starting from T_o=233 ("warm" indicated with "w") or T_o=213 ("cold" indicated with "c"). Figures showing experiment 1 results (Figures 3,4,6,7,8) plot parcel model runs that were completed with Koop (Eq. 2) homogeneous freezing only ("_hom") or with both Koop homogeneous and KL (Eq. 3) heterogeneous freezing ("_hom&het").

Exp. 1 Run	**T_o (K)**	**P_o (Pa)**	**$\overline{w}$ (cm / sec)**	**$\tau_{Ilft\text{-}hom}$ (min.)[a]**	**$\tau_{Ilft\text{-}het}$ (min.)[a]**
uw004	233	34000	4	160	113
uw020			20	33	23
uw100			100	7	5
uc004	213	17000	4	148	94
uc020			20	30	19
uc100			100	6	4

[a] see text for definitions

3.2.1. Homogeneous freezing only runs

3.2.1.1. Impact of $\overline{w}$ and T_o on homogeneous freezing microphysical timescales

For runs with homogeneous freezing only (Koop – Eq. 2), cirrus microphysical properties (Table 3) and timescales (Table 4) changed primarily with $\overline{w}$, but also with T_o. The direct link between $\overline{w}$ and N_{ice} coupled large $\overline{w}$ with short $\tau_{freezing}$ and short τ_{growth}. τ_{growth} and $\tau_{lift\ -hom}$ varied together because they both depended on $\overline{w}$; and large $\tau_{lift\ -hom}$ / τ_{growth} resulted regardless of $\overline{w}$. The decrease in R_{eff} with increasing N_{ice} coupled large $\overline{w}$ with long $\tau_{fallout}$. T_o influenced cirrus microphysical properties and timescales for the homogeneous freezing runs by affecting J_{hom} and ρ_v. Despite the increase in J_{hom} at low T_o, $\tau_{freezing}$ was essentially independent of T_o. The increase in N_{ice} at low T_o did, however, result in faster τ_{growth}. T_o had the greatest impact on $\tau_{fallout}$. At low T_o, the increase in N_{ice} from larger J_{hom} and the decrease in R_{eff} from reduced ρ_v led to the smallest R_{eff} and longest $\tau_{fallout}$.

Table 3: Cirrus cloud properties for parcel model runs with homogeneous freezing and fallout (H=100 m). For homogeneous freezing, the maximum N_{ice} and optical depth increased with $\overline{w}$ while the maximum R_{eff} decreases with $\overline{w}$. The percentage change in cirrus cloud properties from H=∞ to H=100 m is listed in parenthesis. Including fallout increased the maximum N_{ice} and the maximum R_{eff}, but decreased the maximum optical depth, especially for small $\overline{w}$.

Exp. 1 Run	Max. N_{ice} (#/cm^3)	Max. R_{eff} (μm)	Max. Optical Depth
uw004_hom	0.04 (18%)	84 (2%)	0.2 (-86%)
uw020_hom	0.35 (0%)	57 (55%)	1.4 (-52%)
uw100_hom	4.46 (0%)	16 (1%)	6.1 (-13%)
uc004_hom	0.06 (2%)	49 (50%)	0.1 (-63%)
uc020_hom	0.60 (0%)	15 (6%)	0.5 (-32%)
uc100_hom	8.50 (0%)	6 (0%)	1.8 (-3%)

Table 4: Cirrus evolution timescales and ratios for parcel model runs with homogeneous freezing and fallout (H=100 m). For all homogeneous freezing cases, $\tau_{freezing} < \tau_{growth}$, $\tau_{freezing} < \tau_{fallout}$ and $\tau_{growth} < \tau_{lift-hom}$. $\tau_{lift-hom}$ and τ_{growth} are coupled because of the dependence of N_{ice} on $\overline{w}$. For small $\overline{w}$, $\tau_{fallout} < \tau_{growth}$, especially at high T_o. As a result, ice crystals fall out of the parcel before depleting the S_i. For large $\overline{w}$, $\tau_{growth} < \tau_{fallout}$, especially at low T_o.

Exp. 1 Run	$\tau_{freezing}$ (min.)[a]	τ_{growth} (min.)[a]	$\tau_{fallout}$ (min.)[a,b]	$\tau_{lift-hom}/\tau_{growth}$[a]	$\tau_{fallout}/\tau_{growth}$[a]	$\tau_{fallout}/\tau_{lift-hom}$[a]
uw004_hom	7.1	23	6	7.0	0.3	0.04
uw020_hom	5.0	5	12	7.1	2.6	0.36
uw100_hom	0.6	1.0	54	6.9	56	8
uc004_hom	7.5	21	15	7.2	0.7	0.1
uc020_hom	2.3	4.0	60	7.6	15	2.0
uc100_hom	0.6	0.7	282	8.7	394	46

[a] See text for definitions.
[b] For uw100_hom, uc020_hom, and uc100_hom, $\tau_{fallout}$ calculations assume a constant temperature after a total net parcel displacement of 1000 m was reached.

3.2.1.2. P(σ) regimes for homogeneous freezing

Cirrus P(σ) was primarily determined by $\tau_{fallout}$. With $\tau_{fallout} = \infty$, large $\tau_{lift-hom}/\tau_{growth}$ allowed rapid S_i depletion and attainment of the maximum optical depth for a given N_{ice} and R_{eff} combination. As a result, P(σ) was peaked at the maximum optical depth but skewed towards smaller optical depths (see solid curves in Figure 6). When $\tau_{fallout} \neq \infty$, a competition between growth and fallout determined the optical depth evolution (Eq. 10). From the parcel model runs with homogeneous freezing, two regimes for cirrus evolution and P(σ) emerged: a) a limited-

fallout regime with $\tau_{fallout}/\tau_{growth} >> 1$ and $\tau_{fallout}/\tau_{lift\text{-}hom} >> 1$ b) a fallout-dominated regime with $\tau_{fallout}/\tau_{growth} << 1$ and $\tau_{fallout}/\tau_{lift\text{-}hom} << 1$ (Table 4).

(a) The limited-fallout regime: $\tau_{fallout}/\tau_{growth} >> 1$ and $\tau_{fallout}/\tau_{lift\text{-}hom} >> 1$. The limited-fallout regime was characterized by fast drawdown of S_i after a single homogeneous freezing event and sustained large optical depths. The limited-fallout regime P(σ) had a peak at large optical depth values skewed toward smaller optical depths and could be approximated by a gamma distribution with a large $\overline{\sigma}$ and $\nu > 1$ (Eq. 1). Excluding runs with H=∞ (i.e., $\tau_{fallout} = \infty$), large $\overline{w}$ was required for a limited-fallout regime evolution. The largest $\tau_{fallout}/\tau_{growth}$ occurred for T_o = 213 K and $\overline{w}$ = 100 cm sec^{-1} (uc100_hom runs in Figure 6). At large $\overline{w}$, H did not influence the P(σ) shape. In fact, fallout was so slow in the limited-fallout regime that for uw100_hom, large ρ_v allowed the optical depth to increase beyond the value it would attain with $\tau_{growth} = 0$ (not shown).

(b) The fallout-dominated regime: $\tau_{fallout}/\tau_{growth} <<1$ and $\tau_{fallout}/\tau_{lift\text{-}hom} << 1$. The fallout-dominated cirrus evolution had persistently high S_i and multiple homogeneous freezing events. In the fallout-dominated regime, ice crystals fell out of the parcel before they depleted the S_i. The fallout-dominated P(σ) had a monotonically decreasing P(σ) dominated by small optical depths and could be approximated by a gamma distribution with a small $\overline{\sigma}$ and $\nu \leq 1$ (Eq. 1). The smallest $\tau_{fallout}/\tau_{growth}$ and $\tau_{fallout}/\tau_{lift\text{-}hom}$ occurred in parcel model runs with T_o = 233 K, $\overline{w}$ = 4 cm sec^{-1} and H= 100 m (uw004_hom with H=100 m - Figure 6). After the first homogeneous uw004_hom freezing event, ice crystal deposition reduced the S_i to 45% from S_i=49% before falling out of the parcel completely. Subsequent lifting allowed new homogeneous freezing events and resulted in a larger maximum N_{ice} (Table 3). Larger H led to longer $\tau_{fallout}$, stronger S_i drawdown, and a longer optical depth decay. The fallout-dominated regime monotonically decreasing P(σ) shape resembles the observed wave cirrus P(σ) shape (compare Figure 1 and Figure 6).

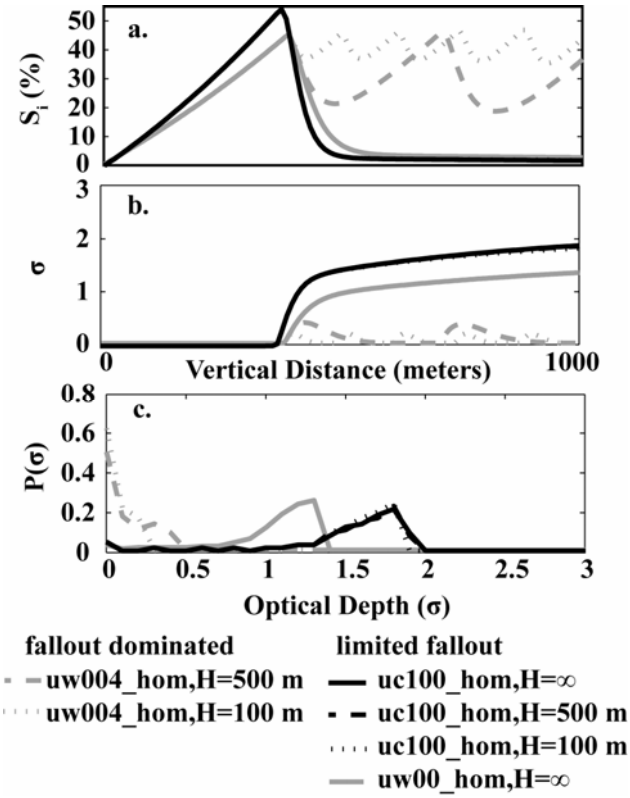

Figure 6. Cirrus evolution with homogeneous freezing for fallout-dominated and limited-fallout cases a. b. Evolution of S_i and optical depth c. P(σ) along trajectory Increasing H had a strong influence on the uw004_hom runs, but had little influence on the uc100_hom runs.

3.2.2. Addition of heterogeneous freezing

3.2.2.1 Microphysical timescales and P(σ) regimes with both homogeneous and heterogeneous freezing

We found $\tau_{lift\text{-}het}/\tau_{growth}$ and $\tau_{fallout}/\tau_{lift\text{-}het}$ determined how heterogeneous nucleation affected cirrus evolution and P(σ) in our parcel model runs. With a fixed IN concentration, N_{ice} generated by heterogeneous freezing had limited dependence on $\overline{w}$. As a result, τ_{growth} and $\tau_{fallout}$ did not depend on $\overline{w}$ (Table 5) and the coupling of $\tau_{lift\text{-}het}$ and τ_{growth} we observed for homogeneous freezing was removed (Table 4). $\tau_{lift\text{-}het}/\tau_{growth}$ decreased with larger $\overline{w}$ while $\tau_{fallout}/\tau_{lift\text{-}het}$ increased with larger $\overline{w}$ (Table 5).

Table 5: Cirrus evolution timescales and ratios with both Koop homogeneous and KL heterogeneous freezing. For a fixed IN concentration, τ_{growth} and $\tau_{fallout}$ depend only on T_o, not on $\overline{w}$. For all $\overline{w}$, small $\tau_{fallout}/\tau_{growth}$ imply IN fall out before they deplete S_i. With small $\overline{w}$, small $\tau_{fallout}/\tau_{lift}$ indicate fallout occurs many times over 1000 m of lifting. At large $\overline{w}$, small $\tau_{lift\text{-}het}$ / τ_{growth} indicate S_i increases despite growth by glaciated IN and homogeneous freezing occurred. Indeed, the critical N_{ice} required to maintain $\tau_{lift\ –het}$ / $\tau_{growth} = 1$ increases with $\overline{w}$. Because of large $\tau_{fallout}/\tau_{lift\text{-}het}$, IN stay with the parcel and can inhibit homogeneous freezing.

Exp 1 Run	**Critical N_{ice} (# cm^{-3})[a]**	**τ_{growth} (min.)[b]**	**$\tau_{fallout}$ (min.)[b]**	**$\tau_{lift\text{-}het}$ / τ_{growth}[b]**	**$\tau_{fallout}$ / τ_{growth}[b]**	**$\tau_{fallout}$ / $\tau_{lift\text{-}het}$[b]**
uw004_hom&het	0.004	29	12	3.8	0.39	0.1
uw020_hom&het	0.07	29	12	0.8	0.39	0.5
uw100_hom&het	0.8	29	12	0.2	0.39	2.6
uc004_hom&het	0.008	34	26	2.8	0.77	0.3
uc020_hom&het	0.12	34	26	0.6	0.77	1.4
uc100_hom&het	1.4	34	26	0.1	0.77	7.0

[a]The critical N_{ice} is the number of ice crystals required for $\tau_{lift\ –het\ /}\ \tau_{growth} = 1$.
[b] Calculations were done for an IN concentration of 0.03 cm^{-3} with H=100 m. See text for descriptions.

When H = ∞, we found cirrus evolution depended only on $\tau_{lift\ -het}/\tau_{growth}$, similar to pioneering research by DeMott et al. (1997). As $\tau_{lift\ -het}/\tau_{growth}$ decreased, the impact of IN decreased from completely inhibiting homogeneous freezing to limiting homogeneous freezing (see transition from light gray to black solid curves in Figure 7).

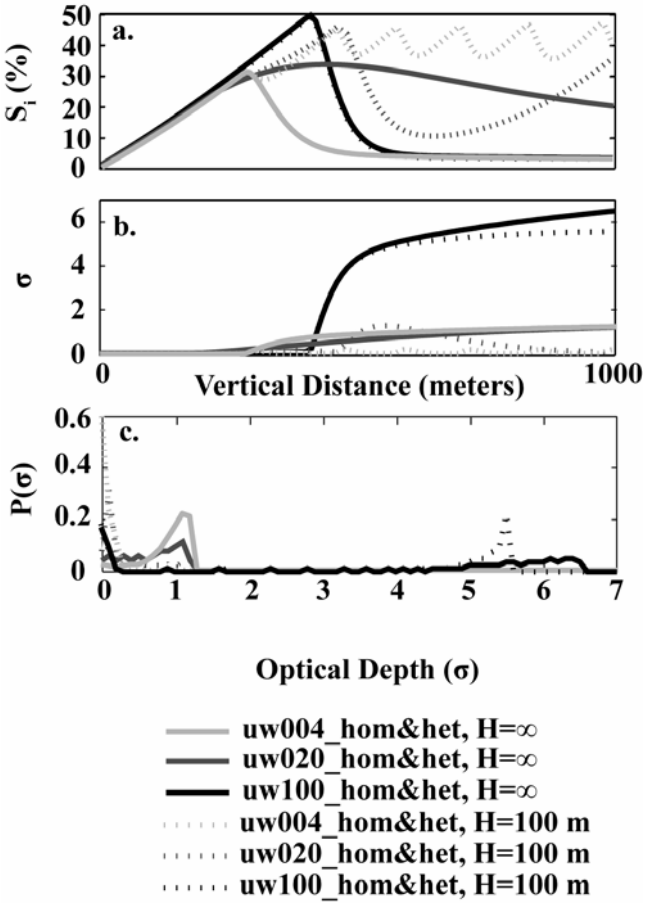

Figure 7. Cirrus evolution for a range of updrafts and constant IN concentration of 0.03 cm^{-3}: a&b. Evolution of S_i and optical depth With small $\overline{w}$ (uw004_hom&het) and H=∞, $\tau_{lift\text{-}het} / \tau_{growth} > 1$ and ice crystal growth inhibits homogeneous freezing. With intermediate $\overline{w}$ (uw020_hom&het) and H=∞, $\tau_{lift\text{-}hom} / \tau_{growth} >\approx 1$ delaying S_i depletion but still inhibiting homogeneous freezing. With large $\overline{w}$ (uw100_hom&het) and H=∞, $\tau_{lift\text{-}hom} / \tau_{growth} < 1$ and homogeneous freezing occurs after heterogeneous freezing. Larger IN concentrations increase $\tau_{lift\text{-}het} / \tau_{growth}$ (not shown). With fallout, IN can delay, but do not inhibit high S_i and homogeneous freezing. With small $\overline{w}$ (uw004_hom&het) and H=100 m, $\tau_{fallout}$ is faster than τ_{growth} and $\tau_{lift\text{-}het}$. Similar to the homogeneous-only fallout-dominated case, large S_i and small optical depths result. At intermediate $\overline{w}$ (uw020_hom&het) and H=100 m, fallout decreases $\tau_{lift\text{-}het} / \tau_{growth}$ and homogeneous freezing occurs. With large $\overline{w}$ (uw100_hom&het) and H=100 m, $\tau_{fallout}$ is faster than τ_{growth} but slower than $\tau_{lift\text{-}het}$. Similar to the homogeneous-only limited-fallout case, low S_i and large optical depths result. In this case, IN limit the N_{ice} and optical depth generated by homogeneous freezing. Larger IN concentrations or larger H increase $\tau_{fallout} / \tau_{growth}$ (not shown). *c. P(σ) along trajectory* Resulting P(σ) are primarily controlled by

$\overline{w}$ and resemble the homogeneous-only limited-fallout and fallout-dominated regimes (Figure 6). For the limited-fallout regime with heterogeneous freezing, the P(σ) has an additional monotonically decreasing optical depth tail.

When H ≠ ∞, fallout dramatically reduced the impact of IN on cirrus optical depth evolution, especially at small $\overline{w}$. Indeed, for all runs with H=100 m and intermediate IN concentrations (0.003 cm^{-3} to 0.1 cm^{-3}), IN played a minor role in cirrus evolution and homogeneous freezing dominated cirrus optical depth evolution and P(σ). At intermediate $\overline{w}$, fallout and IN concentration had the strongest influence on the sequence of freezing events. For example, homogeneous freezing occurred in parcel model run uw020_hom&het with H=100 m because fallout reduced $N_{ice,}$ decreased $\tau_{lift\text{-}het}$ / τ_{growth}, and allowed S_i to increase (Figure 7). At $\overline{w}$ extremes, IN did not influence the sequence of freezing events and similar regimes for cirrus evolution and P(σ) emerged as for the homogeneous freezing only runs: a) a fallout-dominated regime with IN at small $\overline{w}$ (uw004_hom&het, H=100 m, light gray dotted curves - Figure 7) b) a limited-fallout regime with IN at large $\overline{w}$ (uw100_hom&het, H=100 m – black dotted curves Figure 7). Because $\tau_{lift\text{-}het}$ was the only timescale that depended on $\overline{w}$ for heterogeneous freezing, $\tau_{fallout}/\tau_{growth}$ was always << 1 and variation in $\tau_{lift\text{-}het}/\tau_{growth}$ and $\tau_{fallout}/\tau_{lift\text{-}het}$ distinguished the fallout-dominated and limited-fallout regimes (Table 5).

(a) The limited-fallout regime with IN: $\tau_{lift\text{-}het}/\tau_{growth}<<1$ and $\tau_{fallout}/\tau_{lift\text{-}het} >> 1$ (Table 5). At large $\overline{w}$, small $\tau_{lift\text{-}het}/\tau_{growth}$ quickly allowed large S_i and homogeneous freezing to occur. While small $\tau_{fallout}/\tau_{growth}$ show IN fell out before depleting S_i, large $\tau_{fallout}/\tau_{lift\text{-}het}$ imply IN did not fallout over the 1000 m of lifting. Indeed, IN stayed with the parcel and limited homogeneous freezing by reducing the maximum S_i. Despite the presence of IN, relatively large optical depths resulted because of large homogeneous freezing rates generated by large $\overline{w}$. The P(σ) for the limited-fallout regime with IN had a peak at high values with a monotonically decreasing tail at low values. The limited-fallout regime with IN P(σ) could not be represented by a single gamma

distribution. The P(σ) for a limited-fallout regime with heterogeneous freezing resembles the observed anvil cirrus P(σ) (compare Figure 7 and Figure 1).

(b) The fallout-dominated regime with IN: $\tau_{lift\text{-}het}/\tau_{growth} >> 1$ and $\tau_{fallout}/\tau_{lift\text{-}het} << 1$ (Table 5). Although $\tau_{lift\text{-}het}/\tau_{growth}$ was large at small $\overline{w}$, small $\tau_{fallout}/\tau_{lift\text{-}het}$ and small $\tau_{fallout}/\tau_{growth}$ indicate glaciated IN quickly fell out of the parcel before reducing S_i. After an initial heterogeneous freezing event, the subsequent cirrus evolution was controlled by multiple new homogeneous freezing events, similar to the fallout-dominated homogeneous freezing regime. Optical depths remained small because heterogeneous freezing and subsequent homogeneous freezing events had similar N_{ice} and optical depths. The P(σ) for the fallout-dominated regime with IN had monotonically decreasing optical depths dominated by low values. The fallout-dominated with IN P(σ) could be approximated by a gamma distribution with a small $\overline{\sigma}$ and $\nu \leq 1$ (Eq. 1).

3.2.2.2 Impact of IN concentration on cirrus optical depths

To illustrate the dramatic influence of $\tau_{fallout}$ on cirrus optical depths, we summarize how $\overline{\sigma}$ and P(σ) vary as a function of IN concentration, $\overline{w}$, and H (Figure 8). With small $\overline{w}$, H had the largest impact on $\overline{\sigma}$ and the sensitivity of $\overline{\sigma}$ to IN concentration. When H=∞ and $\overline{w}$ was small , IN concentration determined $\overline{\sigma}$. If IN concentrations exceeded 0.03 cm^{-3}, $\overline{\sigma}$ was larger than for runs with only homogeneous freezing (Figure 8a). When H=100 m and $\overline{w}$ was small, $\overline{\sigma}$ and P(σ) were independent of IN concentration (Figure 8b). Larger IN concentration delayed homogeneous freezing events, but did not affect the magnitude of the resulting optical depths (not shown). With large $\overline{w}$, H did not have a strong influence on $\overline{\sigma}$ or the importance of the IN concentration (compare Figure 8a and 8b). In fact, IN concentration was more important than H for determining $\overline{\sigma}$ and P(σ) (Figure 8). In this limited-fallout regime with IN, increasing IN concentrations decreased the mean cirrus optical depth by reducing the N_{ice} formed by homogeneous freezing. IN were most effective at limiting homogeneous freezing N_{ice} at low T_o

where they had the longest $\tau_{fallout}$. Larger H led to a longer $\tau_{fallout}$, especially when there were small N_{ice} and decreased the prevalence of the fallout-dominated regime (see Figure 8c). In general, larger H led to longer heterogeneous freezing events and increased optical depths. At intermediate $\overline{w}$ (20 cm sec^{-1}), the sequence of freezing events occurring over a 1000 m lift depended strongly on H. However, for w004 and w100, the sequence of freezing events remained similar with H=500 m.

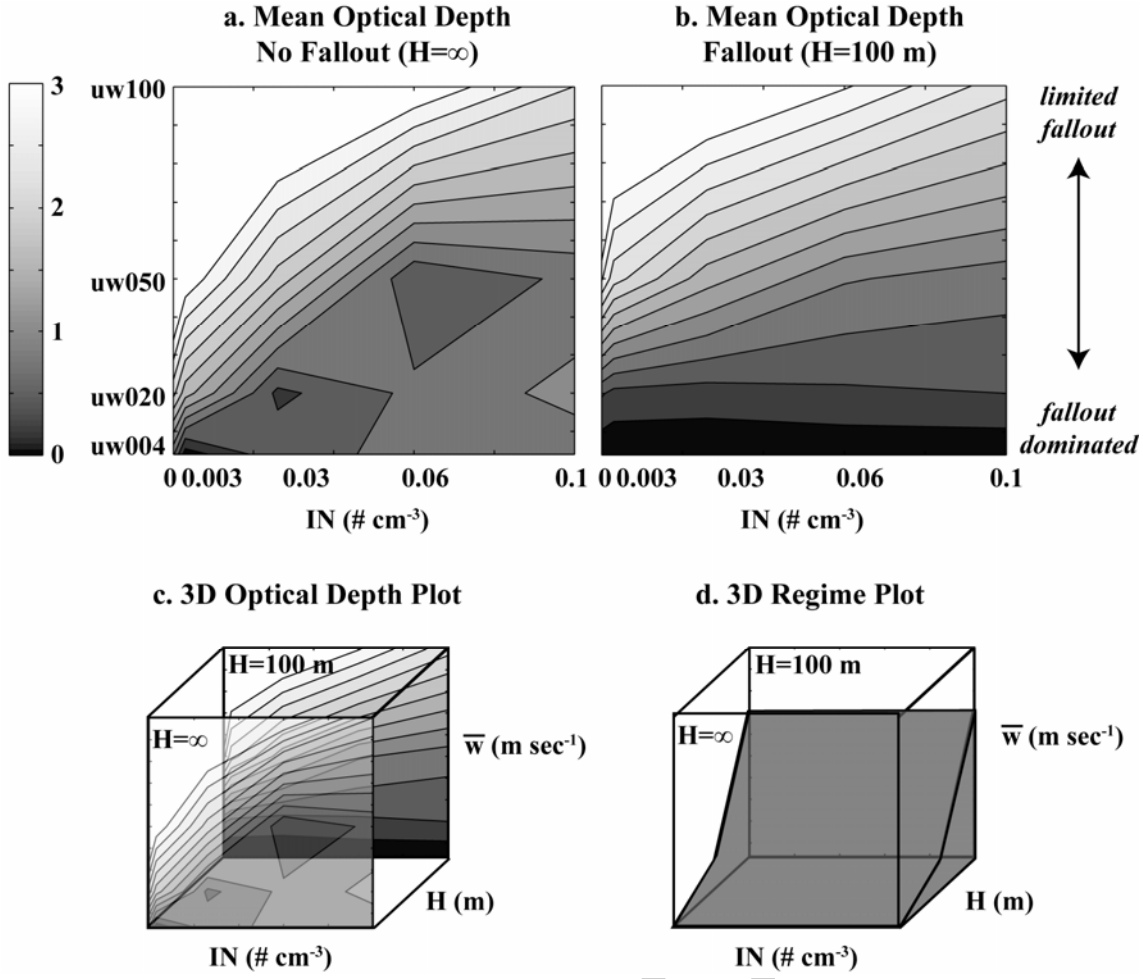

Figure 8: Impacts of IN concentration and fallout on $\overline{\sigma}$. The $\overline{\sigma}$ is contoured in 0.25 increments as a function of IN concentration and run (Table 2). *a. no fallout* IN concentrations influence the $\overline{\sigma}$ at all $\overline{w}$. For small $\overline{w}$, IN control the maximum N_{ice} and $\overline{\sigma}$. For large $\overline{w}$, IN limit the maximum optical depth. *b. fallout with H=100 m* For

small $\overline{w}$ (fallout-dominated regime), $\overline{\sigma}$ is independent of IN concentration. For large $\overline{w}$ (limited-fallout regime), IN still limit the maximum optical depth. *c. 3D plot* This cube shows 6a and 6b are limiting cases in a 3D space that includes IN, H, w. *d. 3D regime plot* The shaded area indicates the fallout-dominated regime ($\tau_{fallout} / \tau_{lift\text{-}het} < 1$ or $\tau_{fallout} / \tau_{lift\text{-}hom} < 1$). As H increases, the prevalence of the fallout-dominated regime decreases.

3.2.2.3 Impact of IN glaciation functions on cirrus optical depths

For a fixed IN concentration, IN glaciation thresholds only influenced cirrus optical depth evolution at small $\overline{w}$. With an IN concentration of 0.026 cm^{-3}, the more gradual M_capped glaciation function (Eq. 5) resulted in a 80% lower N_{ice} than the KL activity glaciation function (Eq. 3) (0.0055 cm^{-3} versus 0.026 cm^{-3}). On the other hand, at large $\overline{w}$, the IN glaciation function did not influence cirrus optical depths because all IN were quickly glaciated. For all $\overline{w}$ and H, the M glaciation function (Eq. 4) consistently had nearly constant optical depths and did not allow homogeneous freezing. The M glaciation function had an unlimited IN concentration and allowed the parcel to experience one long-lived heterogeneous freezing event. Regardless of $\overline{w}$, a steady state was achieved between glaciation of IN creating new ice crystals and fallout removing old ice crystals.

3.3. Experiment 2: Superimposed waves experiment results

3.3.1. Influence of idealized waves on pre-existing cirrus (Experiment 2a)

Both cirrus microphysical timescales and τ_{wave} control the influence of superimposed temperature perturbations on cirrus evolution. Two ratios could be used to evaluate the influence of waves on pre-existing cirrus: $\tau_{wave}/\tau_{growth}$ and $\tau_{wave} /\tau_{fallout}$. Large $\tau_{wave}/\tau_{growth}$ indicated ice crystal growth and sublimation keep up with wave-induced changes in S_i. Small $\tau_{wave} /\tau_{fallout}$ indicated ice crystals could be influenced by the wave-induced changes in S_i before falling out of the parcel. Large $\tau_{wave}/\tau_{growth}$ and small $\tau_{wave}/\tau_{fallout}$ allowed waves to perturb cirrus evolution and broaden $P(\sigma)$. For a gamma distribution, broadening $P(\sigma)$ with a constant $\overline{\sigma}$ corresponds to decreasing ν (Eq. 1). Synoptic waves (τ_{wave} = 166 minutes) had large $\tau_{wave}/\tau_{growth}$ and mostly large

$\tau_{wave}/\tau_{fallout}$ (Table 6). Therefore, when ice crystals were present, they could grow fast enough to maintain S_i=0% throughout cooling, but fallout occurred before the next wave crest. For mesoscale waves (τ_{wave} = 16 minutes), τ_{growth} and $\tau_{fallout}$ were longer, equal or shorter than τ_{wave}. As a result, mesoscale perturbations resulted in more complicated interactions because N_{ice} and R_{eff} determined if $\tau_{wave}/\tau_{growth}$ and $\tau_{wave}/\tau_{fallout}$ were greater or less than 1 (Figure 5). For turbulent scale (τ_{wave} = 0.16 minutes) and convective scale (τ_{wave} = 1.6 minutes) waves, small $\tau_{wave}/\tau_{growth}$ indicate optical depth oscillations were small, but small $\tau_{wave}/\tau_{fallout}$ allowed imprinting of optical depth oscillations over many wave periods.

Table 6: Wave and microphysical timescale ratios. $\tau_{wave}/\tau_{growth} > 1$ and $\tau_{wave}/\tau_{fallout} < 1$ are required for waves to perturb the optical depth evolution over multiple wave crests.

Exp 1 Run	**Mesoscale** $\tau_{wave}/\tau_{growth}$ [a,b]	**Mesoscale** $\tau_{wave}/\tau_{fallout}$ [a,b]
sw004_hom	0.6	2.9
sw020_hom	3.1	1.4
sw100_hom	17	0.3
sc004_hom	0.7	1.1
sc020_hom	3.7	0.3
sc100_hom	21	0.06

[a] For τ_{growth} and $\tau_{fallout}$ values, see Table 4.
[b] To convert listed mesoscale timescale ratios to other scales, multiple by 10^{-2} for turbulent waves, 10^{-1} for convective waves, and 10^{1} for synoptic waves. Turbulent τ_{wave} =16.6 *10^{-2} minutes, convective τ_{wave} =1.6*10^{-1} minutes, mesoscale τ_{wave} =16.6 minutes, and synoptic τ_{wave} =16.6*10^{1} minutes.

To illustrate the importance of wave and microphysical timescale interactions, we calculated optical depth changes (wave – no wave) resulting from superimposed waves with ΔT = 2 K and variable τ_{wave} and vertical velocity amplitude A (Figure 9). Starting at ice saturation, ΔT=2 K did not generate the required S_i for new homogeneous freezing events (S_i=50-54%). As a result, symmetric waves had no impact on $\overline{\sigma}$ with H=∞ (Figure 9a), but could increase the std(σ) about the no wave mean with large $\tau_{wave}/\tau_{growth}$ (Figure 9b). When H=100 m, waves could influence both $\overline{\sigma}$ (Figure 9c) and the std(σ) about the no wave mean with large $\tau_{wave}/\tau_{growth}$ and small $\tau_{wave}/\tau_{fallout}$ (Figure 9d). An increase in $\overline{\sigma}$ occurred for synoptic waves because the combination of fallout and sublimation resulted in a faster decay in optical depth. Though not

shown in Figure 10, larger H resulted in longer $\tau_{fallout}$ and increased the potential for waves to influence the optical depth evolution over multiple wave crests.

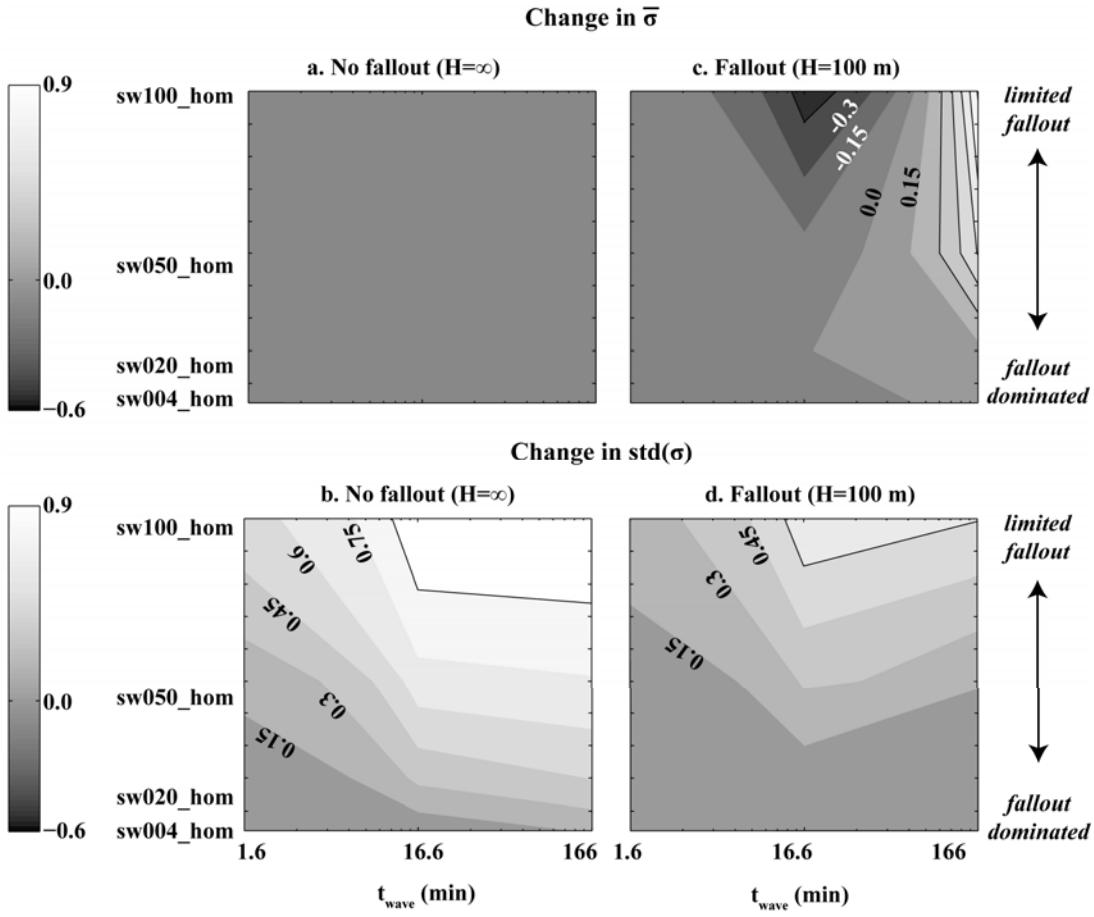

Figure 9: Change (wave – no wave) in cirrus optical depth moments resulting from superimposed waves of varying τ_{wave} and a fixed ΔT. For all runs, the initial S_i was 0%, and the change in std(σ) was calculated after subtracting a line fitted to the no wave optical depth decay. *a&b. Change in $\overline{\sigma}$ and std(σ) about the no wave mean with H= ∞.* Without fallout, waves have no impact on $\overline{\sigma}$. The wave impact on std(σ) increases with larger τ_{wave} and increased N_{ice} because $\tau_{growth} < \tau_{wave}$. *c&d. Change in $\overline{\sigma}$ and std(σ) about the no wave mean with H=100 m.* With fallout, waves influenced $\overline{\sigma}$ because they altered the optical depth decay. The impact of waves on std(σ) diminishes, but remains evident for mesoscale waves in the limited-fallout regime.

In addition to timescale ratios, wave ΔT also controlled cirrus evolution by affecting S_i and ρ_v. As ΔT increased, larger changes in S_i and ρ_v led to larger optical depth variations, increased deposition and sublimation, and occasionally new freezing events. For example, new freezing events occurred when synoptic waves with ΔT =16 K were superimposed on the evolution of fallout-dominated and limited-fallout regime cirrus clouds (Figure 10). For the fallout-dominated evolution, large $\tau_{wave}/\tau_{fallout}$ resulted in the initial cirrus quickly falling out of the parcel, S_i increasing, and a new homogeneous freezing event occurring in the first wave ascent. For the limited-fallout evolution, small $\tau_{wave}/\tau_{fallout}$ allowed the initial cirrus to persist until sublimation occurred due to adiabatic warming in the first wave descent. After complete sublimation of the initial cirrus cloud, S_i increased on the subsequent wave ascent, and a new homogeneous freezing event occurred. Not surprisingly, conservation of total parcel water was critical for new freezing events to occur.

To illustrate the importance of ΔT, we calculated optical depth changes (wave – no wave) for runs with superimposed waves with A = 1 m sec^{-1} and variable ΔT and τ_{wave} (Figure 11). Superimposed waves resulted in vertical displacement ranging from 0.016 to 16 K over τ_{wave} ranging from 0.16 to 166 minutes. Turbulent scale waves (ΔT=0.016 K - not shown) and convective scale waves (ΔT=0.16 K) had limited influence on cirrus optical depths. Mesoscale waves (ΔT=1.6 K) had little influence on $\overline{\sigma}$, but with large $\tau_{fallout}/\tau_{growth}$ increased the std(σ) about the no wave mean (see also Figure 5). Synoptic waves (ΔT=16 K) had significant influence on the mean and standard deviation in optical depth. Large changes in optical depth resulted because large ΔT allowed new homogeneous freezing events to occur (Figure 11).

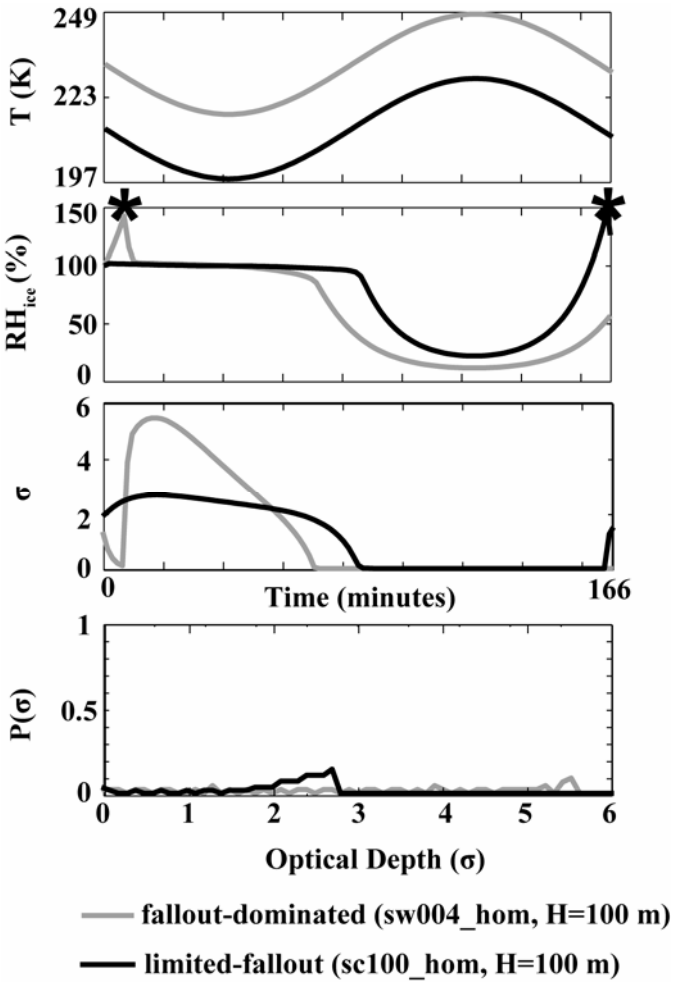

Figure 10: Influence of superimposed synoptic waves with ΔT = 16 K on the evolution of fallout-dominated and limited-fallout initial cirrus clouds: a. T evolution b. RH_{ice} (S_i-100) evolution c. Optical depth evolution d. P(σ) along trajectory. For both model runs, $\overline{w}$=0 and initial S_i=0%. This plot shows that large ΔT resulted in additional freezing events (indicated by *) for both the fallout-dominated and the limited-fallout regime initial clouds.

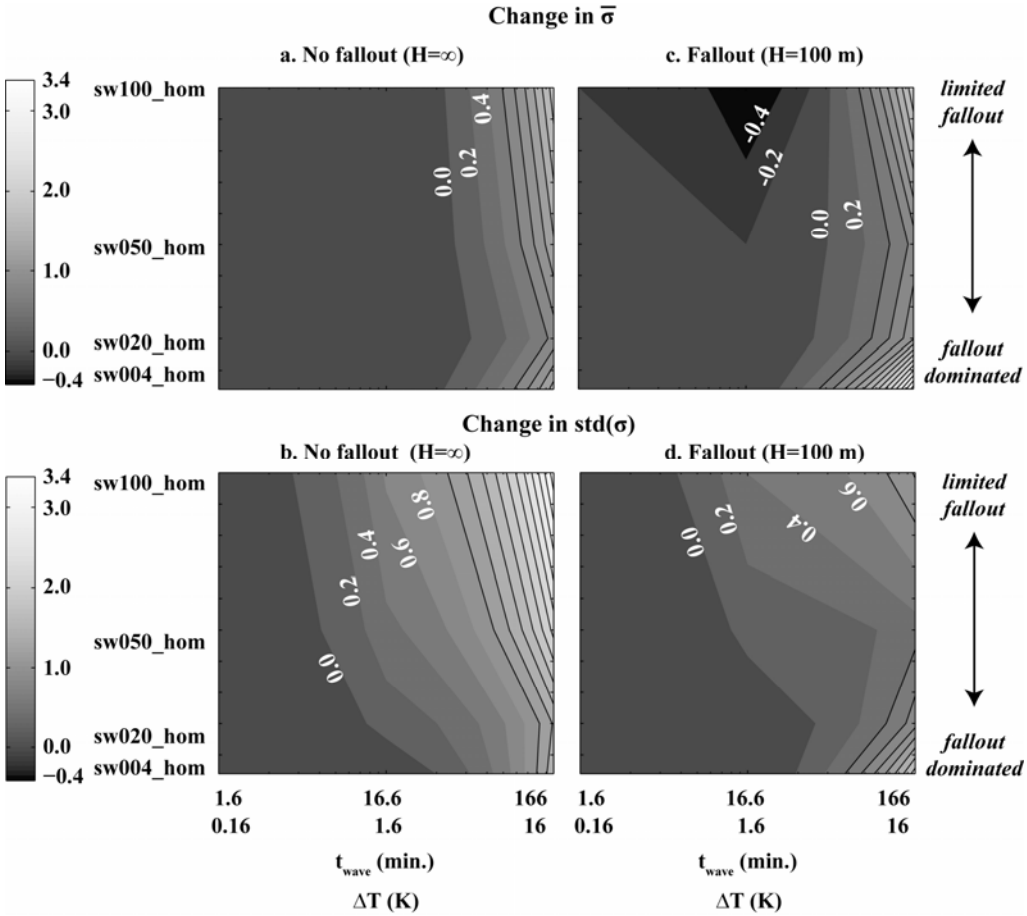

Figure 11: Change (wave – no wave) in cirrus optical depth moments resulting from superimposed waves of varying τ_{wave} and constant A. For all runs, the initial S_i was 0%, and the change in std(σ) was calculated after subtracting a line fitted to the no wave optical depth decay. Convective scale waves have limited influence on optical depths. *a&b. Change in $\overline{\sigma}$ and std(σ) about the no wave mean with H= ∞* Without fallout, mesoscale waves can imprint themselves on the optical depth evolution, but do not influence $\overline{\sigma}$. Synoptic waves affect the sequence of freezing events, and increase both $\overline{\sigma}$ and std(σ). *c&d. Change in $\overline{\sigma}$ and std(σ) about the no wave mean with H=100m* With fallout, mesoscale waves only increase std(σ) for the limited-fallout clouds. Synoptic waves have diminished impact because $\tau_{wave} \geq \tau_{fallout}$. When $\tau_{fallout} << \tau_{wave}$ or $\tau_{fallout} >> \tau_{wave}$, synoptic waves enable new freezing events and increase $\overline{\sigma}$ and std(σ).

3.3.2. Influence of idealized waves on freezing (Experiment 2b)

In addition to their impact on cirrus evolution, superimposed waves also affected the freezing of new ice crystals. To influence homogeneous freezing, waves had to generate high S_i over the duration of typical $\tau_{freezing}$ (for example, $\tau_{freezing}$ calculated in experiment 1- see Table 4). Freezing rates were sensitive to superimposed waves with short τ_{wave} because freezing occurred in 10s of seconds to a few minutes (Table 4). As the duration of large cooling rates increased, so did the N_{ice} generated by homogeneous freezing (Figure 12). As in Hoyle et al. (2005), we found small-scale waves with high cooling rates can generate large N_{ice}. When wave amplitude was fixed at a cooling rate of 36 K hour^{-1}, τ_{wave} must be greater than approximately 10 seconds to influence homogeneous freezing N_{ice} (Figure 12). The N_{ice} generated by heterogeneous freezing was relatively insensitive to the duration and magnitude of the cooling rate, but the presence of IN can increase or decrease homogeneous N_{ice} by changing when homogeneous freezing happens in a wave cycle.

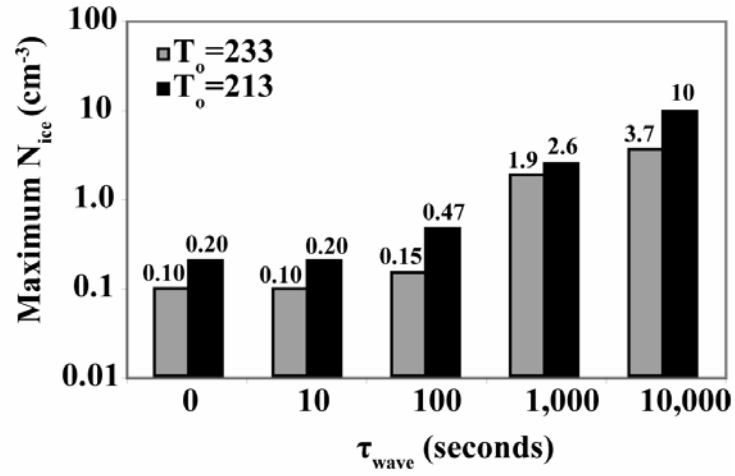

Figure 12: Maximum N_{ice} resulting from superimposed waves with different cooling rate duration (τ_{wave}) but the same maximum cooling rate. For these runs, $\overline{w}$ = 10 cm sec^{-1}, A=1 m sec^{-1} (equivalent to a maximum cooling rate of 36 K hour^{-1}), and the initial S_i=0%. Large cooling rates had to persist for longer than 10 seconds to influence the maximum N_{ice} generated by homogeneous freezing.

4. Conclusions

Using idealized trajectories in an adiabatic parcel model with freezing, growth, and fallout ($H \neq \infty$), we found two regimes for cirrus $P(\sigma)$:

1 - Limited-fallout regime at large $\overline{w}$

In the limited-fallout regime, cirrus formed by homogeneous freezing had large N_{ice}, long $\tau_{fallout}$, large $\tau_{fallout}/\tau_{growth}$, and large $\tau_{fallout}/\tau_{lift\text{-}hom}$ resulting in $P(\sigma)$ peaked at large optical depths ($\sigma > 1$). The limited-fallout regime $P(\sigma)$ with only homogeneous freezing corresponds to a gamma distribution with a large $\overline{\sigma}$ and $\nu > 1$. Large $\tau_{lift\text{-}het}/\tau_{growth}$ indicated glaciated IN could not prevent increases in S_i and homogeneous freezing. However, as a result of large $\tau_{fallout}/\tau_{lift\text{-}het}$, IN stayed with the parcel and did limit the maximum N_{ice} generated by homogeneous freezing. With IN, the peak in the limited-fallout $P(\sigma)$ occurred at a smaller optical depth and $P(\sigma)$ had an additional monotonically decreasing tail at low optical depth values. This shape cannot be reproduced by a single gamma distribution. Cirrus with large N_{ice} were the most likely to be impacted by mesoscale temperature fluctuations because they had the largest $\tau_{wave}/\tau_{growth}$ and the smallest τ_{wave}/τ_{fall}. These superimposed temperature fluctuations broadened $P(\sigma)$ and can be represented in a gamma distribution by decreasing ν.

2 - Fallout-dominated regime at small $\overline{w}$

In the fallout-dominated regime, cirrus formed by homogeneous freezing had small N_{ice}, short $\tau_{fallout}$, small $\tau_{fallout}/\tau_{growth}$, and small $\tau_{fallout}/\tau_{lift\text{-}hom}$, resulting in monotonically decreasing $P(\sigma)$ dominated by small optical depths. This fallout-dominated regime $P(\sigma)$ could be approximated by a gamma distribution with a small $\overline{\sigma}$ and $\nu \leq 1$. Despite large $\tau_{lift\text{-}het}/\tau_{growth}$, glaciated IN quickly fell out in the fallout-dominated regime because of small $\tau_{fallout}/\tau_{lift\text{-}het}$ and new homogeneous freezing events occurred. The fallout-dominated $P(\sigma)$ with IN were similar to fallout-dominated $P(\sigma)$ with homogeneous freezing only. The optical depth evolution in cirrus formed in the fallout-dominated regime was relatively insensitive to superimposed mesoscale waves because the limited-fallout regime resulted in the smallest $\tau_{wave}/\tau_{growth}$ and the largest τ_{wave}/τ_{fall}.

In addition to the two distinct P(σ) regimes, we found:

- Without fallout (H=∞), a limited-fallout regime P(σ) shape resulted for all $\overline{w}$. With large $\overline{w}$, a limited-fallout P(σ) shape occurs for all values of H. However, with small $\overline{w}$, increasing H resulted in longer $\tau_{fallout}$, increased $\overline{\sigma}$ and a transition from fallout-dominated P(σ) shape to fallout-limited P(σ). Fallout was required to obtain a P(σ) with a monotonically decreasing shape.
- With IN concentrations up to 0.1 cm^{-3} and H = 100 m, homogeneous freezing controlled the optical depth evolution. IN had the largest influence on P(σ) when present in large concentrations in the limited-fallout regime.
- For a constant IN concentration and S_{cr}^{het}, changing the IN glaciation function from a step function to a more gradual glaciation with increased S_i did not change P(σ) shape. The IN glaciation function functional form did influence N_{ice} at small $\overline{w}$, but not at large $\overline{w}$.
- Idealized temperature fluctuations influenced P(σ) by superimposing themselves on optical depth evolution or causing new freezing events.
- In order for superimposed temperature fluctuations to broaden P(σ), the amplitude of the temperature fluctuations, ΔT, must be large enough wave to significantly change S_i, and the comparison of microphysical and fluctuation timescales must result in large $\tau_{wave}/\tau_{growth}$ and small $\tau_{wave}/\tau_{fallout}$.
- To influence P(σ) through new homogeneous freezing events, cooling events must generate high S_i over the duration of typical freezing events. In our experiments, this meant large cooling rates had to persist for longer than approximately 10 seconds.

There are limitations to using a parcel model to understand cirrus evolution and P(σ). Namely, the following approximations affect our results:

- Mixing timescales in the upper troposphere can limit validity of the adiabatic assumption. Using a range of aircraft estimates for TKE dissipation rates in the presence of cirrus

(Smith and DelGenio, 2001), we found turbulence can destroy adiabatic parcels with depths of 100 m in 6 to 195 minutes. From this simple calculation, we see the adiabatic assumption breaks down in highly turbulent areas. On the other hand, in cirrus with low TKE dissipation rates, turbulent mixing is slower than most of our calculated microphysical timescales. Therefore, our results are primarily applicable in low turbulence regimes.

- We neglected the influence of radiation on cirrus evolution. Solar and IR cooling rates are generally less than 0.2 K per hour (Fu et al., 1997; Liou, 2002), but these rates are larger with optically thicker clouds. Modeling studies have demonstrated that radiation can affect cirrus cloud lifetimes (Dobbie and Jonas, 2000) and crystal size distributions (Gu and Liou, 2000). Using published cooling rates, radiation timescales to change cirrus cloud temperatures by 2 °C (~600 minutes) are much longer than the timescales used to diagnose $P(\sigma)$ shapes in this study.
- We ignored IN replenishment and ice particle aggregation.
- We used a small set of idealized trajectories, initial conditions, and soundings in this study. In the real atmosphere, non-uniform lapse rates, dry layers, and other anomalies would perturb our results.
- The idealized Lagrangian cirrus evolution in a parcel model cannot be directly compared to cirrus observations which result from the combination of a large number of more complicated trajectories.
- Finally, our parcel modeling provides a simplified 0-dimensional view of complicated 3-dimensional cirrus processes. To model $P(\sigma)$, we assume that cirrus optical depth evolution is largely determined by the generating region. More realistic treatment of cirrus processes requires more complex models. For example, although we have included fallout in our parcel modeling, a more sophisticated model would vertically resolve the interplay between freezing, growth, and fallout processes. Indeed, Lin et al. (2005) demonstrated that homogeneous freezing in cirrostratus is sensitive to the vertical grid resolution. Testing our results with more sophisticated cloud models is a necessary next step to validate and extend our $P(\sigma)$ shape hypotheses.

Despite the described limitations, the fallout-dominated and limited-fallout regimes we have identified are useful for developing hypotheses to explain the main controls on observed cirrus P(σ). Comparisons of parcel-model predicted P(σ) shapes for single trajectories resemble observations from similar meteorological situations at the ARM site in Lamont, OK. The observed isolated cirrus P(σ) (Figure 1) resembles the fallout-dominated P(σ) (Figure 3). The anvil cirrus P(σ) resembles the limited-fallout with heterogeneous freezing (Figure 9b) or a combination of the limited-fallout at large w and the fallout-dominated regime at small w (Figure 1). Finally, the orographic ridge cirrus has a broad P(σ) resembles the limited-fallout cirrus evolution with superimposed waves (Figure 5).

Given the importance of cirrus radiative forcing, it is imperative to understand the physical situations in which P(σ) which can (cannot) be represented by a single gamma distributions in GCMs and the physical factors that determine ranges of $\overline{\sigma}$ and std(σ). We are excited that modeled P(σ) shapes provide testable explanations for the observed P(σ) shapes. We plan future comparison of observed and modeled cirrus P(σ) to test our understanding of the main controls on cirrus evolution. The next step will require statistical comparisons between modeled and observed P(σ). We anticipate our research relating P(σ) to microphysical and dynamical timescales will help the cirrus community better understand observed cirrus P(σ) and parameterize cirrus P(σ) in climate models.

Notation

A	wave amplitude vertical velocity, m sec^{-1}.
a_w	aerosol water activity, dimensionless.
a_w^{ice}	activity of water in a solution in equilibrium with ice, dimensionless.
D	diffusion coefficient, m^2 sec^{-1}.
dt	parcel model time step, sec.
F	fraction of ice particles that falls out of each parcel model bin in dt, dimensionless.
H	parcel depth, m.
IWC	ice water content, mg kg^{-1}.
J	freezing rate, m^{-3} sec^{-1}.
J_{hom}	homogeneous freezing rate, m^{-3} sec^{-1}.
J_{het}	heterogeneous freezing rate, m^{-3} sec^{-1}.

$N_{IN\text{-}max}$	maximum number concentration of glaciated ice nuclei, m^{-3}.
N_{CCN}	maximum number concentration of aerosol, m^{-3}.
N_{ice}	number concentration of ice crystals, m^{-3}.
P_o	initial air pressure, Pa.
$P(\sigma)$	optical depth distribution, dimensionless.
$P_{freezing}$	probability of aerosol freezing, sec^{-1}.
R_{eff}	effective radius of ice crystals, m.
r_o	aerosol or drop radius, m.
R_{ice}	ice crystal radius in each parcel model bin, m.
$S_{cr}^{\hom}$	critical S_i for homogeneous freezing, %.
S_{cr}^{het}	critical S_i for heterogeneous freezing,%.
S_i	supersaturation with respect to ice, %.
S_{io}	initial supersaturation with respect to ice for parcel model experiments, %.
t	time, sec.
T	temperature, K.
T_o	initial temperature for parcel model experiments, K.
V_{fall}	fallout velocity, m sec^{-1}.
w	vertical velocity, m sec^{-1}.
$\overline{w}$	uniform vertical velocity, m sec^{-1}.
Γ_{ice}	pseudoadiabatic with respect to ice lapse rate, K m^{-1}.
$\Gamma(\nu)$	gamma function, dimensionless.
Δ	ratio of the homogeneous and heterogeneous kinetic pre-factors, dimensionless.
Δz	cloud depth, m.
ΔT	maximum temperature excursion caused by wave, K.
ν	gamma distribution fit parameter, dimensionless.
ρ_{sat}	saturation vapor density, kg m^{-3}.
ρ_{ice}	density of ice, kg m^{-3}.
ρ_{vap}	supersaturated vapor content $[S_i*\rho_{sat}(T)]$, kg ,$^{-3}$.
σ	optical depth, dimensionless.
$\overline{\sigma}$	mean optical depth, dimensionless.
$std(\sigma)$	standard deviation in optical depth, dimensionless.
$\tau_{fallout}$	parcel model fallout timescale, sec.
τ_{growth}	parcel model growth timescale, sec.
$\tau_{lift\text{-}het}$	heterogeneous freezing lift S_i generation timescale, sec.
$\tau_{lift\text{-}hom}$	homogeneous freezing lift S_i generation timescale, sec.

$\tau_{freezing}$ parcel model freezing timescale, sec.

τ_{wave} wave period, sec.

Acknowledgments: The authors thank Dr. Stefan Fueglistaler and Dr. Qiang Fu for fruitful discussion and comments on this manuscript; and Dr. Dave Turner for providing and helping interpret the raman lidar optical depth observations. We also acknowledge NSF-ATM-02-1147 for funding this research.

References

Carlin, B., Fu, Q., Lohmann, U. Mace, G., Sassen, K., and J. Comstock (2002), High-cloud horizontal inhomogeneity and solar albedo bias, *J. Climate*, 15 (17), 2321-2339.

DeMott, P. J., Cziczo, D. J., Prenni, A. J., Murphy, D. M., Kreidenweis, S. M., Thomson, D. S., Borys, R. and D. C. Rogers (2003), Measurements of the concentration and composition of nuclei for cirrus formation, *Proc. Natl. Acad. Sci.*, 100:25, 14655-14660.

DeMott, P. J., Rogers, D. C., and S. M. Kreidenweis (1997), The susceptibility of ice formation in upper tropospheric clouds to insoluble aerosol components, *J. Geophys. Res.*, 102 (D16), 19575-19584.

Demoz B. B., Starr D. O., Chan K. R., and S. W. Bowen (1998), Wavelet analysis of dynamical processes in cirrus, *Geophys. Res. Lett.*, 25 (9), 1347-1350.

Dobbie, S. and P. Jonas (2001), Radiative influences on the structure and lifetime of cirrus clouds, *Q. J. R. Meteorol. Soc.*, 127 (578), 2663-2682.

Fu, Q. and K. N. Liou (1993), Parameterization of the radiative properties of cirrus clouds, *J. Atmos. Sci.*, 50 (13), 2008-2025.

Fu, Q., Liou, K. N., Cribb, M. C., Charlock, T. P., and A. Grossman (1997), Multiple scattering parameterization in thermal infrared radiative transfer, *J. Atmos. Sci.*, 54 (24), 2799-2812.

Fu, Q., Carlin, B. and G. Mace (2000), Cirrus horizontal inhomogeneity and OLR bias, *Geophys. Res. Lett.*, 27 (20), 3341-3344.

Gierens K, Schumann U, Helten M, Smit H, and P. H. Wang (2000), Ice-supersaturated regions and subvisible cirrus in the northern midlatitude upper troposphere, *J. Geophys. Res.*, 105 (D18), 22743-22753.

Gu, Y. and K. N. Liou (2000), Interactions of radiation, microphysics, and turbulence in the evolution of cirrus clouds, *J. Atmos. Sci.*, 57 (15), 2463-2479.

Gultepe, I. and D. O. Starr (1995), Dynamical structure and turbulence in cirrus clouds: Aircraft observations during FIRE, *J. Atmos. Sci.*, 52 (23), 4159-4182.

Haag, W. and B. Kärcher (2004), The impact of aerosols and gravity waves on cirrus clouds at mid-latitudes, *J. Geophys*. Res., 109 (D12), doi:10.1029/2004JD004579.

Hoyle, C. Luo, B. P. and T. Peter (2005), The origin of high ice crystal number densities in cirrus clouds, *J. Atmos. Sci.*, 62 (7), 2568-2579.

Jacobson, M. Z. (1999), *Fundamentals of Atmospheric Modeling*, 600 pp., Cambridge Univ. Press, New York.

Jensen, E. J. and O. B. Toon (1994), Ice freezing in the upper troposphere: sensitivity to aerosol number density, temperature and cooling rate, *Geophys. Res. Lett.*, 21 (18), 2019-2022.

Jensen, E.J., Toon, O.B., Vay, S.A., Ovarles, J., May, R., Bui, T.P., Twohy, H. Gandrud, B.W., Pueschel, R.F., and U. Schumann (2001), Prevalence of ice-supersaturated regions in the upper troposphere: Implications for optically thin ice cloud formation, *J. Geophys. Res.*, 106 (D15), 17253-17266.

Kärcher, B. (2003), Simulating gas-aerosol-cirrus interactions: Process-oriented microphysical model and applications, *Atmos. Chem. Phys.*, 3, 1645-1664.

Kärcher B. and U. Lohmann (2003), A parameterization of cirrus cloud formation: heterogeneous freezing, *J. Geophys. Res.,* 108 (D14), 4402, doi:10.1029/2002JD003220.

Kärcher, B. and J. Strom (2003), The roles of dynamical variability and aerosols in cirrus cloud formation, *Atmos. Chem. Phys.*, 3, 823-838.

Khvorostyanov, V. I. and J. A. Curry (2004), The theory of ice freezing by heterogeneous freezing of deliquescent mixed CCN. Part I: Critical radius, energy and freezing rate, *J. Atmos. Sci.*, 61 (22), 2676-2691.

Khvorostyanov, V. I. and J. A. Curry (2005), The theory of ice freezing by heterogeneous freezing of deliquescent mixed CCN. Part II: Parcel model simulation, *J. Atmos. Sci.*, 62 (2), 261-285.

Koop, T., Luo, B. Tslas, A. and T. Peter (2000), Water activity as the determinant for homogeneous ice freezing in aqueous solutions, *Nature*, 406, 611-614.

Lin, R.-F., O'Starr, D. O., Reichardt, J., and P. J. DeMott, (2005). Nucleation in synoptically forced cirrustratus, *Journal of Geophysical Research*, 110, D08208, doi:10.1029/2004D005362.

Lin, R.-F., O'Starr, D. O., DeMott, P. J., Cotton, R., Sassen, K., Jensen, E., Kärcher, B., and X. Liu (2002), Cirrus parcel model comparison project. Phase 1: The critical components to simulate cirrus initiation explicitly, *J. Atmos. Sci.*, 59 (15), 2305-2329.

Liou, K. N. (2002), *An Introduction to Atmospheric Radiation*, International Geophysics Series Vol. 84, 2nd ed., 583 pp., Academic Press, San Diego, California.

Meyers, P. J., DeMott, P. J., and W. R. Cotton (1992), New primary ice-freezing parameterization in an explicit cloud model, *J. App. Meteror.*, 55, 2039-2052.

Minikin A., Petzold, A. , Strom, J. , Krejci, R., Seifert, M., Velthoven, P., Schlager, H. and U. Schumann (2003), Aircraft observations of the upper tropospheric fine particle aerosol in the Northern and Southern Hemispheres at midlatitudes, *Geophys. Res. Lett.*, 30 (10), 1503, doi:10.1029/2002GL016458,

Möhler, O, Stetzer, O. Schaefers, C. , Linke, C., Schnaiter, M., Tiede, R., Saathoff, H., Kramer, M., Mangold, A., Budz, P., Zink, P., Schreiner, J., Mauersberger, K., Haag, W., Kärcher, B. and U. Schurath (2003), Experimental investigation of homogeneous freezing of sulphuric acid particles in the aerosol chamber AIDA, *Atmos. Chem. Phys.*, 3, 211-223.

Murphy, D. M. and T. Koop (2005), Review of the vapor presser of ice and supercooled water for atmospheric applications, *Q. J. R. Meteorol. Soc.*, 131 (608), 1539-1565.

Myhre, C. E. L., Nielson, C. J. and O. W. Saastad (1998), Density and surface tension of aqueous H_2S0_4 at low temperature, *J. Chem. Eng. Data*, 143, 617-622.

Rogers, D. C., DeMott, P. J., Kredenweis, S. M., and Y. Chen (1998), Measurements of ice nucleating aerosols during SUCCESS, *Geophys. Res. Lett.*, 25:9, 1383-1386.

Smith S. A. and A. D. DelGenio (2001), Analysis of aircraft, radiosonde, and radar observations in cirrus clouds observed during FIRE II: The interactions between environmental structure, turbulence, and cloud microphysical properties, *J. Atmos. Sci.*, 58 (5), 451-461.

Spice, A., Johnson, D. W., Brown, P. R. A., Darlison, A. G. and C. P. R. Saunders (1999), Primary ice freezing in orographic cirrus clouds: A numerical simulation of the microphysics, *Q. J. R. Meteorol. Soc.*, 125, 1637-1667.

APPENDIX B: DATA PROCESSING

1.1 Description

For this dissertation, we analyzed Raman lidar and radiosonde observations collected between January 1998 and September 2001. In this appendix, we provide further processing details. An overview of processing and a description of the estimated variables were also described in Table 3.2 and 3.3. The interested reader should contact J. Kay for additional processing details and/or the code used to complete the analyses.

1.2 Cirrus cloud masks and temperature profile analysis

From the lidar depolarization data, we constructed time-height ice cloud masks and computed cirrus cloud statistics. ~4000 hours of lidar observations met our criterion for cloud mask analysis: ice cloud presence, 12-hours of continuous observations, and two concurrent atmospheric soundings. To construct cloud masks, we classified all points with depolarization ratios greater than 10% and low depolarization errors (random error < 20%) as ice and all other points as non-ice. Continuity was an important priority for ice cloud masks inhomogeneity analysis. Therefore, we used 10-minute lidar depolarization observations to maximize data quality (i.e., reduce random error in depolarization). We required 12 hours of continuous observations to minimize data gaps which would result in false positive identification of cirrus inhomogeneity.

From the ice cloud masks, we computed cirrus duration (D, min) at each height and layer thickness (Δz_{layer}, km) and total thickness, (Δz_{total}, km) at each time. Using linearly interpolated radiosonde wind profiles, we converted cloud durations (D, minutes) into effective cloud lengthscales, L_{eff} (km). Using the ice cloud masks and linearly interpolated radiosonde temperature profiles, we calculated in-cloud temperature (T_c, °C) and we related durations and thicknesses to temperature. Using temperature profiles within 3 hours of cirrus, we calculated in-cloud Φ (K/km) and above-cloud Φ (K/km). Temperature profiles were sampled every 250 m for Φ calculations.

1.3 Upper tropospheric RH_{ice}

We calculated relative humidity with respect to ice using raman lidar estimates of water vapor mixing ratio (10-minute temporal resolution) and linearly interpolated radiosonde temperature and pressure observations. We used the Murphy and Koop (2005) es_{ice} formulation in our calculations. Our criterion for relative humidity observation utilization were: random errors in water vapor less than 20% and random errors in depolarization less than 20%. In-cloud RH_{ice} had depolarization ratios greater than 10% (43,164 total observations). In addition to finding in-cloud RHice, we also found clear air RH_{ice} for three upper tropospheric environments. Near-cloud RH_{ice} DR<10% and were within 30 minutes and 500 m of cirrus (77,552 total observations). Below-cloud RH_{ice} DR<10% and were up to 1000 m below cirrus (44,627 total observations). Distant-from-cloud RH_{ice} DR<10% and were far from cirrus (>6 hours) and had heights > 8.3 km (105,172 total observations).

1.4 Cirrus optical depths (σ)

Using 1-minute lidar backscatter at cloud base and cloud top, we calculated cirrus optical depths (σ) using Beer's law. We selected the most continuous optical depth time series and computed optical depth distributions [P(σ)] for 774 3-hour periods. We use 1-minute optical depth observations to capture most of the variability that is important for radiative impacts (Carlin et al., 2000). Our error treatment was very generous because we believe including some noise was better than having discontinuous optical depth time series. We excluded σ observations with error values greater than 10, or percentage errors greater than 1000%. To keep points which we know were affected by lidar extinction, we set these points to the lidar attenuation limit (nominally 3). If $\sigma > 3$ and the attenuation flag was yes, σ was set to the maximum observed optical depth with reasonable errors.

VITA

Jennifer E. Kay was born and raised in Ithaca, New York. She received a B.A. degree in 1999 magna cum laude and with honors from Brown University, where she majored in Economics and Geological Sciences. After a year of Economic consulting in Washington, D.C., she moved to Seattle, Washington in 2000 to begin graduate studies in the Department of Earth and Space Sciences at the University of Washington. She received her Master of Science degree in 2002 under the supervision of Professor Alan Gillespie. In 2006, she earned her Ph.D. under the supervision of Professor Marcia B. Baker and Professor Dean A. Hegg.